TECHNISCHE UNIVERSITÄT WIEN

DISSERTATION

Polyharmonic Distortion Modeling of Non-linear RF Components

ausgeführt zum Zwecke der Erlangung des akademischen Grades
eines Doktors der technischen Wissenschaften

unter der Leitung von
Assoc.Prof. Dipl.-Ing. Dr.techn. Holger Arthaber
Institute of Electrodynamics, Microwave and Circuit Engineering

eingereicht an der Technischen Universität Wien
Fakultät für Elektrotechnik und Informationstechnik

von

Dipl.-Ing. Bernhard Pichler
Matr.Nr. 0725801

Wien, im März 2020

Abstract

Having an accurate model of a non-linear device under test (DUT) is indispensable in radio frequency (RF) circuit design. Such a model allows to perform a design process for a circuit fully in a computer aided design (CAD) environment, without relying on time-consuming empirical design methods like load-pull measurements. Furthermore, a more comprehensive description of the DUT's behavior is possible, allowing to be able to solve the large-signal matching problem, predict voltage and current waveforms at the DUT's terminals, and carrying out the model prediction for different types of stimuli like, e.g., continuous wave (CW) or two-tone excitation.

Due to their generality, black-box behavioral models are desired, because they allow to formulate a model without the knowledge of the DUT's inner workings, solely on port input/output relations. As an important candidate of such models, polyharmonic distortion (PHD) modeling emerged due to its beneficial properties: It uses the well-established traveling waves description in the frequency domain, are a superset of S-parameters for handling non-linear effects, and there exist several well-working extraction techniques. For the extraction measurements, typically a non-linear vector network analyzer (NVNA) is used, which allows to fully measure the non-linear response of a DUT. Based on PHD modeling, X-parameters emerged, which comprise not just the model itself, but also a comprehensive measurement framework.

In this thesis, PHD modeling is discussed, mainly on the example of X-parameters and beyond. It starts from the theory, how they are measured, and their limitations. To demonstrate their accuracy, a commercially available gallium nitride (GaN) high electron mobility transistor (HEMT) is utilized to generate models and to perform verification measurements, in combination with an off-the-shelf NVNA. The requirements on the measurement setup are discussed and it is analyzed how load-dependent X-parameters can help to increase the model accuracy. Therefore, the NVNA is expanded to a high power setup due to power handling requirements. Although highly accurate for harmonic mismatch, the prediction accuracy suffers for strongly non-linear and load-sensitive DUTs.

Like any non-linear model, X-parameters rely on approximation techniques. There, linearization techniques are utilized, similar to a Taylor series approach, while operating the DUT on a large-signal operating point (LSOP). By adding higher order approximation terms, the quadratic polyharmonic distorti-

on (QPHD) model can be formed, which is discussed in this thesis. It is shown how such a model is robustly extracted and the model prediction results are analyzed and compared to X-parameters. Therefore, CW excitation over a wide range of different load conditions is utilized, as well as dynamic stimulus, using a two-tone excitation while assuming quasi-static conditions.

It is discussed in this thesis that X-parameters and the QPHD model can be used to mathematically solve the non-linear matching problem. This enables to identify the load condition for achieving maximum output power as well as maximum drain efficiency, without the need of time-consuming load-pull measurements. The calculated optimum load conditions are carried out using measured X-parameters and QPHD models and are compared to load-pull verification measurements.

Kurzfassung

Modelle für nichtlineare Bauelemente sind unabdingbar für den Schaltungsentwurf in der Hochfrequenztechnik. Solche Modelle erlauben es, den Schaltungsentwurf vollständig in einer CAD Umgebung durchzuführen, ohne zeitaufwändige „load-pull“ Messungen durchführen zu müssen. Außerdem erlauben Modelle eine umfangreichere Beschreibung des Bauelementes, was es ermöglicht das Problem der Anpassung bei Großsignalanregung zu lösen, die Kurvenformen von Strom und Spannung an den Anschlüssen des Bauelementes zu bestimmen, sowie auch eine Vorhersage für unterschiedliche Arten der Anregung zu machen, wie zum Beispiel Dauerstrich oder Zweitonanregung.

Aufgrund ihrer universellen Anwendbarkeit sind Verhaltensmodelle, die das Bauelement als eine sogenannte „black box“ ansehen, wünschenswert. Diese können ausschließlich anhand der Beobachtung ihrer Eingangs- und Ausgangsgrößen formuliert werden, ohne dass Kenntnis des internen Aufbaus vonnöten ist. Als ein wichtiger Vertreter solcher Modelle hat sich „PHD modeling“ herauskristallisiert, aufgrund seiner vorteilhaften Eigenschaften: Die Formulierung dieses Modells erfolgt im Frequenzbereich mit Hilfe der bewährten normierten Leistungswellen, sie sind eine Obermenge zu S-Parametern, welche nichtlinear Effekte berücksichtigen und für die Extraktion der Modellparameter gibt es bewährte Methoden. Dazu wird typischerweise ein nichtlinearer Netzwerkanalysator (NVNA) verwendet, welcher die gesamte nichtlineare Antwort des Messobjektes messen kann. Basierend auf PHD modeling haben sich X-Parameter in der Praxis etabliert, welche zusätzlich zum Modell auch eine umfangreiche Messlösung anbieten, um die Modellparameter zu erhalten.

Diese Dissertation beschäftigt sich mit PHD modeling, was hauptsächlich anhand von X-Parametern behandelt wird. Sie beginnt mit der theoretischen Formulierung des Modells, behandelt die erforderliche Messtechnik und untersucht den Anwendungsbereich dieser Modelle. Um die Genauigkeit zu untersuchen, wird ein kommerziell erhältlicher GaN HEMT, in Kombination mit einem serienmäßigen NVNA, benutzt, um Modelle als auch Verifikationsmessungen durchzuführen. Dabei werden die Anforderungen an das Messsystem dargestellt, und auch die Vorteile von „load-dependent“ X-Parametern werden diskutiert. Aufgrund der Belastbarkeit wird dazu ein Messsystem für hohe Leistungen benutzt. Es wird gezeigt, dass das Modell sehr gut mit Fehlanpassungen bei den Harmonischen umgehen kann, jedoch wird die Modellvorhersage ungenau, falls das Messobjekt eine hohe Empfindlichkeit gegenüber Laständerungen aufweist und in einem stark nichtlinearen Betriebsmodus betrieben wird.

Nichtlineare Modelle beruhen typischerweise darauf, dass das nichtlineare Verhalten des Messobjektes angenähert wird. Bei PHD modeling wird eine Linearisierung um einen Großsignalarbeitspunkt, ähnlich einer Taylorreihe, verwendet. Fügt man quadratische Terme hinzu, erhält man das sogenannte QPHD Modell, welches in dieser Dissertation behandelt wird. Es wird gezeigt, wie man dieses Modell stabil messen kann und die Genauigkeit der Modellvorhersage wird mit der von X-Parametern verglichen. Dazu wird die Last des Messobjektes stark unter Dauerstrichanregung variiert, als auch eine Zweitonanregung unter quasistatischer Näherung verwendet.

In dieser Dissertation wird gezeigt, dass X-Parameter und das QPHD Modell es ermöglichen, das Problem der Anpassung bei Großsignalanregung mathematisch zu lösen. Somit ist es möglich, die optimale Last zu bestimmen, um die maximale Ausgangsleistung, als auch den maximalen Wirkungsgrad zu erhalten, ohne zeitaufwändige load-pull Messungen durchführen zu müssen. Dazu werden gemessene X-Parameter als auch QPHD Modelle verwendet und mit Verifikationsmessungen verglichen.

Contents

Abbreviations

AC	alternating current
ADC	analog to digital converter
AlGaN/GaN	aluminum gallium nitride/gallium nitride
ANN	artificial neural network
BJT	bipolar junction transistor
CAD	computer aided design
CW	continuous wave
DC	direct current
DPD	digital predistortion
DUT	device under test
DWLU	direct waveform look-up
EPHD	enhanced polyharmonic distortion
ET	extraction tone
GaAs	gallium arsenide
GaAs/AlGaAs	gallium arsenide/aluminum gallium arsenide
GaN	gallium nitride
HB	harmonic balance
HBT	heterojunction bipolar transistor
HEMT	high electron mobility transistor

HPR	harmonic phase reference
IF	intermediate frequency
IM3	third order intermodulation product
JFET	junction field effect transistor
LO	local oscillator
LS	large-signal
LSNA	large-signal network analyzer
LSOP	large-signal operating point
LUT	look-up-table
MESFET	metal semiconductor field effect transistor
MTA	microwave transition analyzer
MSE	mean squared error
NVNA	non-linear vector network analyzer
PA	power amplifier
PCB	printed circuit board
PHD	polyharmonic distortion
PM	power meter
PRF	pulse repetition frequency
QPHD	quadratic polyharmonic distortion
RF	radio frequency
Si	silicon
SNR	signal-to-noise ratio
SOLT	short, open, load, through
SPICE	simulation program with integrated circuit emphasis
SRD	step-recovery diode

TRL	through, reflect, line
VIOMAP	Volterra input output mapping
VNA	vector network analyzer
VNNA	vectorial non-linear network analyzer
VSWR	voltage standing wave ratio

Chapter 1

Motivation and Thesis Outline

Linearity is one of the most important properties of a circuit or system in radio frequency (RF) engineering. As stated in [1], 'linearity is so mathematically simple that it enables very general analytical, or closed-form, solutions for system behavior'. This means if a system is linear, it is simple to find a comprehensive description, i.e., model, for this particular system.

Mathematically, the concept of linearity is defined as follows. A function $\mathcal{F}$ is to be considered linear, if two properties are satisfied: Firstly, superposition

$$\mathcal{F}(x+y) = \mathcal{F}(x) + \mathcal{F}(y) \tag{1.1}$$

and secondly, homogeneity

$$\mathcal{F}(\alpha \cdot x) = \alpha \cdot \mathcal{F}(x). \tag{1.2}$$

The quantities x and y are input variables and α is a scalar. Violating at least one of those properties for a given system, means that linearity cannot be assumed. Hence, it is considered to be *non-linear*.

Non-linearity is a very general property. It causes that there are no general solutions for system behavior possible any more, only in a very particular small set of cases [1]. Describing the behavior of a non-linear system is therefore based on approximation techniques. These approximations are typically tailored to fit a certain application and are called *models*. Based on the assumptions made, they have limitations, which are typically described by a certain range of operation. Consequently, there are many different models present, made for a specific use-case and device under test (DUT).

1.1 Non-linear RF Circuits and Systems

In principle, 'all electrical circuits are non-linear' [2]. Consequently, if a circuit is considered linear, it is only assumed to be linear based on an approximation. This is very intuitive for, e.g., transistors, but also passive circuit elements like resistors, capacitors, and others are non-linear at the extremes of their operational range [2]. Non-linear effects occur even at the most basic circuit elements like metallic junctions or connectors, which suffer from passive intermodulation [3].

The most common non-linear circuit elements are active semiconductor devices, like transistors. These are used extensively in RF circuit design. For designing a circuit, a model for the particular non-linear element has to be found by approximating its behavior for the desired application. Therefore, the operational conditions are significant. When utilizing an RF transistor for designing a small-signal amplifier, the behavior of the transistor can easily be approximated by a linear mapping. Consequently, S-parameters are used.

Since demands on RF circuits are increasing steadily, circuit designers are driven into more sophisticated designs in order to improve their performance. This goes along with the evolution of communication systems, trying to increase their capabilities more and more while reducing their costs. There, special focus is put on the power amplifier (PA), because it typically consumes the largest amount of power [4]. To operate an active device like an RF power transistor at high efficiency levels, typically strongly non-linear operation is necessary [5]. Consequently, an S-parameter based design process is not feasible. It is necessary to find an accurate model for the given DUT and perform the design process in a computer aided design (CAD) environment. The accuracy of the model is crucial for the design. Therefore, many different types of models have been proposed to be able to accurately describe non-linearities. Due to its so-called "black-box" approach, a non-linear model based on measurement data analog to S-parameters is desired. This allows that it can be measured for a specific device, allowing to tackle possible manufacturing tolerances and the inner workings are not needed to be known. Consequently, from a manufacturer's point-of-view, the intellectual property of the DUT remains protected and from an design engineer's point-of-view, the inner workings are are often not from interest.

In recent years, X-parameters emerged as a superset of S-parameters for non-linear DUTs [6]. These fit the bill perfectly in many cases, but they have limitations for strongly non-linear DUTs, like RF power transistors. In this thesis, the principles of X-parameters are discussed in detail, showing their benefits and limitations. Furthermore, their concept is expanded to go *beyond* X-parameters, allowing to accurately model RF power transistors applicable for PAs.

1.2 Thesis Outline

This thesis is structured as follows: In Chapter 2 the most popular non-linear models are discussed, with a strong focus on their applicability for RF circuit design. The basic model concepts of physics-based, equivalent circuit, and behavioral models are introduced. Due to its generality, the focus is put on behavioral modeling and in particular frequency domain behavioral models, due to their easier measurement and applicability in RF circuit design.

In Chapter 3, X-parameters are introduced in detail. Beginning with their definition, their relation to S-parameters, extraction procedures, and limitations are discussed. Especially load-dependent X-parameters are discussed and their drawbacks for the use for strongly non-linear DUTs in highly mismatched environments are shown.

The measurement setup for extracting X-parameters is discussed in Chapter 4. It starts by introducing the basic concept of the so-called vectorial non-linear network analyzer (VNNA), which comes in two different instruments: The large-signal network analyzer (LSNA) and the non-linear vector network analyzer (NVNA). Also the calibration is discussed briefly. The DUT, which is used for the measurements in this thesis, is a 10 W RF power transistor. Due to the involved high power levels, the required measurement setup is discussed in detail, leading to adaptations because of power handling issues. It is analyzed how these changes in the setup affect the measurements and how to extract accurate models using such a measurement setup. At the end of this chapter, X-parameter measurements are presented and their accuracy is analyzed using verification measurements.

Chapter 5 discusses extensions to basic X-parameters, leading to a better model prediction accuracy for strongly non-linear DUTs. Therefore, the quadratic polyharmonic distortion (QPHD) model is introduced. It is discussed how this model is extracted and its accuracy is compared to X-parameters. This is done by utilizing both continuous wave (CW) and two-tone excitation.

In Chapter 6, the non-linear matching problem is solved by using X-parameters and the QPHD model. It is derived how to determine the optimum load condition for achieving maximum output power as well as maximum efficiency. The gained results are analyzed by comparing them to verification measurements.

Chapter 2

Non-linear Models

Over the time, the design process of non-linear RF circuits has undergone an evolution from empirical designs to advanced CAD methods. For example, designing an RF PA is a typical non-liner design task. It requires an accurate description of the behavior of the used RF power transistor, which serves as a DUT. Since S-parameters cannot be used due to their restriction to linear circuits, engineers came up with lots of different approaches for describing non-linear RF behavior.

Traditionally, load-pull measurements were used for a non-linear design [7]. These rely on empirical solutions for the matching problem, by varying the load and source impedances while measuring performance parameters like output power or efficiency. Although accurate and widely used in practice, a vectorial description of the port input and output quantities is desired. Consequently, special attention was paid on getting more advanced models for non-linear behavior.

Finding an appropriate model is a difficult task, because describing a non-linear mapping exactly is in most cases not possible. Consequently, many different types of models exist, especially tailored to fit certain requirements and applications. In the following sections the most common types of models are discussed, with a strong focus on usability in RF circuit design. This includes the model prediction for the fundamental frequency (f_0) as well as at the harmonics. Emphasis is put on measurement based frequency-domain black-box behavioral models, because they have several benefits for the use in RF circuit design: They are easier to extract due to the predominately frequency-domain measurement equipment in RF engineering and since the DUT's inner working is not needed to be known for the model formulation, they offer a general modeling approach. Furthermore, easy implementation in an RF circuit simulator is possible, due to their close relation to harmonic balance (HB) simulators, which are predominately used in RF circuit design [8]. This is in stark contrast to a low frequency design, where simulation program with integrated circuit emphasis (SPICE) is most common [9].

In Figure 2.1 an overview of popular non-linear models is shown, which serves as a basis for this chapter. Note that the green highlighted models are discussed in this thesis, while the other ones indicate popular models which are only mentioned for the sake of completeness and are not discussed here. The chapter begins with a brief discussion of physics-based models and equivalent circuit models. Due to the fact that they are derived from the specific internal device composition, they have to be tailored to each specific device and therefore, do not allow generality.

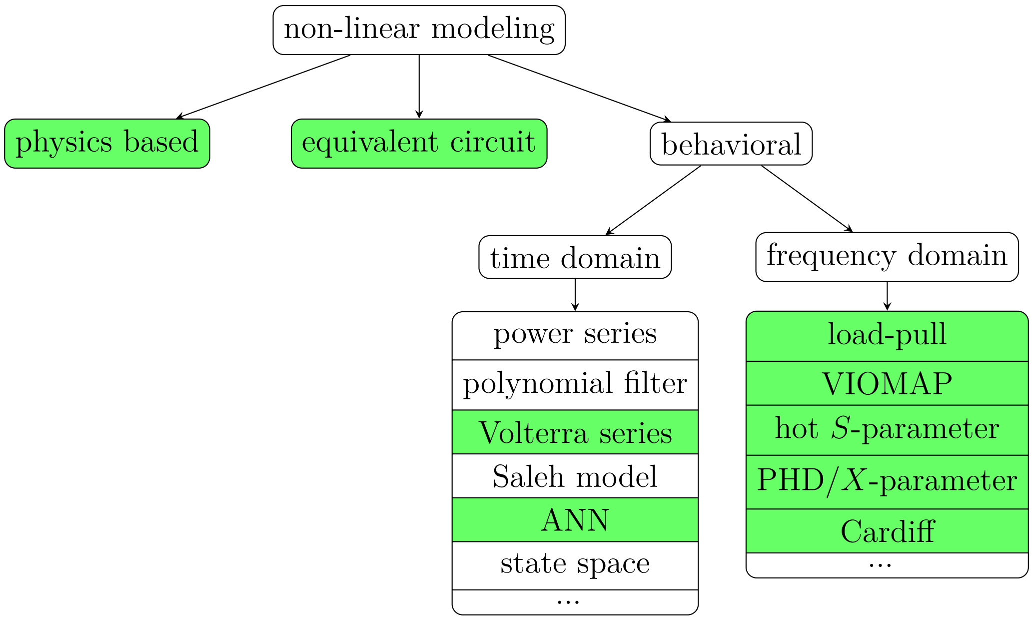

Figure 2.1: Model tree of popular RF models, the green highlighted models are discussed in this chapter.

In contrast to physics-based and equivalent circuit models, a more general approach is desired. It is possible to formulate models which are only dependent on the input/output relations of the DUT. Such models are called behavioral models. These treat the DUT as a black box, hence, knowledge of the inner workings of the DUT is not required. One of the most prominent black-box behavioral models are S-parameters. These are widely used in RF engineering, however, their application is limited to the linear regime.

There are many different behavioral models present, which can be categorized based on their properties. One is to split them into band-pass and equivalent baseband models [10]. Although these terms mainly describe the nature of the input signal, they influence the implementation of the model [11]. Band-pass models make use of the full RF input signal, while equivalent baseband models only consider the signal's envelope for carrying out the model prediction. From an application's point-of-view, the aim of these models is completely different. Equivalent baseband models can easily deal with modulated signals, but they are not able predict the harmonic response, which can on the other hand be done using band-pass models [11]. In contrast, band-pass models are the better choice for the use in circuit design.

Some types of models can be used as band-pass as well as equivalent baseband models, e.g. Volterra series [10]. Hence, for the model categorization in this work, behavioral models are split into time-domain and frequency-domain models. As discussed later in more detail, frequency-domain models offer generally higher flexibility for an application in circuit design, thus they are the focus of this thesis. However, for the sake of completeness, the most important time domain behavioral models are discussed in this chapter, i.e., the Volterra series and artificial neural networks (ANNs).

2.1 Physics-based Models

Physics-based models rely, as the name suggest, on the the internal structure of a certain DUT. This includes the device geometry, used materials, doping profiles, and so on. Consequently, such models are especially tailored to fit a specific DUT, whose internal composition has to be perfectly known. Using this information allows to formulate models to describe the operation of the DUT. For semiconductors this would, for example, include the electron and hole transport and the current continuity relationships [12]. This allows to predict the voltage and current response of the DUT, by solving the semiconductor state equations according to the boundary conditions, given by the device terminals [13].

Solving these semiconductor state equations is very complex and requires a large amount of computational time. Furthermore, such models can only be formulated by the DUT's manufacturer, since the required knowledge of the inner workings of the DUT is in most cases not accessible to an application engineer. Consequently, they are very rarely used in RF circuit design.

2.2 Equivalent Circuit Models

A widely used class of models in RF circuit engineering are equivalent circuit models. Similar to physics-based models, they are specially tailored to fit a certain device, component, and application. However, equivalent circuit models try to abstract the function of the DUT by using well-known circuit elements, like resistors, capacitors, voltage sources, and so on. In contrast to physics-based models, a more computationally efficient model can be found, because the use of circuit elements allows to calculate the node voltages and currents according to Kirchhoff's circuit law, which can easily be implemented in SPICE. Furthermore, an electrical engineer can understand the function of even very complex DUTs easily, because of the use of simple well-known circuit elements.

When applied to RF transistors, a specialized model for each different technology is required, which has to be adapted to each transistor type using this technology. A general model is not possible in many cases, or very complex due to the involved non-linearity. Hence, their applicability is often limited to a certain frequency or input power range.

Equivalent circuit models for transistors have been published shortly after the transistor's invention. For example, the Ebers model [14] and the Gummel-Poon model [15] for the bipolar junction transistor (BJT) are well-known and widely used. Models for the silicon (Si) junction field effect transistor (JFET) and BJT have been implemented in SPICE [16]. An example of a typical equivalent circuit model for a JFET is depicted in Figure 2.2. The main element of such a model

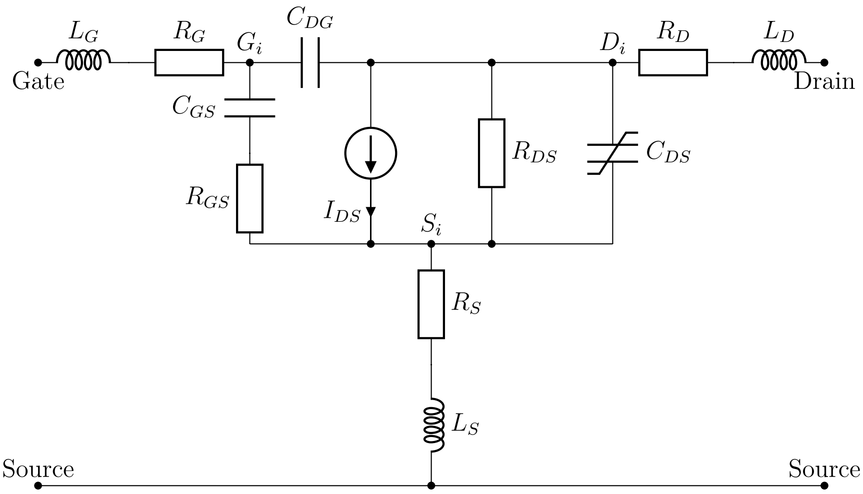

Figure 2.2: Typical equivalent circuit of a FET [17].

is the controlled current source for the drain or collector current, respectively. An accurate model for this current is crucial for the overall model performance. Furthermore, the capacitances between the DUT's terminals are modeled. Additionally, line inductance and resistance is added to model the bonding wires used for connecting the intrinsic gate (G_i), drain (D_i), and source (S_i) to the corresponding package leads. The characteristics of the drain-source current I_{DS} of the voltage controlled current source (Figure 2.2) is dependent on the gate-source voltage V_{GS} and the drain-source voltage V_{DS}. Especially when it comes to large-signal application, this behavior is strongly non-linear. Also the physical dimensions and the properties of the semiconductor material strongly influences I_{DS}. Consequently, finding an accurate description of the drain-source current is crucial for the model accuracy.

In RF the most important requirement on a transistor is having a high transit frequency, which is different to most other electrical engineering applications. Inevitably, suited technologies are used, which are optimized for their frequency handling capabilities. Also the models have to be adapted in a way to describe the high-frequency behavior of this transistors accurately. Due to its excellent high frequency behavior, gallium arsenide (GaAs) metal semiconductor field effect transistors (MESFETs) are widely used in RF applications. Especially the use of GaAs allows to achieve high transit frequencies, due to its high electron mobility compared to Si. As a consequence, the Si JFET models are unable to accurately predict the behavior of such transistors. One of the first models applicable for GaAs MESFETs was introduced by Curtis [18]. This models took emphasis on the stronger current saturation caused by the higher electron mobility in GaAs as well a non-linear description for the gate-source and drain-source capacitance. To get a better model for this saturation effects, a hyperbolic tangent function function is utilized for modeling the drain-source current. With its dependence on the intrinsic gate-source (V_{GS_i}) and drain-source (V_{GS_i}) voltages, the drain-source current is modeled as

$$I_{DS}(V_{GS_i}, V_{DS_i}) = \beta(V_{GS_i} + V_T)^2 \cdot (1 + \lambda V_{DS_i}) \cdot \tanh(\alpha V_{DS_i}), \qquad (2.1)$$

whereas V_T is the gate-source threshold voltage and α, β, and γ are constants. This model offers a simple and accurate description for the GaAs MESFET using a very low number of coefficients. However, further investigations on the model have shown, that the model offers limited accuracy on the transconductance, i.e., the dependence of the drain-source current on the gate-source voltage [19]. One approach to overcome this issue was proposed by Angelov [20], which is in literature called Angelov or Chalmers model. In this model the influence of the transconductance was implemented by introducing a power series function. The parameters of this function can be adapted empirically for a given DUT, allowing for a simple model, showing accurate modeling capabilities for a wide range of different gate-source and drain-source voltages.

With the emergence of the high electron mobility transistor (HEMT), emphasis was taken to adapt the GaAs MESFET equivalent circuit models to the characteristic behavior of the HEMT. Due the use of a semiconductor heterojunction, the electrons in the channel are confined in a 2D structure [21]. This allows to achieve higher electron mobility, and consequently, higher transit frequencies. These devices were initially made using the gallium arsenide/aluminum gallium arsenide (GaAs/AlGaAs) material system, however, especially in high power applications aluminum gallium nitride/gallium nitride (AlGaN/GaN) shows beneficial properties [22]. These are given by, for example, the higher saturation velocity and larger bandgap, which allow higher direct current (DC) supply voltages and higher thermal conductivity. Consequently, the gallium nitride (GaN) HEMT is currently used extensively in RF PA design. To allow for efficient designs, efforts have been made to adapt the GaAs MESFET models to the GaN HEMT [23]. As an example, among many others, the Chalmers model was adapted to fit the requirements of the GaN HEMT [24].

In literature, many different equivalent circuit models have been proposed. Although models like the Chalmers model are utilizing empirical methods for their modeling approach, the major drawback of equivalent circuit models is that they require knowledge of the inner working of the DUT. As a consequence, for many devices no or only proprietary models are available [25, 26]. Despite in many cases highly accurate, their application range and limitations are often not clearly stated, which makes it difficult for an application engineer to identify if a particular model is applicable or not for the specific design task.

2.3 Time-domain Behavioral Models

In many cases, it is from interest to be able to form a model without knowing the DUT in detail. Therefore, so-called black-box models emerged, which rely on input/output observation data. Those models can be gained from any device, regardless of the DUT's structure. This is beneficial also from a manufacturer's point-of-view as the intellectual property remains protected. However, those models rely on measured data, i.e., typically lots of measurements are necessary to generate such models.

The obvious approach for gaining black-box models is formulating table-based or look-up-table (LUT) based models [27]. These consist basically on measured data of the DUT over a wide range of operation. As the name suggests, the measurement data is stored in a table with the operational conditions as parameters. To achieve high accuracy over a wide range of bias points or input power levels, a large number of measurements is needed. Hence, LUT based models tend to have a large model size and interpolation techniques are required for the use in a simulator. Consequently, it is desired to have a more compact model formulation, which allows for an easier implementation in a simulation environment. Therefore, a mathematical representation to describe the DUT's behavior based on measured data is desirable.

Finding a model for a non-linear DUT can be performed similar to a system identification approach, i.e., a mapping between an excitation signal $x(t)$ to the output $y(t)$ has to be identified. If the mapping is static, instantaneous, and memoryless, the response can be written as

$$y(t) = \mathcal{F}[x(t)] \tag{2.2}$$

For a dynamic or memory afflicted system, the output depends on the system state's past. The input-output mapping is represented by a non-linear differential equation [28], as written in recursive form as

$$y(t) = \mathcal{F}\left[x(t), \frac{dx(t)}{dt}, \cdots, \frac{d^{M_1}x(t)}{dt^{M_1}}, \frac{dy(t)}{dt}, \cdots, \frac{d^{M_2}y(t)}{dt^{M_2}}\right]. \tag{2.3}$$

This equation has to be approximated in order to be able to serve as a behavioral model. For non-linear RF DUTs many approaches have been proposed [28, 29], examples for time-domain behavioral models are shown in Figure 2.1. Two of the most important ones, the Volterra series and ANNs, are discussed as follows.

2.3.1 Volterra Series

The output $y(t)$ of a system $\mathcal{H}$ can be described by its input $x(t)$ as

$$y(t) = \mathcal{H}[x(t)]. \tag{2.4}$$

If this system is static, instantaneous, and memoryless as in Equation (2.2), it can be approximated by a Taylor series. This allows to describe such a system using polynomials. If this system is memory afflicted, as in Equation (2.3), a Taylor series is not suitable. However, the Volterra series can be seen as a memory polynomial representation of such a dynamic system [30]. By using this memory polynomial approach for a causal system, the relation between the output $y(t)$ and the input $x(t)$ can be expressed by

$$\begin{aligned} y(t) =& h_0 + \int_0^\infty h_1(\tau_1)x(t-\tau_1)d\tau_1 + \int_0^\infty\int_0^\infty h_2(\tau_1,\tau_2)x(t-\tau_1)x(t-\tau_2)d\tau_1 d\tau_2 \\ &+ \int_0^\infty \cdots \int_0^\infty h_n(\tau_1,\tau_2,\cdots,\tau_n)x(t-\tau_1)x(t-\tau_2)\cdots x(t-\tau_n)d\tau_1\cdots d\tau_n \\ =& h_0 + \sum_{n=1}^{N}\int_0^\infty \cdots \int_0^\infty h_n(\tau_1,\cdots,\tau_n)\prod_{m=1}^{n} x(t-\tau_m)d\tau_n. \end{aligned} \tag{2.5}$$

This is called the "Volterra-series" of N^{th} degree, while $h_n(\tau_1, \cdots, \tau_n)$ denote the Volterra kernels [30]. Note that the Volterra series is a generalization of the Taylor series, able to approximate memory afflicted systems. If no memory is present, the Volterra kernels $h_n(\tau_1, \cdots, \tau_n)$ reduce to $a_n\delta(\tau_1 \cdots \tau_n)$, where δ is

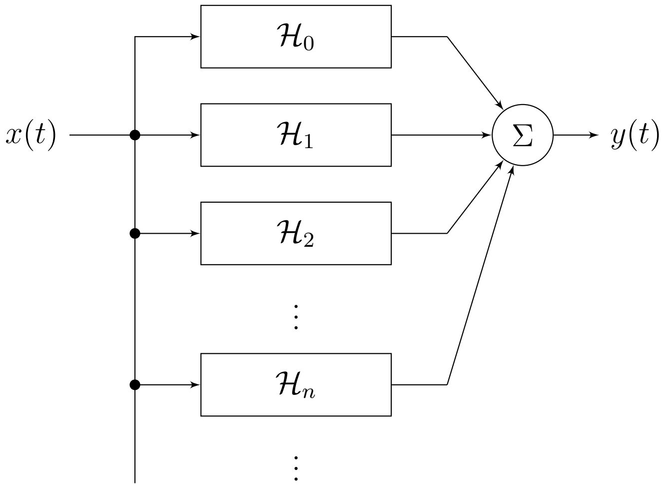

Figure 2.3: Graphical illustration of the Volterra series representation [30].

the Dirac delta function and a is a coefficient. Rewritten to a more general form Equation (2.5) is given as

$$y(t) = \mathcal{H}_0 + \mathcal{H}_1[x(t)] + \mathcal{H}_2[x(t)] + \cdots + \mathcal{H}_n[x(t)] + \cdots , \tag{2.6}$$

with $\mathcal{H}_n$ is called the n-th order Volterra operator, which is given as

$$\mathcal{H}_n[x(t)] = \int_0^\infty \cdots \int_0^\infty h_n(\tau_1, \tau_2, \cdots, \tau_n) \prod_{m=1}^{n} x(t - \tau_m) d\tau_n. \tag{2.7}$$

In Figure 2.3 a graphical representation of the Volterra series is depicted.

The Volterra series is widely used to model non-linear PAs with memory, especially for digital predistortion (DPD) applications [31]. However, it has several limitations: For strongly non-linear behavior the series is often non-convergent. If the series is convergent for strongly non-linear behavior, a high order N is necessary to describe the non-linear effects accurately. This causes a large model size and high computational complexity when used in a simulator [28]. Also an a priori estimation of how large the order N has to be for a certain accuracy is not possible [3]. The extraction of the Volterra series is especially difficult for hard non-linear behavior. Extracting the kernels can be interpreted as estimating coefficients of a noise polynomial with, e.g., least-squares estimation over multiple measurements [32]. Especially for estimating higher order kernels noise can cause problems, leading to an ill-conditioned estimator.

It has several benefits to apply the Fourier transform to Equation (2.5) to get a frequency-domain representation of the Volterra series. This is discussed in more detail in Section 2.4.3.

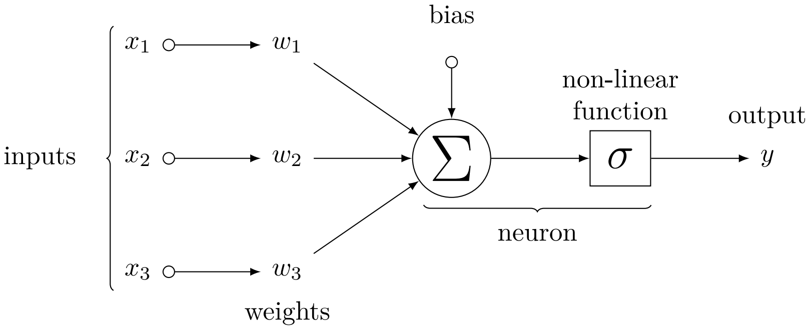

Figure 2.4: Diagram of a simple neuron structure [34].

2.3.2 Artificial Neural Networks

A dynamic non-linear system, as described by Equation (2.3), can be approximated as a black-box by using time-domain ANNs [33]. These models are inspired by the human brain in order to find a generalization of a certain device or system based on observations. An ANN basically consists of a large number of so-called neurons, which are highly interconnected.

An example of a neuron is shown in Figure 2.4. It has a simple structure which consists of an arbitrary number of inputs, e.g., three in this case and an output. Each input signal x is weighted by a weight w. The weighted input signals are summed up including an additional bias and applied to a non-linear function σ, the so-called neuron activation function. There is no clear requirement

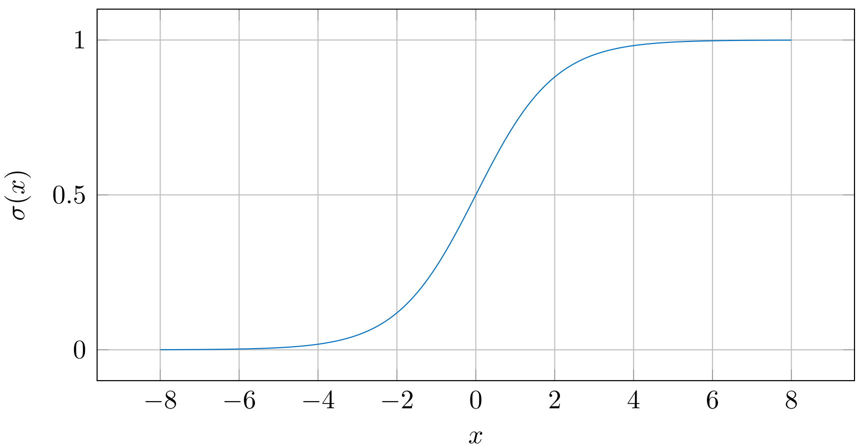

Figure 2.5: Sigmoid function $\sigma(x)$.

on this function, it is strongly dependent on the application of the ANN. Since a non-linear model for an RF device or system is intended to be found, this

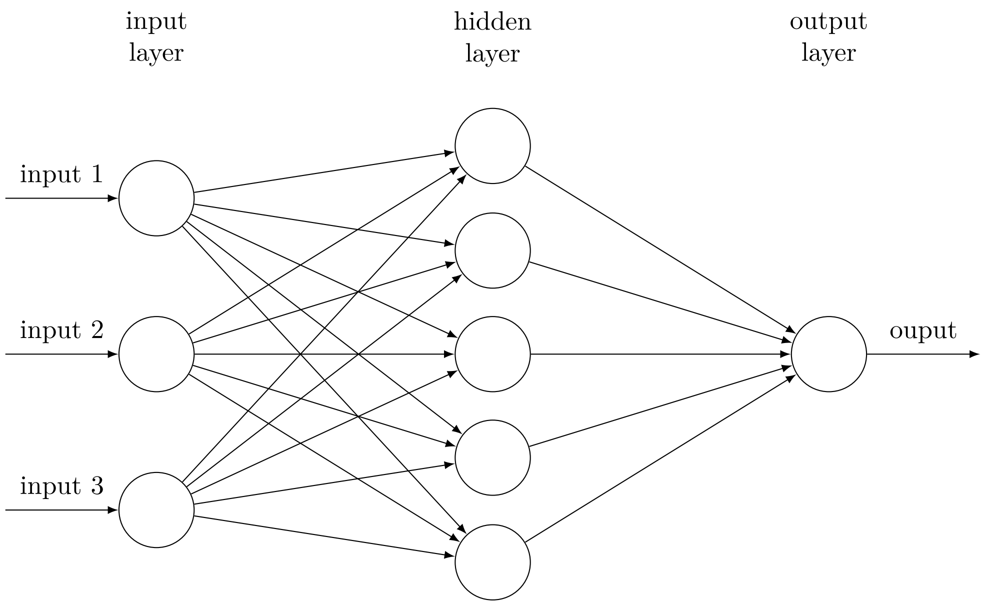

Figure 2.6: Example of a simple ANN.

function has to be non-linear [35]. For example, it is possible to utilize a unit step function, however this leads to a binary output and does not model human decision making. Consequently, it cannot be used for the intended application. In practice, the sigmoid function is often used for approximating non-linear behavior with an ANN [33]. It is given as

$$\sigma(x) = \frac{1}{1 + e^{-x}} \tag{2.8}$$

and a plot is shown in Figure 2.5. This function is monotonically increasing, smooth, and bounded. This ensures that also the output is bounded for any input signal, which means that there is no stability issue for a single neuron.

An ANN generally consists of a large number of neurons, combined in a layered structure, an example is shown in Figure 2.6. There is an input layer, where the inputs are connected to the input neurons. The outputs of the input neurons are connected to the neurons in the hidden layer. In this example, only one hidden layer is presented, but generally an arbitrary number of hidden layers are possible. At last, an output layer is at the output of the ANN, connecting the hidden layer neurons to the output.

ANNs can efficiently be used for modeling non-linear RF devices or systems. Therefore, a so-called ”training” procedure has to be performed. This means, that all weights and bias variables at each involved neuron has to be identified. Typically, measurements gained from the desired DUT are used, like data measured for a table base model [36]. An untrained ANN in contrast does not offer any meaningful output. It is possible, in theory, to approximate any non-linear function to an arbitrary degree of accuracy, as long as there are enough neurons [34]. However, identifying the required number of neurons a priori, for achieving a certain model prediction accuracy, is impossible. Consequently, the structure and the used number of neurons can only be determined by using trial and error. Furthermore, the accuracy is strongly dependent on the training process. This means, that the model extraction measurements have to be chosen wisely.

Time-domain behavioral models offer the possibility to serve as an accurate model for non-linear DUTs. However, they have limitations for hard non-linear behavior, which is often the case in RF circuit design. For such hard non-linear operational conditions time-domain approximation techniques often lead to large model size and they are typically harder to extract. Also an a priori identification of the required model size is often impossible, as discussed for the Volterra series and ANNs. Frequency-domain behavioral models are often better suited for the use in RF circuit design, the most prominent candidates are discussed in the following section.

2.4 Frequency-domain Behavioral Models

In RF engineering the frequency-domain description of a circuit is most common. For example, for a narrow-band circuit predominantly the frequency response is analyzed and not the impulse response. Also, RF measurement equipment, such as the vector network analyzer (VNA) and the spectrum analyzer are frequency-domain instruments. Consequently, frequency-domain measurements are easier to perform in the model extraction measurements. When designing RF circuits, HB simulation is predominately used [34], hence, it is desired to have non-linear frequency-domain black-box behavioral models.

The most important black-box behavioral model in the frequency domain are S-parameters. They are well-known and extensively used in RF engineering [37]. They are utilizing traveling power waves (incident wave a_p and outgoing wave b_p at port p) in order to describe the behavior of a certain DUT in the frequency-domain. Contrary to Z- and Y-parameters, they can easily be measured and do not require open- and short-circuits in the measurements, which makes them an excellent fit for RF circuits.

By using the, in general, complex valued port impedance Z_p, these traveling power waves are defined as

$$a_p = \frac{1}{2}\frac{V_p + Z_p \cdot I_p}{\sqrt{|\Re\{Z_p\}|}} \tag{2.9a}$$

$$b_p = \frac{1}{2}\frac{V_p - Z_p^* \cdot I_p}{\sqrt{|\Re\{Z_p\}|}}, \tag{2.9b}$$

when utilizing the port voltage V_p and port current I_p at the reference plane at port p [38, 39]. A block diagram of a 2-port network showing all involved traveling waves, voltages, and currents at its reference planes is shown in Figure 2.7. Using

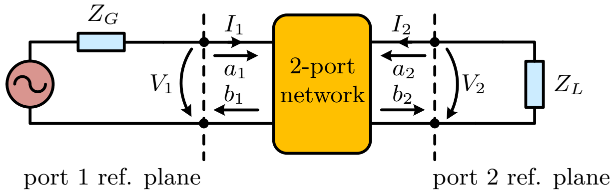

Figure 2.7: Traveling waves for a 2-port network.

linear relations between the waves a and b, the scattering parameter matrix can be defined as

$$\mathbf{b} = \mathbf{S} \cdot \mathbf{a}, \tag{2.10}$$

where the S-parameter matrix for an arbitrary n-port is denoted as

$$S_{n\times n} = \begin{pmatrix} S_{11} & \cdots & S_{1n} \\ \vdots & \ddots & \vdots \\ S_{n1} & \cdots & S_{nn} \end{pmatrix}. \tag{2.11}$$

The benefit of the S-parameter description is that all parameters have a clear physical meaning. The parameter S_{pp} is equal to the input reflection coefficient at port p, where the parameter S_{pq} is equal to the transmission coefficient from port q to port p. However, S-parameters have one important limitation, that they can only be defined in the linear domain. Hence, for modeling DUTs in the non-linear domain, S-parameters cannot be used. To overcome this issue, emphasis was taken on finding frequency-domain black-box behavioral models for non-linear DUTs. Equivalently to time-domain LUT models, the trivial LUT approach can also be used in the frequency domain. However, the same problems occur, i.e., large model size for high accuracy, which lead to high computational complexity, as well as interpolation techniques are required. Consequently, a compact behavioral modeling approach is desired, the most important ones are discussed as follows.

2.4.1 Load-pull Measurements

Traditionally, non-linear RF circuits are designed by using load-pull measurements [7]. Since vectorial measurements of non-linear circuits generally require an extensive measurement setup, load-pull relies on simple scalar measurement quantities such as the RF output power or DC voltages and currents. This can be used to determine performance parameters like output power, gain, and efficiency. Also other scalar quantities can be analyzed, such as plain power consumption [40]. During load-pull measurements, the source and load impedances presented to the non-linear DUT are varied in order to find an optimum for certain performance parameters. This can be interpreted as an empirical solution for the large-signal matching problem.

A typical block diagram of a load-pull measurement setup is depicted in Figure 2.8. This setup shows all necessary components for performing load-pull

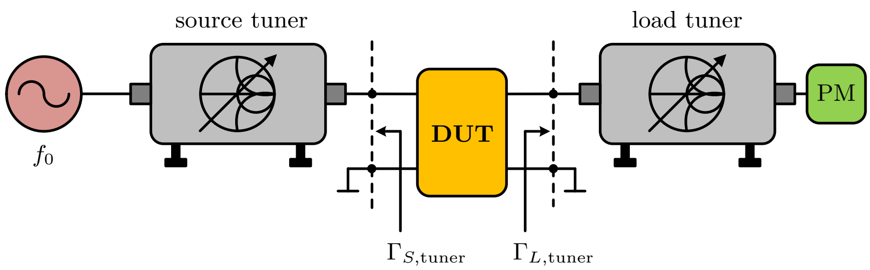

Figure 2.8: Block diagram of a typical load-pull measurement.

measurements. Note that biasing circuits and additional measurement instruments are not depicted here for simplicity. In order to provide the necessary driving power for the DUT, an RF source is needed, which, for a CW operation, provides an output at the fundamental excitation frequency f_0. Impedance tuners are placed at the input and the output of the DUT. Tuning the input is typically denoted as source-pull and tuning the output as load-pull. For a passive setup, these tuners are typically mechanical slide-screw tuners. These allow to provide a certain input $\Gamma_{S,tuner}$ and output reflection coefficient $\Gamma_{L,tuner}$ at the DUT's reference plane. Note that these are only valid at the fundamental frequency f_0, at all other frequency points the provided load and source reflection coefficients are according to the tuner's trajectory. At last, a load termination is needed. There, normally the output power is measured by a power meter (PM).

Load-pull measurements are widely used in PA design, since they allow to determine optimum loads for the non-linear matching problem of a dedicated DUT. This is possible for the fundamental frequency as well as the involved harmonics, when using a so-called harmonic tuning load-pull setup. This allows to use load-pull measurements as a design foundation for advanced PA topologies, such as class E or class F amplifiers, which require defined harmonic terminations [5, 41].

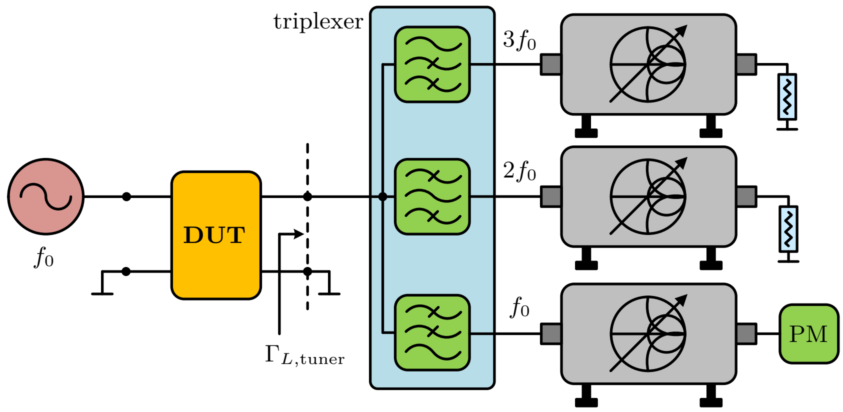

Figure 2.9: Block diagram of a typical triplexer based harmonic tuning load-pull setup.

There are several possibilities for a passive harmonic tuning load-pull setup. The most important ones are the multiplexer filter based harmonic tuning load-pull setup (Figure 2.9) and the cascaded tuning load-pull setup (Figure 2.11) [42]. Both setups are designed to use mechanical slide screw tuners for the fundamental frequency, as well as for harmonic tuning. For the multiplexer based setup, a multiplexer filter is used to separate the fundamental and harmonic frequency bands of the excitation signal. In most cases, this is done up to the third order harmonic, hence, a triplexer is used. Such a filter enables an independent use of three different tuners, see Figure 2.9. The drawback is, that the tuning range is limited due to the inherent insertion loss of the filter. Consequently, the maximum achievable reflection coefficient $\Gamma_{L,tuner}$ is limited. This is especially an issue for the harmonics, as the insertion loss is typically higher for increasing frequencies, see Figure 2.10. This may cause that such a setup is not applicable for PA design, due to the fact that harmonic controlled PAs do need highly reflective terminations at the harmonics [5].

The cascaded harmonic tuning setup, see Figure 2.11, does not need an additional filter for providing a defined load condition for the fundamental frequency and the desired harmonics. To be able to realize a defined reflection coefficient at multiple frequencies, multiple tuners are connected in a cascade. The resulting load reflection coefficient $\Gamma_{L,tuner}$ is therefore formed as a combination on the mutual state of all tuners. Consequently, for a harmonic tuning setup up to the third order harmonic, three tuners are needed. An example of the load reflection coefficient realization is shown in Figure 2.12. In this figure, the load for the

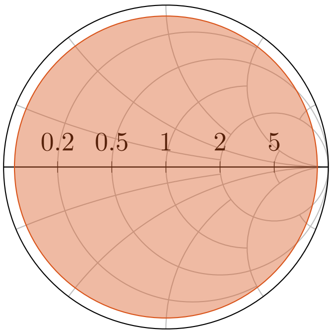

(a) Tuning range at f_0.

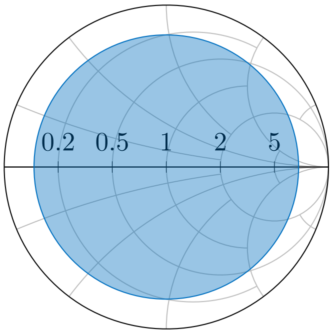

(b) Tuning range at $2 \cdot f_0$.

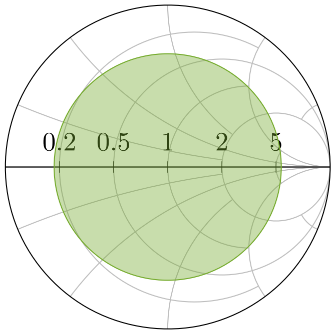

(c) Tuning range at $3 \cdot f_0$.

Figure 2.10: Influence of losses onto the tuning range, which is portrayed as the colored area.

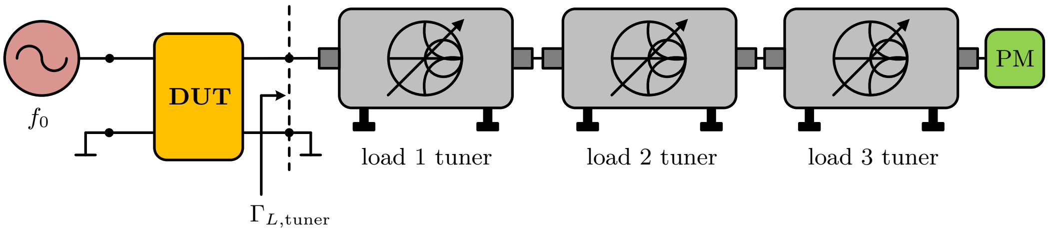

Figure 2.11: Block diagram of a typical cascaded harmonic tuning load-pull setup.

fundamental frequency $\Gamma^{(f_0)}_{L,tuner}$, second order $\Gamma^{(2f_0)}_{L,tuner}$, and third order harmonic $\Gamma^{(3f_0)}_{L,tuner}$ are shown. Each load reflection coefficient is comprised by the superposition of the reflection coefficients of all involved tuners. Compared to the triplexer based setup, this approach allows to achieve a higher tuning range, because the losses are lower. However, in practice, tuning sensitivity is an issue. Since each tuner is typically realized by a mechanic slide-screw tuner, mechanical tolerances are involved. By adjusting multiple tuners in a cascaded connection, these tolerances sum up and my cause a different realization of the load reflection coefficient when trying to repeat the tuner setting to the same load condition.

If very high tuning range is needed, active tuning load-pull is the method of choice [43]. There, the load reflection coefficient is realized by applying a defined input signal at the output of the DUT. This allows to achieve output reflection coefficients with a magnitude even bigger than one. A block diagram of such a setup is depicted in Figure 2.13. There are several different approaches possible for an active load-pull setup, in this graph an open-loop setup is shown [42]. Different to the passive setup, the first element at the output is an isolator, to protect the subsequent components from damage. In order to achieve an input

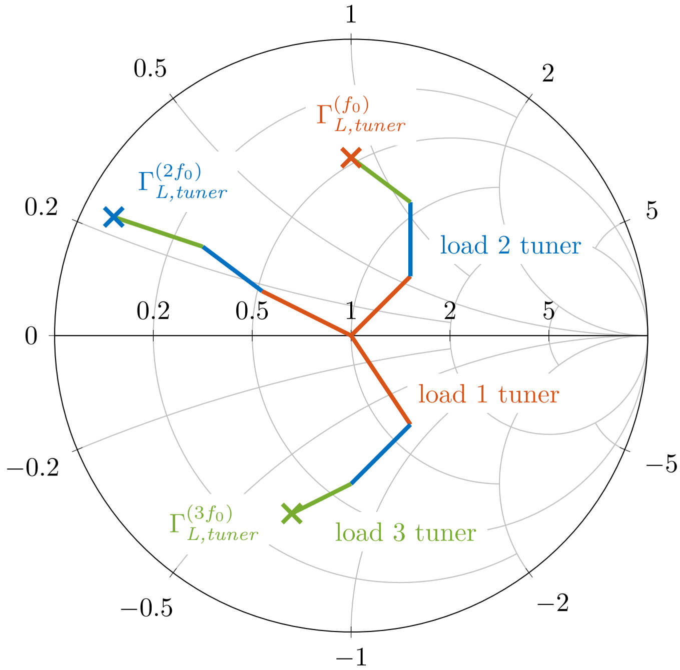

Figure 2.12: Realization of the load reflection coefficient using a cascaded harmonic tuning setup.

signal at the output, an RF source is used, which has to be coherent with the actual input source for the DUT. To get a defined signal power an amplifier and an adjustable attenuator is implemented to the setup. To adjust the phase, an adjustable phase shifter is used afterwards. Consequently, typically any desired refection coefficient can be applied at the DUT's reference plane. Such setups can also be expanded to harmonic tuning in combination with a multiplexer. The drawback is that a comprehensive setup is necessary, which leads to high setup costs, especially for high power applications. Also the accuracy strongly depends on the coherence of the involved sources, which is often tricky in practice.

Load-pull measurements are widely used in PA design, since they allow to determine optimum loads for the non-linear matching problem for a dedicated DUT. An inherent drawback is, that only scalar measurements, e.g. power, subject to a certain load and source impedance, are possible. In many cases this is unsatisfactory, because a vectorial description of the measurement quantities is desired. However, in combination with state-of-the-art VNAs, load-pull measurements are widely used during model extraction of more advanced measurement based models, which are discussed as follows.

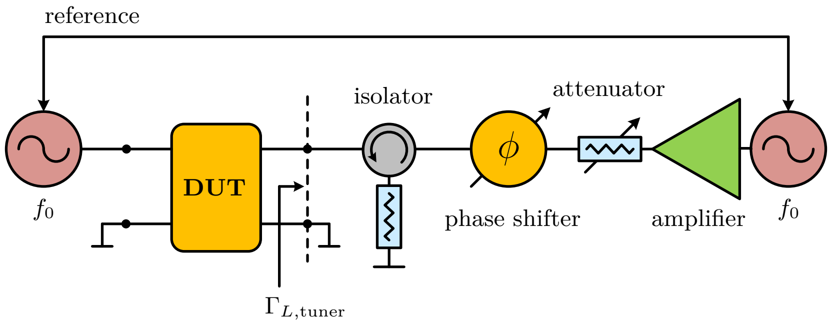

Figure 2.13: Block diagram of a typical open-loop active load-pull setup.

2.4.2 Hot S-parameters

Over the years, RF engineers tried to overcome the limitations of S-parameters to find a similar approach for non-linear DUTs, since defining relations between the incident and outgoing waves a and b is generally not limited to the linear domain. Therefore, attempts have been made to extend the concept of S-parameters to the large-signal domain, which have been called "hot S-parameters" or "large-signal S-parameters" [44]. The goal for this is to be able to handle non-linearities, while still using the S-parameter framework.

As described in [45], several approaches have been made to define hot S-parameters. These different formulations have been motivated by different design problems, supposed to be described by hot S-parameters [45]. For simplicity, only the most basic formulation will be discussed here.

The basic idea is to describe the behavior of a DUT under realistic operational conditions, i.e., when a persistant large-signal stimulus a_1 is present at the carrier frequency f_0. Equivalent to linear S-parameters, a relationship between the traveling waves a and b is desired. Therefore, an additional small CW probing tone is applied at the excitation frequency f_0 [44, 46, 47]. Similar to linear S-parameters, the relationship can be written as

$$\begin{pmatrix} b_1 \\ b_2 \end{pmatrix} = \begin{pmatrix} \mathrm{hot}S_{11} & \mathrm{hot}S_{12} \\ \mathrm{hot}S_{21} & \mathrm{hot}S_{22} \end{pmatrix} \cdot \begin{pmatrix} a_1 \\ a_2 \end{pmatrix}. \tag{2.12}$$

In order to determine hot S-parameters, the presence of the necessary probing tone leads to a more complicated situation than for the linear case, hence a VNA cannot be used in its standard configuration. In order to provide the persistent large-signal stimulus and the additional probing tone, two sources are necessary. This can be realized by providing the large-signal tone using a power combiner, as depicted in the block diagram in Figure 2.14. Note that the receivers of the VNA in this graph are denoted as A, B, R1, and R2 with is according to the notation of *Keysight Technologies*. This notation was used for all block diagrams in this thesis for the sake of consistency.

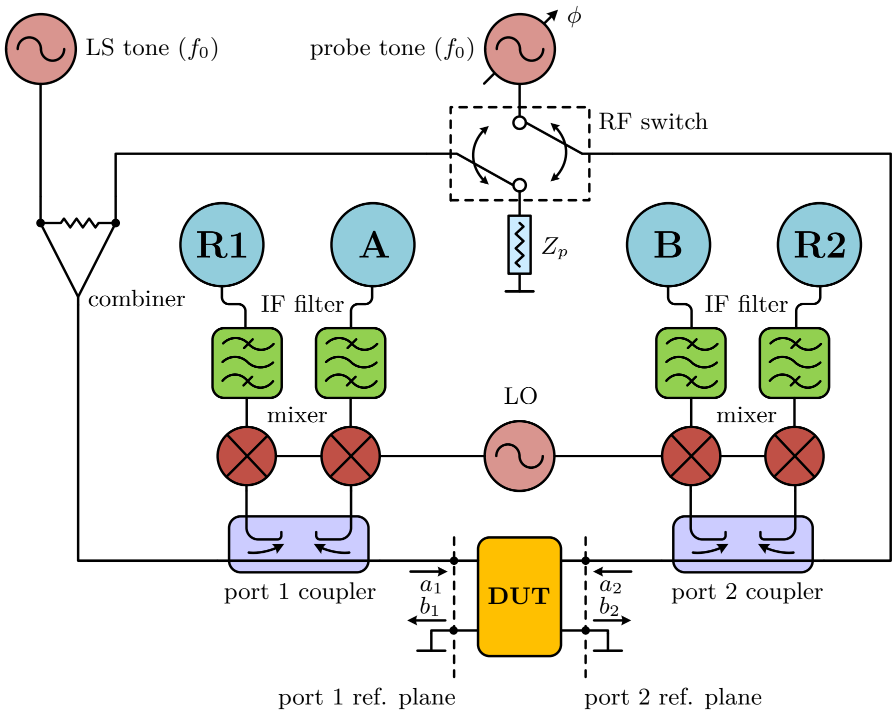

Figure 2.14: Block diagram of a VNA including a second source, applicable for hot S-parameter measurements.

Due to the presence of a second input tone, the hot S-parameters cannot easily be separated during the measurements. Consequently, they will appear in the following form:

$$\frac{b_1}{a_1} = \mathrm{hot}S_{11} + \mathrm{hot}S_{12}\frac{a_2}{a_1} \tag{2.13a}$$

$$\frac{b_1}{a_2} = \mathrm{hot}S_{11}\frac{a_1}{a_2} + \mathrm{hot}S_{12} \tag{2.13b}$$

$$\frac{b_2}{a_1} = \mathrm{hot}S_{21} + \mathrm{hot}S_{22}\frac{a_2}{a_1} \tag{2.13c}$$

$$\frac{b_2}{a_2} = \mathrm{hot}S_{21}\frac{a_1}{a_2} + \mathrm{hot}S_{22}. \tag{2.13d}$$

If $|a_1|$ and $|a_2|$ are constant, each quantity $\frac{b_i}{a_j}$, in which $(i,j) \in \{1,2\}$, leads to a circle in the corresponding $\frac{b_i}{a_j}$ plane, if the phase between $|a_1|$ and $|a_2|$ is changed

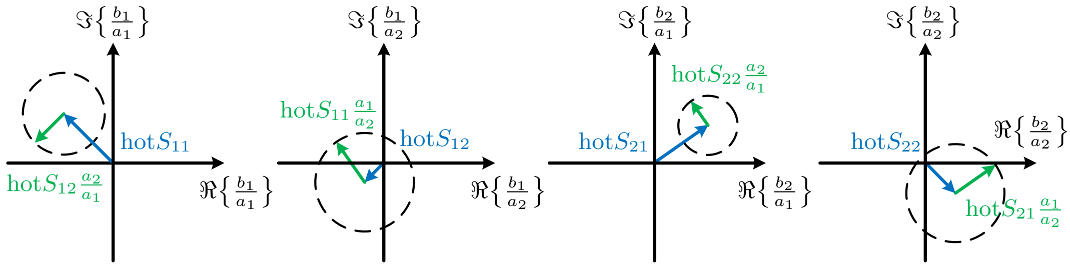

Figure 2.15: Circular locii of the quantities $\frac{b_i}{a_j}$ as a function of $\frac{a_i}{a_j}$, observed during hot S-parameter measurements [44].

[44]. This is shown in Figure 2.15. Consequently, the quantities for the hot S-parameters can be determined by finding the center of the corresponding circle.

As discussed in [48], hot S-parameters are beneficial for describing non-linear DUTs. However, for an increasing degree of non-linearity, the model fails in accurately describing the observed behavior. Furthermore, harmonics are not taken into account, which are a very important in the non-linear case. However, based on the hot S-parameter framework models have emerged, which tackle these limitations. These are discussed in the following sections.

2.4.3 Volterra Input Output Mapping

As discussed in Section 2.3.1 the Volterra series can be transformed to the frequency-domain. This leads to Volterra kernels in the frequency-domain as

$$h_n(\tau_1, \cdots, \tau_n) \circ\!\!-\!\!\bullet\, H_n(\omega_1, \cdots, \omega_n) \tag{2.14}$$

and the convolution integrals turn into multiplications in the frequency-domain as

$$\begin{aligned}&\int\limits_0^\infty \cdots \int\limits_0^\infty h_n(\tau_1, \tau_2, \cdots, \tau_n) x(t-\tau_1) x(t-\tau_2) \cdots x(t-\tau_n) d\tau_1 \cdots d\tau_n \\ &\circ\!\!-\!\!\bullet\, H_n(\omega_1, \cdots, \omega_n) X(\omega_1) \cdots X(\omega_n).\end{aligned} \tag{2.15}$$

The benefit of the frequency-domain representation is in its intuitive interpretation, e.g., intermodulation distortion at the frequency $2\omega_1 + \omega_2$ is directly proporional to the Volterra kernel $H_3(\omega_1, \omega_1, \omega_2)$. Furthermore, it is easier to measure the frequency-domain kernels [32].

The frequency domain representation of the Volterra series serves as a basis for the Volterra input output mapping (VIOMAP) approach. Equivalent to S-parameters, traveling waves a and b are used as input and output quantities with the difference, that they are generally non-linear for the VIOMAP approach [49]. Hence, the frequency-domain Volterra kernels for the VIOMAP are defined as $H_{n,pq_1q_2\cdots q_n}(f_1, f_2, \cdots, f_n)$. These describe the contribution of a non-linearity with degree n, combining the frequencies f_i at port q_i, into the frequency components $f_1 + f_2 + \cdots + f_n$ to the resulting wave at port p.

An example of a device containing a third order non-linearity is presented in [49] and [50], which can be described by a VIOMAP as

$$\begin{aligned}
b_1(f_1) =& H_{1,11}a(f_1) + H_{1,12}(f_1)a_2(f_1) \\
&+3H_{3,1111}(f_1, f_1, -f_1)a_1(f_1)a_1(f_1)a_1(-f_1) \\
&+3H_{3,1112}(f_1, f_1, -f_1)a_1(f_1)a_1(f_1)a_2(-f_1) \\
&+6H_{3,1112}(f_1, -f_1, f_1)a_1(f_1)a_1(-f_1)a_2(f_1) \\
&+6H_{3,1122}(f_1, f_1, -f_1)a_1(f_1)a_2(f_1)a_2(-f_1) \\
&+3H_{3,1122}(-f_1, f_1, f_1)a_1(-f_1)a_2(f_1)a_2(f_1) \\
&+3H_{3,1222}(f_1, f_1, -f_1)a_2(f_1)a_2(f_1)a_2(-f_1) \\
b_1(3f_1) =& 3H_{3,1112}(f_1, f_1, f_1)a_1(f_1)a_1(f_1)a_2(f_1) \\
&+3H_{3,1122}(f_1, f_1, f_1)a_1(f_1)a_2(f_1)a_2(f_1) \\
&+H_{3,1222}(f_1, f_1, f_1)a_2(f_1)a_2(f_1)a_2(f_1).
\end{aligned} \tag{2.16}$$

Note that $x(-f_1) = x^*(f_1)$. If this device is linear, all third order kernels are zero, i.e., Equation (2.16) simplifies to

$$\begin{aligned}
b_1(f_1) =& H_{1,11}a(f_1) + H_{1,12}(f_1)a_2(f_1) \\
b_1(f_1) =& 0.
\end{aligned} \tag{2.17}$$

Here, the relationship to S-parameters can clearly be seen. Hence, it is shown that for a linear device the first order kernels $H_{1,pq}(f_1)$ are equal to $S_{pq}(f_1)$.

For the measurement of the VIOMAP, the excitation signal has to be varied considerably. Its amplitude and frequency is therefore randomly chosen over the desired range of interest [49]. In order to be able to extract the full VIOMAP, two independent sources are necessary to provide a stimulus at both ports, i.e., the incident waves a_1 and a_2. To determine the harmonic response, a VNNA is used, which is basically a 4-channel harmonic sampler. Note that this was the first name in literature, which was used for such an instrument. More details on variations and types of such VNNAs can be found in Chapter 4.

A block diagram of a typical measurement setup is depicted in Figure 2.16. As can be seen in the block diagram, two RF sources are used, whose amplitude and phase can be adjusted using the signal combining and conditioning block, for providing the necessary stimuli at both ports. This is very similar to an active load-pull setup, as discussed in Section 2.4.1. As a VNNA in this block

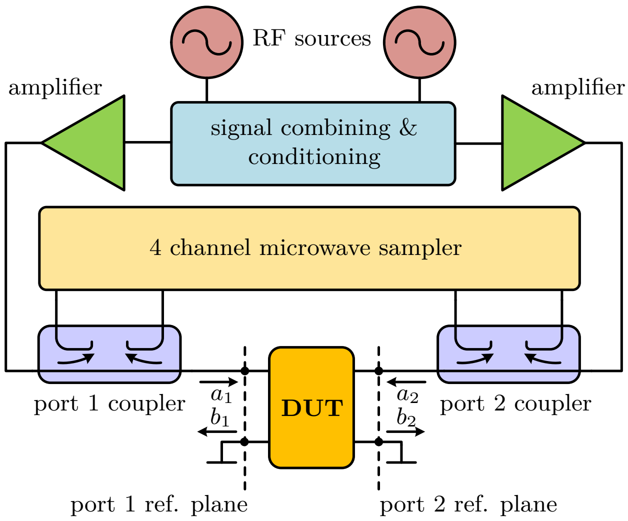

Figure 2.16: Block diagram of a measurement setup, able to extract a VIOMAP, a "vectorial non-linear network analyzer" [50].

diagram a microwave sampler is used, which is able to measure the full harmonic response. With the measurements the VIOMAP can be extracted by using non-linear parameter estimation techniques, e.g. the Newton-Raphson algorithm [49].

The VIOMAP offers a technically sound model to describe a non-linear system as a black box [49]. However, equivalent to the time-domain Volterra series, this approach is only suited for modeling weakly non-linear devices [51]. For hard non-linearities the required degree n gets large, i.e., the determination of the kernels requires solving an ill-conditioned set of equations which makes the model extraction procedure impractical. Since hard non-linear operations are common especially in RF circuit design, this approach is not very feasible for a general black-box behavioral model.

2.4.4 Polyharmonic Distortion Modeling

As discussed in the previous sections, a black-box behavioral model for non-linear DUTs, similar to S-parameters, is desired. Different approaches have been proposed to find an appropriate description, but all those approaches still have severe limitations to some extent. The VIOMAP seems promising at the first glance, however it is limited to weakly non-linear systems and the extraction is complicated. Also hot S-parameters seem promising, but they are not able to describe the harmonic response.

To be able to model strongly non-linear behavior, so-called *describing functions* are better suited than a power series [52, 53]. The idea behind this describing function approach is, that each spectral output component of a non-linear DUT can be described as an, in general, complex function of all spectral input components. Utilizing the traveling waves description, the output or outgoing wave b_{pk} of a given DUT at port p and harmonic index k can be described as a function of the incident wave a, applied at the input port q and harmonic index l. Mathematically, this can be written as

$$b_{pk} = F_{pk}(a_{11}, a_{12}, \cdots, a_{21}, a_{22}, \cdots, a_{ql}), \tag{2.18}$$

where F_{pk} denotes these multivariate complex functions, the so-called describing functions. They describe the spectral mapping of all the involved signals. Using this approach, any signal component, i.e., the fundamental frequency and the harmonics, can be described accurately. An example is shown in Figure 2.17. It shows a non-linear DUT under CW excitation and arbitrary load conditions

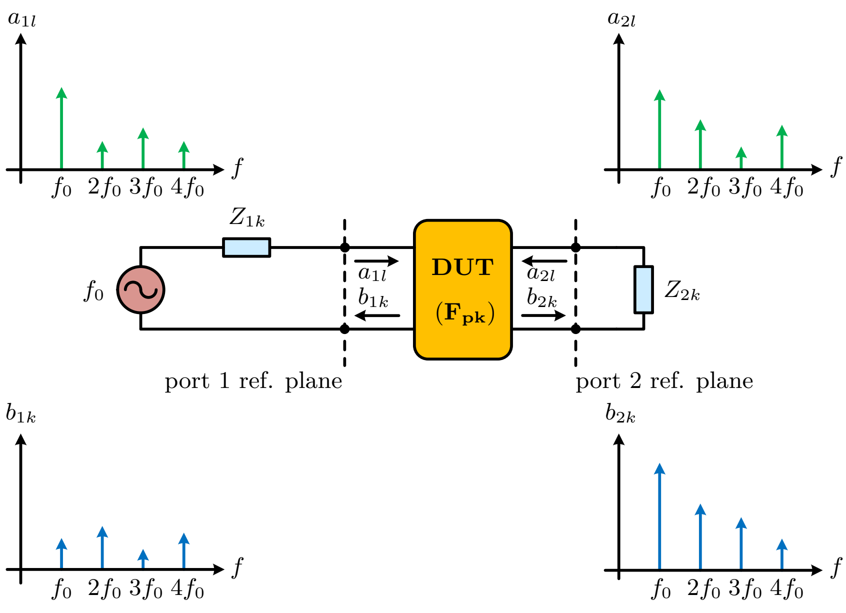

Figure 2.17: Non-linear 2-port with arbitrary loads under CW excitation at f_0.

Z_{pk} at each involved frequency point. Consequently, a large number of frequency components are involved at the input and output. Because a CW excitation is used, the traveling waves show components at multiples of the fundamental frequency f_0, i.e. the harmonic grid. Note that also the input signal shows signal components all over the harmonic grid, which is due to the assumed arbitrary source and load impedances, which may cause reflections.

Since these describing functions are time-invariant [54], phase normalization can be applied, which is done by using the phase of the fundamental input a_{11}.

Therefore, the phasor P is introduced as

$$P = \frac{a_{11}}{|a_{11}|} = e^{j\underline{/a_{11}}}. \tag{2.19}$$

Hence, Equation (2.18) can be reformulated as

$$b_{pk} = F_{pk}\Big(|a_{11}|, a_{12}P^{-2}, \cdots, a_{21}P^{-1}, a_{22}P^{-2}, \cdots\Big)P^{k}. \tag{2.20}$$

The describing functions approach can be used for a description of the behavior of the DUT, but for a comprehensive description it would end up in a huge set of functions, which is impractical for model extraction and simulation. To simplify this description, a new modeling approach was developed, which is called polyharmonic distortion (PHD) modeling [55]. This framework is closely related to hot S-parameters [48], however, PHD modeling allows for better accuracy for non-liner DUTs, as will be discussed as follows.

For the PHD modeling approach the describing functions are approximated in order to make them more useful in practice. Therefore, several assumptions are made: In many applications, especially PAs with a narrow-band input stimulus, only one dominant large-signal input tone is present, i.e. a_{11}. All other input components are relatively small, hence, they can be seen as additional small-signal input tones. Therefore, Equation (2.20) can be linearized for all components beside the large-signal input tone. This allows to utilize the superposition principle, which would not be possible for the original describing function in Equation (2.20). At the first glance, this seems unusual because of the involved non-linearity. However, this was experimentally verified in [56] and is called the "harmonic superposition principle". A graphical illustration is depicted in Figure 2.18. There, a DUT is excited with a large-signal CW stimulus

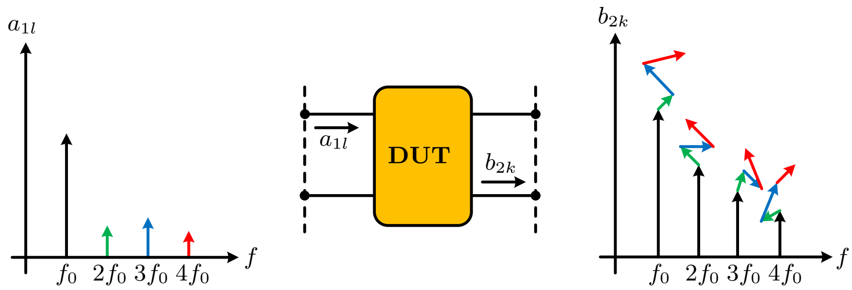

Figure 2.18: Graphical representation of the harmonic superposition principle [56].

at the fundamental frequency f_0, i.e., an incident wave a_{11}. This stimulus causes a harmonic response at port 2, which generally consists of tones at multiples of f_0.

Additionally, small-signal input tones at port 1 are considered in this example. In order not to violate the harmonic superposition principle, these tones have to be much smaller than the large-signal input tone a_{11}. Each of this input tones will generally cause a response at each frequency on the harmonic grid. Consequently, there exist functions, which describe the mapping between different frequencies, which is often called spectral mapping. As schematically illustrated in Figure 2.18, each actual output component b_{pk} consists of a superposition of the large-signal response and the responses from the additional small-signal input due to the harmonic superposition principle.

The linearization of Equation (2.20) is performed similar to a Taylor series expansion [57], so it can be rewritten as

$$\begin{aligned} b_{pk} =& K_{pk}(|a_{11}|)P^k \\ &+ \sum_{ql} G_{pk,ql}(|a_{11}|)P^k \cdot \Re\{a_{ql}P^{-l}\} \\ &+ \sum_{ql} H_{pk,ql}(|a_{11}|)P^k \cdot \Im\{a_{ql}P^{-l}\}, \end{aligned} \tag{2.21}$$

with

$$K_{pk}(|a_{11}|) = F_{pk}(|a_{11}|, 0, \cdots, 0), \tag{2.22a}$$

$$G_{pk,ql}(|a_{11}|) = \left.\frac{\partial F_{pk}}{\partial \Re\{a_{ql}P^{-l}\}}\right|_{|a_{11}|, \underset{\{q,l\}\neq\{1,1\}}{\forall} a_{ql}=0}, \tag{2.22b}$$

$$H_{pk,ql}(|a_{11}|) = \left.\frac{\partial F_{pk}}{\partial \Im\{a_{ql}P^{-l}\}}\right|_{|a_{11}|, \underset{\{q,l\}\neq\{1,1\}}{\forall} a_{ql}=0}. \tag{2.22c}$$

Again, for convenience, the indices are defined as

p . . . output port index

k . . . output frequency index

q . . . input port index

l . . . input frequency index.

The result in Equation (2.21) is analog to the harmonic superposition principle shown in Figure 2.18, with the parameters K_{pk} describing the non-linear mapping and the parameters $G_{pk,ql}$ and $H_{pk,ql}$ describe the spectral mapping between the frequencies on the harmonic grid. Note that the real and imaginary part of the input argument a_{ql} are treated independently in the approximation. This is due to the non-analytic nature of the describing function F_{pk} [55].

Equation (2.21) can again be rewritten by substituting the real and imaginary parts of the input arguments with

$$\begin{aligned}\Re\{a_{ql}P^{-l}\} &= \frac{a_{ql}P^{-l} + \left(a_{ql}P^{-l}\right)^*}{2} \\ \Im\{a_{ql}P^{-l}\} &= \frac{a_{ql}P^{-l} - \left(a_{ql}P^{-l}\right)^*}{2j},\end{aligned} \tag{2.23}$$

forming a simple PHD model equation as

$$\begin{aligned}b_{pk} = &\sum_{ql} S_{pk,ql}(|a_{11}|)P^{k-l} \cdot a_{ql} \\ &+ \sum_{ql} T_{pk,ql}(|a_{11}|)P^{k+l} \cdot a_{ql}^*.\end{aligned} \tag{2.24}$$

This is done by the introduction of two new parameters, $S_{pk,ql}$ and $T_{pk,ql}$, which are defined as

$$S_{pk,11}(|a_{11}|) = \frac{K_{pk}(|a_{11}|)}{|a_{11}|} \tag{2.25a}$$

$$T_{pk,11}(|a_{11}|) = 0 \tag{2.25b}$$

$$\forall (q,l) \neq (1,1): \tag{2.25c}$$

$$S_{pk,ql}(|a_{11}|) = \frac{G_{pk,ql}(|a_{11}|) - jH_{pk,ql}(|a_{11}|)}{2} \tag{2.25d}$$

$$T_{pk,ql}(|a_{11}|) = \frac{G_{pk,ql}(|a_{11}|) + jH_{pk,ql}(|a_{11}|)}{2} \tag{2.25e}$$

The parameters $T_{pk,11}$ are defined as being equal to 0, which can be explained by the fact that

$$P^{k-1}a_{11} = P^{k+1}a_{11}^* = |a_{11}| \tag{2.26}$$

This means that only the sum $S_{pk,11} + T_{pk,11}$ matters in this case, so $T_{pk,11}$ is set to zero by convention [55].

The basic PHD model is very similar to hot S-parameters, i.e., a frequency domain mapping of the outgoing waves b_{pk} from the incident waves a_{ql}. However, there are some main differences, which are going beyond the extension to a non-linear mapping over the whole harmonic grid. When considering the simple case of b_{21} only depends on the fundamental frequency input at f_0, i.e., a_{21} and the persistent large-signal input $|a_{11}|$, Equation (2.24) is reduced to

$$b_{21} = S_{21,11}(|a_{11}|) \cdot a_{21} + S_{21,21}(|a_{11}|) \cdot a_{21} + T_{21,21}(|a_{11}|)P^2 \cdot a_{21}^*. \tag{2.27}$$

Differently to hot S-parameters, the conjugate term $T_{21,21}$ is present in the PHD model. The effect of these conjugate terms is illustrated in Figure 2.19. On the left side, Figure 2.19a, a typical model response without conjugate terms is depicted. Note that similar behavior can be seen in Figure 2.15, showing hot S-parameters graphically. For increasing input power, i.e., increasing a_{11}, the DUT becomes increasingly non-linear. One would expect non-linear distortion, hence, compression. However, the model shows only shrinking smiley-faces for increasing power. By the introduction of the conjugate terms, the model shows much better agreement with the reality since distortion effects can be modeled, as depicted in the right part, i.e. Figure 2.19b. This tackles the limitation which

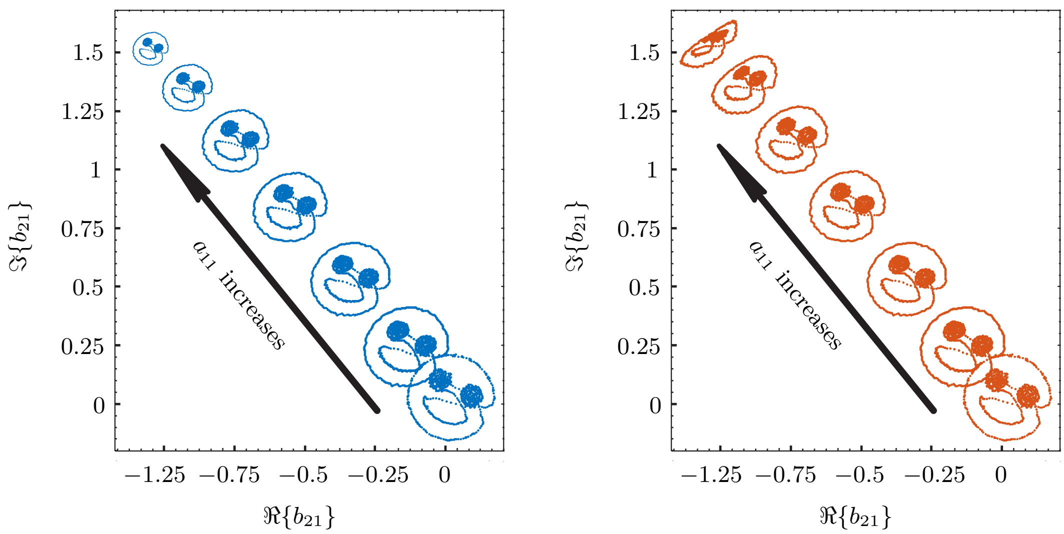

(a) Without conjugate terms (b) With conjugate terms

Figure 2.19: Comparioson of the trajectories of b_{21}, with and without conjugate terms [48, 55].

arose with the concept of hot S-parameters, which do not utilize the conjugate terms. Furthermore, the expansion to higher order harmonics allows to predict the full non-linear behavior of a DUT. Compared to the VIOMAP approach, there are similarities, but the parameters involved are more intuitive. While the parameters $S_{pk,ql}$ show close similarities to S-parameters, the parameters $T_{pk,ql}$ are strongly related to the non-linearity of the DUT. This means, that for a DUT operating close to the linear regime, the parameters $T_{pk,ql}$ are very small, while they are increasing for a greater degree of non-linearity.

Several models have been developed using PHD modeling as a basis. In combination with an appropriate measurement instrument, they are commercially available, similar to S-parameters and the VNA. One approach are S-functions by *NMDG* [58]. They are formulated as

$$
\begin{aligned}
b_{pk} &= Sf_{pk11}|a_{11}| \\
&\quad + \sum_{(q,l)\neq(1,1)} \left(Sf_{pk,ql} a_{ql} + Sfc_{pk,ql} a_{ql}^{*} \right).
\end{aligned}
\tag{2.28}
$$

The close relationship to PHD modeling is evident, hence, a more detailed explanation is not necessary here. Furthermore, they are not very often used any more. To the author's knowledge this is mainly due to the superior measurement framework available for X-parameters, which is *Keysight's* PHD based modeling approach. X-parameters have become a popular model and are widely used in RF engineering. Consequently, they are discussed in more detail in Chapter 3. From a mathematical point-of-view, X-parameters can be seen as a reformulation of S-functions [59], but the out-of-the-box measurement solution provided by *Keysight's PNA-X* allows for an easier model extraction. More details on non-linear measurement instruments can be found in Chapter 4.

For the extraction of the PHD model different techniques exist, like the offset frequency or the offset phase technique. These techniques can be used for all PHD based models and are discussed in Section 3.4.

Besides their benefits, PHD based models have limitations due to the linearization of the describing functions. Consequently, they fail for strongly non-linear DUTs in highly mismatched environments, due to the underlying assumption of only one single large-signal input tone. In such highly mismatched environments, it can happen that reflections cause large input tones. These may violate the harmonic superposition principle, hence, the model error will tend to get large.

2.4.5 Cardiff Model

The Cardiff model has evolved over time, therefore, different formulations have been proposed. It was initially proposed as a direct waveform look-up (DWLU) or "truth look-up model" model [60]. Therefore, the full non-linear response was gained by performing large-signal measurements from a DUT and deployed to a CAD software. The background of this approach was to find an accurate description for a DUT for PA design, since equivalent circuit based models either do not offer the necessary accuracy for state-of-the-art highly efficient PA architectures, or are not available for a certain DUT.

To gain the model, a 2-port as in Figure 2.20 is considered. For a specific load impedance Z_{Load}, the currents at port 1 and 2 can be defined in the frequency-

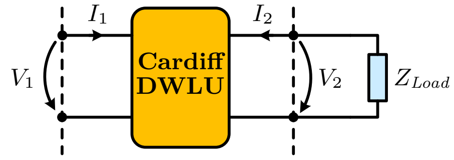

Figure 2.20: Cardiff DWLU model block diagram.

domain as

$$I_1(\omega) = A_0 \cdot \delta(\omega) + \sum_{k=1}^{K} A_k \cdot V_1^k(\omega) \cdot \delta(\omega - 2\pi k f_0) \tag{2.29a}$$

$$I_2(\omega) = B_0 \cdot \delta(\omega) + \sum_{k=1}^{K} B_k \cdot V_1^k(\omega) \cdot \delta(\omega - 2\pi k f_0), \tag{2.29b}$$

whereas V_1^k denotes the input CW stimulus, f_0 the fundamental frequency, and k the harmonic index. A_k and B_k are the model coefficients and K is the maximum harmonic order. In order to get a valid device representation it is necessary to measure the DUT for a wide range of loads, i.e., load-pull measurements over a wide load-pull grid.

The accuracy of the DWLU model relies on interpolation techniques, which leads to several limitations. For having a model which shows good agreement with the DUT over a wide range of input powers or bias points, the model size tends to get large. This may lead to low computational efficiency, hence, the model was expanded to a behavioral model approach based on polynomials [61]. This has similarities to a Volterra series approach in the frequency domain.

For the behavioral modeling approach, describing functions are used to model the considered DUT. As shown in Equation (2.30), this is done by describing the outgoing waves b_1 and b_2 as functions of the incident waves a_1 and a_2, at the fundamental frequency f_0.

$$b_1 = f(a_1, a_2) \tag{2.30a}$$

$$b_2 = g(a_1, a_2) \tag{2.30b}$$

For the model generation, the function is approximated by a polynomial of complex coefficients ϕ and θ. This allows to find a mathematically robust formulation for the involved non-linearity as

$$b_1 = \phi_{10}a_1 + \phi_{01}a_2 + \phi_{11}a_1a_2 + \cdots + \phi_{n1n2}a_1^{n_1}a_2^{n_2} \tag{2.31a}$$

$$b_2 = \theta_{10}a_1 + \theta_{01}a_2 + \theta_{11}a_1a_2 + \cdots + \theta_{n_1n_2}a_1^{n_1}a_2^{n_2}, \tag{2.31b}$$

with the order n of the combined polynomial is the sum of degree n_1 and n_2. Theoretically, Equation (2.31) allows to accurately model any kind of non-linearity, if the order of the polynomial is sufficiently high. Initially, the order of the Cardiff model was limited to $n = 3$ to limit the model's complexity [61]. Hence, Equation (2.31) is reformulated as [62]

$$b_1 = \phi_{10}a_1 + \phi_{01}a_2 + \phi_{11}a_1a_2 + \cdots + \phi_{30}a_1^3 + \phi_{03}a_2^3 \tag{2.32a}$$
$$b_2 = \theta_{10}a_1 + \theta_{01}a_2 + \theta_{11}a_1a_2 + \cdots + \theta_{30}a_1^3 + \theta_{03}a_2^3. \tag{2.32b}$$

As can be seen in Equation (2.32), a lot of harmonic products are generated. By focusing on the fundamental component only, Equation (2.32) can be reduced to:

$$\begin{aligned} b_1 =& \left(\phi_{10} + 3\phi_{30}|a_1|^2 + \phi_{12}|a_2|^2 + \phi_{21}|a_1||a_2| \cdot \frac{Q}{P}\right)a_1 \\ &+ \left(\phi_{01} + 3\phi_{03}|a_2|^2 + \phi_{21}|a_1|^2 + \phi_{12}|a_1||a_2| \cdot \frac{P}{Q}\right)a_2 \end{aligned} \tag{2.33a}$$

$$\begin{aligned} b_2 =& \left(\theta_{10} + 3\theta_{30}|a_1|^2 + \theta_{12}|a_2|^2 + \theta_{21}|a_1||a_2| \cdot \frac{Q}{P}\right)a_1 \\ &+ \left(\theta_{01} + 3\theta_{03}|a_2|^2 + \theta_{21}|a_1|^2 + \theta_{12}|a_1||a_2| \cdot \frac{P}{Q}\right)a_2, \end{aligned} \tag{2.33b}$$

or

$$b_1 = \left(C_{1,0} + C_{1,1} \cdot \frac{Q}{P}\right)a_1 + \left(U_{1,0} + U_{1,1} \cdot \frac{P}{Q}\right)a_2 \tag{2.34a}$$
$$b_2 = \left(C_{2,0} + C_{2,1} \cdot \frac{Q}{P}\right)a_1 + \left(U_{2,0} + U_{2,1} \cdot \frac{P}{Q}\right)a_2. \tag{2.34b}$$

Interestingly, the parameters C and U only depend on the magnitudes of the input traveling waves a_1 and a_2. The phase terms are fully separated and defined as:

$$P = \frac{a_1}{|a_1|} = e^{j\underline{/a_1}} \tag{2.35a}$$
$$Q = \frac{a_2}{|a_2|} = e^{j\underline{/a_2}}. \tag{2.35b}$$

This decoupling of the phase dependencies reduces the complexity of the model dramatically and makes the model parameter easier to extract [62].

The described model is very similar to the PHD model. This can be seen more easily by using a slightly different formulation of the model as

$$\begin{aligned} b_1 =& (\phi_{10} + 3\phi_{30}|a_1|^2 + \phi_{12}|a_2|^2)a_1 + (\phi_{12}|a_2|^2)a_1^*Q^2 \\ &+ (\phi_{01} + 3\phi_{03}|a_2|^2 + \phi_{21}|a_1|^2)a_2 + (\phi_{21}|a_1|^2)a_2^*P^2 \end{aligned} \tag{2.36a}$$

$$\begin{aligned} b_2 =& (\theta_{10} + 3\theta_{30}|a_1|^2 + \theta_{12}|a_2|^2)a_1 + (\theta_{12}|a_2|^2)a_1^*Q^2 \\ &+ (\theta_{01} + 3\theta_{03}|a_2|^2 + \theta_{21}|a_1|^2)a_2 + (\theta_{21}|a_1|^2)a_2^*P^2. \end{aligned} \tag{2.36b}$$

This alternative formulation can be rewritten using the alternative parameters S and T [63]:

$$b_1 = S_{11}a_1 + T_{11}a_1^* Q^2 + S_{12}a_2 + T_{12}a_2^* P^2 \tag{2.37a}$$

$$b_2 = S_{21}a_1 + T_{21}a_1^* Q^2 + S_{22}a_2 + T_{22}a_2^* P^2. \tag{2.37b}$$

Equation (2.37) is very similar to the PHD formulation discussed in Section 2.4.4, hence, the PHD model is similar to this formulation of the Cardiff model with order $n = 3$. However, there are two main differences to the original PHD formulation. Firstly, the parameters S and T in the PHD approach are a function of $|a_1|$, while for the Cardiff model approach $|a_1|$ and $|a_2|$ are relevant. Secondly, T_{11} and T_{21} do not exist in the PHD model. This is because the Cardiff model is derived without assuming the validity of the harmonic superposition principle. Consequently, the influence of a_2 has to be taken into account. The original PHD model can therefore be interpreted as a special case if the magnitude of a_2 is sufficiently small, hence T_{11} and T_{21} converges to zero [62].

By considering higher order non-linearity, Equation (2.32) can be generalized. If an n^{th} order polynomial is used, see Equation (2.31), the model is rewritten in a more general form [61]

$$b_p = \sum_{n=0}^{\frac{N-1}{2}} C_{p,n} \cdot \left(\frac{Q}{P}\right)^n a_1 + \sum_{n=0}^{\frac{N-1}{2}} U_{p,n} \cdot \left(\frac{P}{Q}\right)^n a_2, \tag{2.38}$$

with p represents the port number and N the order used in the polynomial. Note that the maximum order N has to be an odd integer number, because an even-order term does not generate any component at the fundamental [61].

The described model (Equation (2.38)) has been extended to add harmonic complexity, in order to account for fundamental and second harmonic load-pull [64]. Therefore, describing functions are used as a starting point. Again, the input waves can be written in polar form and therefore, the absolute phase is removed from the function. This is described as

$$b_{p,k} = f_{p,k}(a_{1,1}, a_{2,1}) = P_1^k \cdot g_{p,k}\left(|a_{1,1}|, |a_{2,1}|, \left(\frac{Q_1}{P_1}\right)\right), \tag{2.39}$$

again utilizing separation between magnitude and phase in order to simplify the model extraction [64]. Due to the applied phase normalization, a very important property can be used to approximate this function. The phase vector $\frac{Q_1}{P_1}$ is a periodic function, i.e., $b_{p,k}$ is also periodic [64]. Therefore, a Fourier series with respect to the phase vector $\frac{Q_1}{P_1}$ can be determined as

$$b_{p,k} = P_1^k \sum_{n=-\frac{N-1}{2}}^{\frac{N+1}{2}} \left[R_{p,k,n}\Big(|a_{1,1}|, |a_{2,1}|\Big)\left(\frac{Q_1}{P_1}\right)^n\right], \tag{2.40}$$

where $R_{p,k,n}$ are the coefficients of the Fourier series and N denotes the mixing order or complexity.

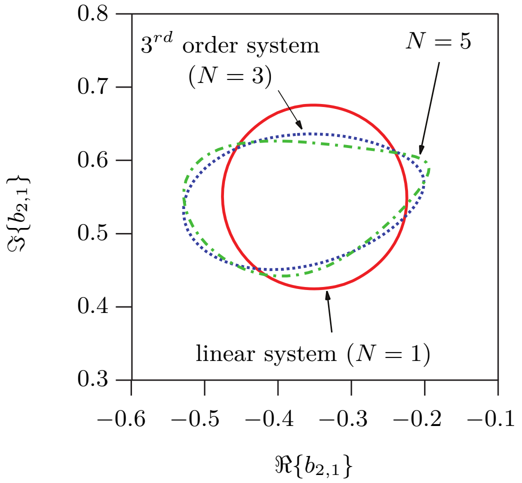

(a) Behavioral response $b_{2,1}$ depending on the model order

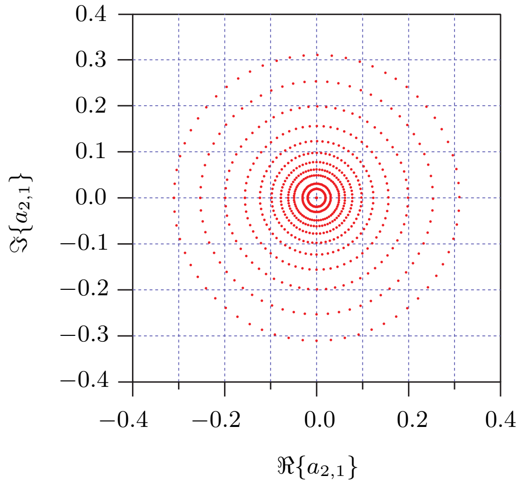

(b) Stimulus at port 2

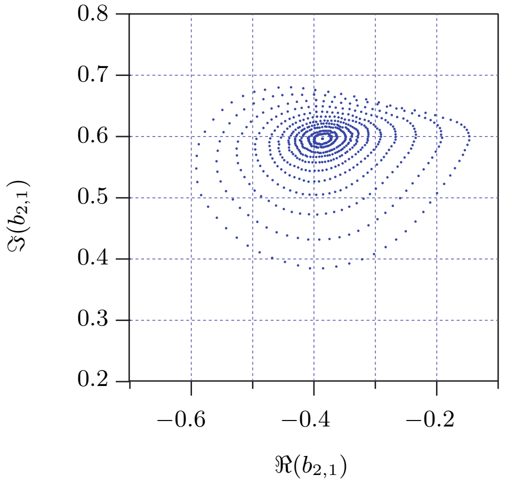

(c) Measured response $b_{2,1}$of the DUT

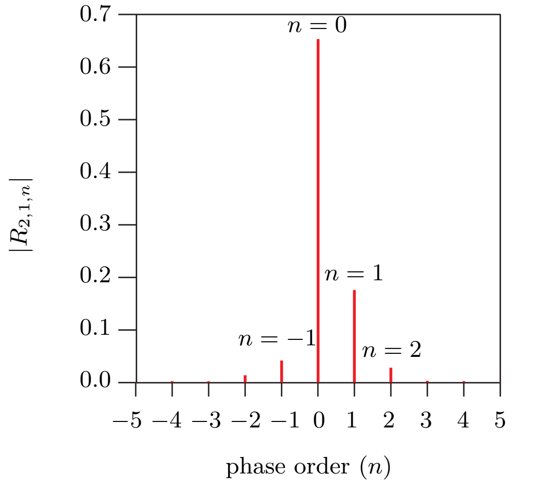

(d) Magnitude of the behavioral model spectral components

Figure 2.21: Measured response of the periodic phase stimulus compared to the behavioral model. The figure is taken from [65].

In Figure 2.21, the approach from Equation (2.40) is demonstrated. In Figure 2.21a, the responses $b_{2,1}$ as a function from the phase vecor $\frac{Q_2}{P_1}$ is depicted. It can be seen, that the higher the degree of non-linearity, the higher the complexity

N has to be in order to allow for an accurate description. In Figure 2.21b, an example stimulus $a_{2,1}$ is depicted, with periodic sinusoidal variations, indicated by the depicted circles. The resulting response, depicted in Figure 2.21c, is not shaped like a circle, hence, higher order phase terms ($N > 1$) are needed for an accurate model. Figure 2.21d shows the magnitude of the coefficients $R_{2,1,n}$. As expected, the linear terms ($n = 0$ and $n = 1$) are the most significant ones. The next significant term is for $n = -1$, which is the phase-conjugate term. The need for this term is already shown in Section 2.4.4. This spectrum also shows that a relatively low number of complexity N, i.e., between 5 and 7, is sufficient to achieve high accuracy. This allows to get an equivalent behavioral model, allowing to compress the measurement data significantly [65]. If the complexity is reduced to $N = 3$ and four R coefficients, the result is identical to the X-parameters. For $N = 3$ and three coefficients the formulation is equal to the PHD approach. For two coefficients and $N = 1$, the results is equal to the S-parameters.

The coefficients $R_{p,k,n}$ describe how changes like the load impedance at the fundamental frequency, leading to an input at $a_{2,1}$, affect the harmonically related frequencies. If the load impedance is changed, e.g., at the harmonics, the model accuracy degrades, because it is not included in the model. To overcome this issue, the model was extended to include mismatch at harmonic terminations [64]. A main goal was to keep the framework as in Equation (2.40), hence, all phase vectors are formed with reference to the phase of the fundamental stimulus at port 1 (P_1). By considering a stimulus at the 2^{nd} harmonic at port 2, i.e., $a_{2,2}$, a coefficient set can be generated as

$$R_{p,k,n} = \sum_r \left[G_{p,k,n,r}\big(|a_{1,1}|, |a_{2,1}|, |a_{2,2}|\big) \left(\frac{Q_2}{P_1^2}\right)^r \right] \tag{2.41}$$

By substituting Equation (2.41) into Equation (2.40), a more generalized equation can be formed [64]:

$$b_{p,k} = P_1^k \sum_n \sum_r \left[G_{p,k,n,r}\big(|a_{1,1}|, |a_{2,1}|\big) \left(\frac{Q_1}{P_1}\right)^n \left(\frac{Q_2}{P_1^2}\right)^r \right] \tag{2.42}$$

This again consists of various sets of Fourier series, with the coefficients $G_{p,k,n,r}$. The complexity is here denoted by n and r, p denotes the port index and k the harmonic index. This can be rewritten to [65]:

$$b_{p,k} = P_1^k \sum_{n_1=\frac{-N_1-1}{2}}^{n_1=\frac{N_1+1}{2}} \cdots \sum_{n_r=\frac{-N_r-1}{2}}^{n_r=\frac{N_r+1}{2}} \left[G_{p,k,n_1,\cdots n_r} \left(\frac{Q_1}{P_1}\right)^{n_1} \cdots \left(\frac{Q_r}{P_1^r}\right)^{n_r} \right], \tag{2.43}$$

where r denotes the considered input tones. This formulation leads to a comprehensive model for a DUT, but also to a large number of coefficients (the maximum number of coefficients is given by $pk(N+1)^k$).

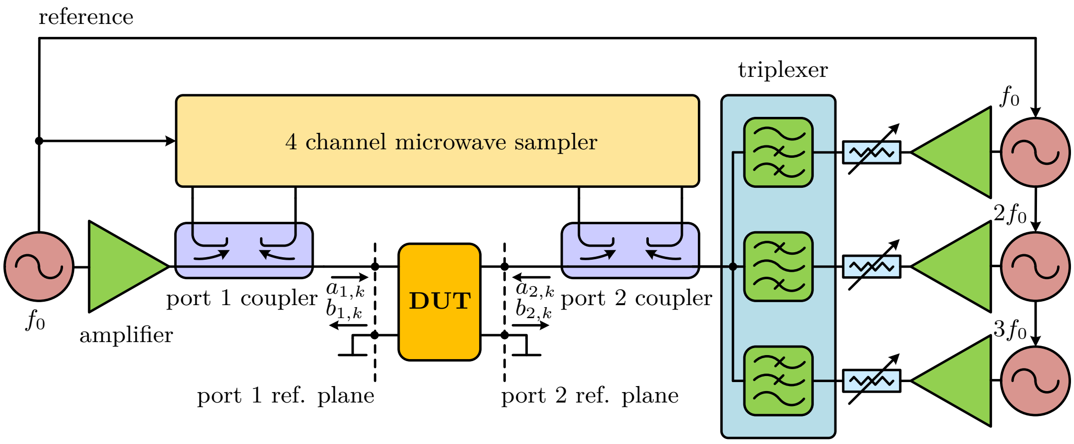

Figure 2.22: Cardiff model measurement setup using open-loop active load-pull [66].

The measurement setup for generating the Cardiff model is based on a load-pull setup. Similar to the VIOMAP, a VNNA is necessary to record the full harmonic response. At Cardiff university, a measurement setup tailored for the extraction of the Cardiff model was developed, which utilizes an open-loop active load-pull setup [66]. As a VNNA, a 4 channel harmonic sampler is utilized in order to measure the fundamental components and the corresponding harmonics, Figure 2.22 shows the block diagram. When using this setup, it is easy to realize the desired stimulus for the model extraction. While applying a constant input stimulus at port 1, an additional input wave with constant magnitude at port 2 is applied, e.g., constant circles with the magnitude of $|a_{2,1}|$, as shown in Figure 2.21b. By varying the phase from 0 to 2π, the Fourier transform can be applied due to the periodic phase. This procedure is repeated for different magnitudes and harmonics, depending on the model requirements [64].

The Cardiff model allows for an accurate description of non-linear RF devices. However, there are some drawbacks: As can be seen in Equation (2.43), the generalized model is cumbersome due to the large number of coefficients. The model coefficients are defined for different magnitudes of the input tones measured in the load-pull measurements. As a consequence, determining the model response for a load condition different from the extraction requires interpolation techniques. Therefore, the model accuracy also depends on the implementation in the simulator. Additionally, performing extrapolation of the DUT's behavior is not possible. Hence, in many cases, a simpler behavioral model is desired.

2.5 Summary

An exact description of non-linear behavior is typically not possible. Therefore, models are needed, which approximate the non-linear behavior accurately for a certain application and DUT. For the use in RF engineering, many different models have been proposed over time, which can be split into three categories: Physics-based models, equivalent circuit models, and behavioral models.

Physics based and equivalent circuit models approximate the behavior of the DUT based on the inner device composition. While physics based models rely on the microscopic building blocks of the DUT, are equivalent circuit models derived by using electrical circuit elements. Consequently, each of these models are especially tailored to fit a certain DUT and do not offer generality.

Behavioral models are based on a different approach: They consider the DUT as a black-box and form a mathematical mapping based on observed input and output quantities gained from the DUT. This can be done by utilizing time-domain or frequency-domain data. Prominent time-domain behavioral models are the Volterra series or ANNs. However, they are not very well suited for RF circuit design and are often hard to extract.

Due to the predominately frequency-domain measurement equipment in RF, frequency-domain black-box behavioral models are desired. Therefore, it is possible to transform the Volterra series to the frequency domain. In combination with traveling waves as input and output quantities, the VIOMAP can be formed. This works well for weakly non-linear DUTs, but similar to the time-domain Volterra series, the extraction is tricky for hard non-linearities. Based on S-parameters, hot S-parameters emerged. These allow to be able to model non-linearities, but only for the fundamental frequency. To overcome this issue the PHD modeling approach was proposed. This relies on describing functions, which are linearized. Consequently, a compact model can be found, which allows to predict the non-linear response of a DUT at the fundamental frequency as well as at the harmonics. The Cardiff model offers a similar approach while approximating describing function based on its periodic phase. This leads to an accurate model, but often to a large number of coefficients.

PHD modeling based models are widely used in practice. Especially X-parameters are well-accepted due to their comprehensive approach including an off-the-shelf measurement solution. They rely on PHD modeling and provide an out-of-the-box measurement solution. They are well-suited for RF circuit design and therefore, serve as a basis for this work. However, they suffer from the same limitations as all PHD modeling based models. A detailed discussion of X-parameters can be found in Chapter 3.

Chapter 3

X-parameters

X-parameters are a registered trademark of *Agilent Technologies*, which is now *Keysight Technologies* and were developed as a measurement-based black-box behavioral model for non-linear DUTs. They are closely related to PHD modeling, introduced in Section 2.4.4 and serve as a superset to S-parameters [67]. The main benefit of X-parameters is that they not just serve as a behavioral model, but that also a comprehensive measurement framework is available. This includes the measurement hardware, the calibration procedure, and the model extraction, which is implemented in the *PNA-X* network analyzer by *Keysight*. Consequently, models can be generated with off-the-shelf hardware, as it is usual for S-parameters. In the following sections, the theory behind X-parameters, as well as the measurement based model extraction procedure, is discussed.

3.1 Definition

Finding an accurate model for a non-linear DUT is tricky. Especially, when it comes to measurement-based black-box behavioral models, it is hard to model the entire range of operation accordingly. As a consequence, several assumptions were made for the X-parameter approach. As a starting point, as for PHD modeling, X-parameters utilize describing functions F_{pk} as a basis, i.e., the outgoing wave can be described as

$$b_{pk} = F_{pk}(a_{11}, a_{12}, \cdots, a_{21}, a_{22}, \cdots, a_{ql}, \cdots), \tag{3.1}$$

with

p . . . output port index

k . . . output frequency index

q ... input port index

l ... input frequency index.

In many cases, e.g., PAs, the DUT operates in a matched environment and is excited with a narrow-band stimulus. This limits the number of possible input signals dramatically, therefore, for typical RF applications, a single CW large-signal stimulus at port 1 is sufficient to formulate a suited model.

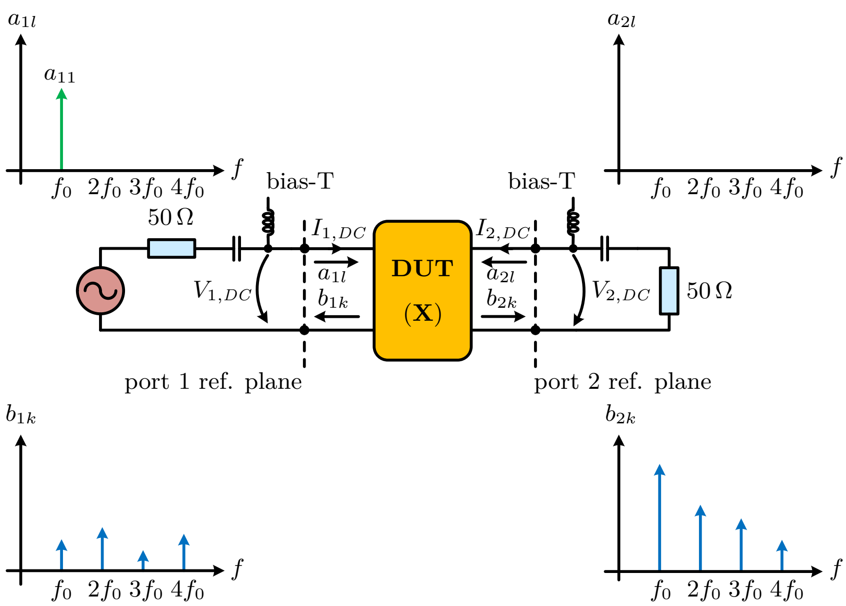

Figure 3.1: Non-linear mapping of X-parameters.

Typical non-linear DUTs are active devices, hence, biasing plays an important role. One can easily imagine that adjusting the gate bias current of an RF power transistor will dramatically change the mode of operation. However, the bias condition can be considered fixed for most applications. For X-parameters these assumptions lead to a formulation of a model defined only on a certain large-signal operating point (LSOP). This LSOP includes all necessary DC bias, as well as the large-signal stimulus at port 1, i.e. $|a_{11}|$. Compared to Figure 2.17, a simplified non-linear mapping can be observed, with a single CW input signal, see Figure 3.1. This means, that the describing function can now be written as

$$b_{pk} = F_{pk}(|a_{11}|) \cdot P^k, \tag{3.2}$$

with P is the large-signal phasor as $P = e^{j\angle a_{11}}$. While this describes the response of the DUT for the assumed load and stimulus perfectly, it is not very useful from a modeling perspective, due to the lack of extrapolation. Hence, similar to the

PHD modeling approach, linearization of the describing functions around the LSOP can be performed. This allows to model perturbations around the LSOP by exploiting the harmonic superposition principle introduced in Section 2.4.4. This leads to X-parameters, which are mathematically defined as

$$\begin{aligned} b_{pk} = {} & X^F_{pk}(|a_{11}|)P^k \\ & + \sum_{(q,l)\neq(1,1)} X^S_{pk,ql}(|a_{11}|)P^{k-l} \cdot a_{ql} \\ & + \sum_{(q,l)\neq(1,1)} X^T_{pk,ql}(|a_{11}|)P^{k+l} \cdot a^*_{ql}. \end{aligned} \tag{3.3}$$

In the formulation, three different parameters, i.e., X^F, X^S, and X^T, are used. While X^F is identical with the describing function in Equation (3.2), the parameters X^S and X^T can be expressed as

$$X^S_{pk,ql} = \left.\frac{\partial F_{pk}}{\partial(a_{ql}P^{-l})}\right|_{|a_{11}|} = \left.\frac{\partial F_{pk}}{\partial a_{ql}}\right|_{|a_{11}|} \cdot P^l \tag{3.4a}$$

$$X^T_{pk,ql} = \left.\frac{\partial F_{pk}}{\partial(a_{ql}P^{-l})^*}\right|_{|a_{11}|} = \left.\frac{\partial F_{pk}}{\partial a^*_{ql}}\right|_{|a_{11}|} \cdot P^{-l} \tag{3.4b}$$

and are called spectral mapping or linearization parameters. These are able to describe perturbations around the LSOP according to the harmonic superposition principle. Mathematically, X-parameters can be seen as a reformulation of PHD modeling. The main benefit of this approach in terms of modeling is, that a mismatch to the LSOP can be modeled, without the use of interpolation techniques. Consequently, the model response of a mismatch is not dependent on the implementation of the model in the simulator. However, this is only possible for a load mismatch. For other LSOP variations, e.g., power sweep or change in the bias condition, the model has to be implemented as a LUT, using different LSOP parameters for each model set.

X-parameters are not limited to only model the traveling waves at the ports of the DUT. The framework can be expanded to model the involved DC voltages and currents [6]. Therefore, describing functions are again used as a starting point. This allows to formulate the DC voltage and current at port p as

$$V_{p,DC} = F^V_{pk}(a_{11}, a_{12}, \cdots, a_{21}, a_{22}, \cdots, a_{ql}, \cdots) \tag{3.5a}$$

$$I_{p,DC} = F^I_{pk}(a_{11}, a_{12}, \cdots, a_{21}, a_{22}, \cdots, a_{ql}, \cdots). \tag{3.5b}$$

Note that the describing functions F^V_{pk} and F^I_{pk} also depend on the DC bias. Similar to Equation (3.3), this formulation can be approximated by considering a single large-signal stimulus a_{11} as

$$V_{p,DC} = X_p^V(|a_{11}|) + \sum_{(q,l)\neq(1,1)} \Re\left\{X_{p,ql}^Z(|a_{11}|) \cdot a_{ql}\right\} \tag{3.6a}$$

$$I_{p,DC} = X_p^I(|a_{11}|) + \sum_{(q,l)\neq(1,1)} \Re\left\{X_{p,ql}^Y(|a_{11}|) \cdot a_{ql}\right\}, \tag{3.6b}$$

with

$$X_{p,ql}^Z(|a_{11}|) = 2 \cdot \left.\frac{\partial F_p^V}{\partial a_{ql}}\right|_{|a_{11}|} \tag{3.7a}$$

$$X_{p,ql}^Y(|a_{11}|) = 2 \cdot \left.\frac{\partial F_p^I}{\partial a_{ql}}\right|_{|a_{11}|}. \tag{3.7b}$$

Note that there are no conjugate terms in Equation (3.6), which is different to the X-parameter formulation in Equation (3.3). This is caused by the fact that the DC voltages and currents have to be real-valued quantities, i.e.,

$$\left(\left.\frac{\partial F_p^V}{\partial a_{ql}}\right|_{|a_{11}|} \cdot a_{ql} + \left.\frac{\partial F_p^V}{\partial a_{ql}^*}\right|_{|a_{11}|} \cdot a_{ql}^* \right) \in \mathbb{R}. \tag{3.8}$$

It can be shown that

$$\left.\frac{\partial F_p^V}{\partial a_{ql}}\right|_{|a_{11}|} = \left(\left.\frac{\partial F_p^V}{\partial a_{ql}^*}\right|_{|a_{11}|} \right)^* \tag{3.9}$$

for $a_{ql} \in \mathbb{C}$. Consequently, the relationship in Equation (3.8) causes the factor of two in Equation (3.7) and for real-valued voltages and currents, it leads directly to the model formulation in Equation (3.6).

3.2 Relation to S-parameters

X-parameters serve as a mathematical superset of S-parameters. Consequently, when extracting X-parameters from a linear DUT, S-parameters can directly be found in the parameter set [6].

When considering an active device, the degree of non-linearity depends on the input power level. For example, an RF transistor can be considered linear if operated in the small-signal regime, i.e., the input stimulus $|a_{11}|$ is small. This linear regime implies that no harmonics are generated or

$$\underset{pk,\, k>1}{\forall} X_{pk}^F \simeq 0. \tag{3.10}$$

The conjugate terms model distortion phenomena (see Figure 2.19b), which do not occur in the linear case. Consequently, these terms vanish

$$\underset{pk,ql}{\forall} X^T_{pk,ql} \simeq 0. \tag{3.11}$$

This leads to a largely collapsed parameters set. While S_{22} and S_{12} can directly be observed from the spectral mapping terms, the remaining S-parameters can be derived as

$$\Gamma_{IN} = \frac{X^F_{11}P}{|a_{11}|}, \tag{3.12a}$$

$$G_{21} = \frac{X^F_{21}P}{|a_{11}|}. \tag{3.12b}$$

Γ_{IN} denotes the large-signal input reflection coefficient, which is equal to S_{11} in the linear case, and G_{21} denotes the complex large-signal gain, which is equal to S_{21} in the linear case. Consequently, the full S-parameter matrix for a linear 2 port is given as

$$\begin{bmatrix} S_{11} & S_{12} \\ S_{21} & S_{22} \end{bmatrix} = \begin{bmatrix} \Gamma_{IN} & X^S_{11,21} \\ G_{21} & X^S_{21,21} \end{bmatrix}. \tag{3.13}$$

In Figure 3.2 the relationship between X- and S-parameters is analyzed for models gained from a commercially available GaN HEMT. There, measured S_{21} and S_{22} values gained at $-10\,\mathrm{dBm}$ input power are compared with the large-signal gain and $X^S_{21,21}$, respectively. Furthermore, a plot of $X^T_{21,21}$ is added. For low input power levels, the magnitude and phase of $X^S_{21,21}$ is independent of the input power, as depicted in Figures 3.2a and 3.2b. Hence, the DUT operates in the linear regime. In this region, $X^S_{21,21}$ equals the measured S_{22}, as described in Equation (3.13). Note that the measured S-parameters deviate slightly from the equivalent quantity derived from the X-parameters. This is caused by measurement uncertainties, as a consequence of the relatively low input power levels in the linear regime. For increasing input power levels, the magnitude and phase of $X^S_{21,21}$ diverges from the initial values and S_{22}, i.e. non-linear effects are present. Additionally, the magnitude of $X^T_{21,21}$ gets larger, i.e., the distortion, modeled by the conjugate terms, increases. Similar effects can be observed for the large-signal gain, depicted in Figures 3.2c and 3.2d. For low input power levels G_{21} and S_{21} are equal in magnitude and phase. For increasing input power levels the gain shows a highly non-linear characteristic, which is typical for such a device and cannot be accurately modeled with S_{21}.

In this example, the relationship between S- and X-parameters is demonstrated. It can be seen that Equation (3.13) holds for a non-linear DUT in the small-signal regime and how X-parameters serve as a superset of S-parameters.

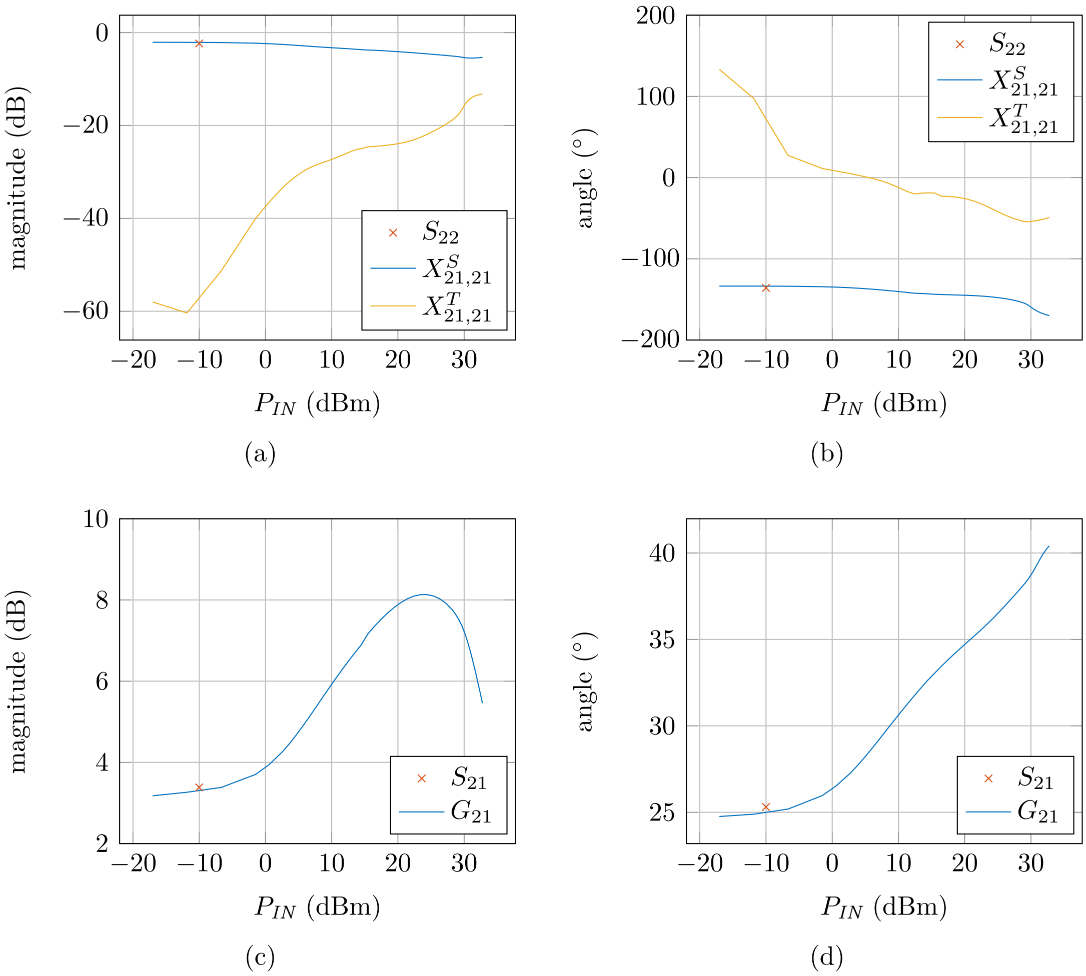

Figure 3.2: Comparison of S_{21} and S_{22} with the corresponding X-parameter quantities, for different input power levels.

3.3 Load-dependent X-parameters

Using X-parameters for modeling non-linear DUTs enables accurate models which can be directly measured with an off-the-shelf measurement equipment. They can handle devices even in a hard non-linear regime, e.g. PAs. Due to the usage of PHD modeling, it is easily possible to use multiple concatenated X-parameter model blocks, which, for example, enables to calculate the non-linear response of an amplifier chain. An implementation similar to S-parameters is therefore possible. However, this is not feasible for all kind of devices. Due to the linearization of the PHD modeling approach, this is only accurate for matched or weakly mismatched environments. If a DUT operates in a strongly mismatched environment, it may happen that, due to load reflections, the harmonic superposition principle is violated and the model prediction leads to an error. Especially when trying to use X-parameters for device modeling in RF PA design this may occur, due to the fact that typical RF power transistors often operate on very low impedance values.

To be able to use X-parameters in highly mismatched environments, it is possible to generalize the PHD modeling approach in order to consider multiple input stimuli [68]. Generally, the describing functions approach is able to consider an arbitrary number of input tones, as stated in Equation (2.18). But, as discussed previously, this would lead to an impractical model. For the purpose of device modeling, limiting the input stimulus to two tones is sufficient in many cases, the large-signal input a_{11} and a second tone a_{21}, which originates from a load mismatch at the output at the fundamental frequency, as shown in Figure 3.3. Consequently, the describing functions can be reformulated as

$$b_{pk} = F_{pk}\Big(|a_{11}|, a_{21}\Big)P^k. \tag{3.14}$$

Note that for ensuring a stimulus only at the fundamental frequency at port 2, an impedance match has to be satisfied for all harmonic loads. With this theory, X-parameters can easily be generated for non-linear devices with more than two ports, e.g. mixers [69].

Similar to X-parameters, Equation (3.14) is desired to be simplified. However, using the traveling wave a_{21} as a variable is unfavorable, since its value is often not known or not meaningful. Thus, analog to load-pull measurements, the fundamental load reflection coefficient at port 2, i.e., the model definition load $\Gamma_{L,M}$, is utilized [70]. Hence, the traveling wave a_{21} can be described as

$$a_{21} = b_{21} \cdot \Gamma_{L,M} \tag{3.15}$$

Consequently, the so-called load-dependent X-parameters can be formulated as

$$\begin{aligned} b_{pk} = {} & X^F_{pk}(|a_{11}|, \Gamma_{L,M})P^k \\ & + \sum_{(q,l)\neq(1,1)} X^S_{pk,ql}(|a_{11}|, \Gamma_{L,M})P^{k-l} \cdot a_{ql} \\ & + \sum_{(q,l)\neq(1,1)} X^T_{pk,ql}(|a_{11}|, \Gamma_{L,M})P^{k+l} \cdot a^*_{ql}. \end{aligned} \tag{3.16}$$

With this extension to the original formulation of X-parameters, it is possible to increase their applicability for device modeling [71]. Even for strongly mismatched devices, an appropriate set of parameters can be found in order to serve as an accurate model. However, prior knowledge of the behavior of the DUT is necessary for this approach, in order to utilize a suited model load condition

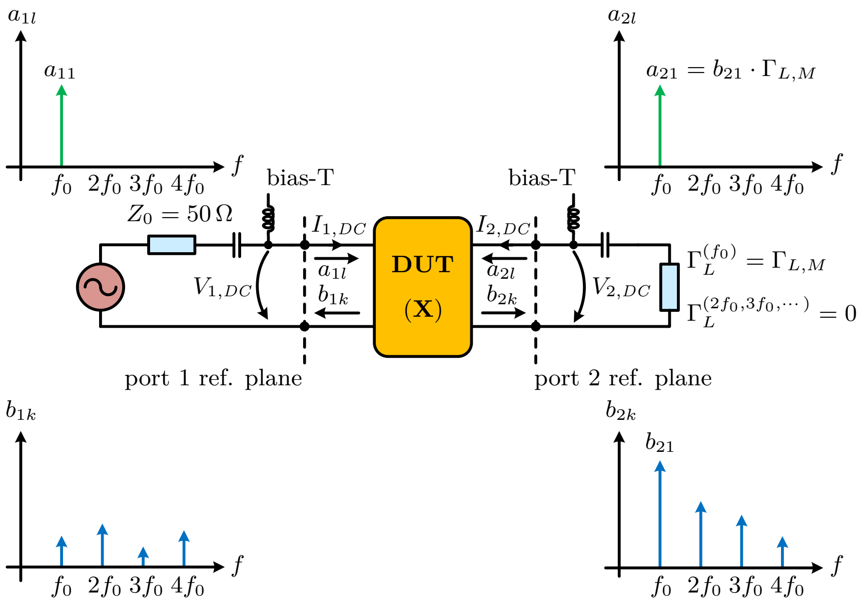

Figure 3.3: Non-linear mapping for load-dependent X-parameters.

$\Gamma_{L,M}$. Also, a more complex measurement setup is necessary because load-pull techniques are utilized. More details regarding the measurement setup are discussed in Chapter 4.

For devices which are very sensitive to an output mismatch, e.g., a typical RF power transistor, another drawback of this approach arises. Due to the linearization of PHD modeling, high accuracy is only given for small perturbations around the model load condition $\Gamma_{L,M}$ due to the harmonic superposition principle, limiting their applicability. To derive a general model with high accuracy, without any knowledge of the behavior of the DUT, it is possible utilize load-dependent X-parameters similar to a LUT. Therefore, N different load conditions $\Gamma_{L,M}^{(n)}$, with $n = 1, 2, \ldots, N$, i.e., a load-pull grid, are used to extract parameters sets. For each load condition $\Gamma_{L,M}^{(n)}$, an independent set of X-parameters is defined. An important parameter is the grid density, which has to be chosen according to the DUT and desired model accuracy. An optimum spacing is always a trade-off between accuracy and model size. An example of a densely-space load-pull grid is depicted in Figure 3.4. Finding an accurate model is possible for any device, but due to the LUT approach, interpolation techniques are required. Furthermore, the model size will increase rapidly by using a high number N of different model definition loads.

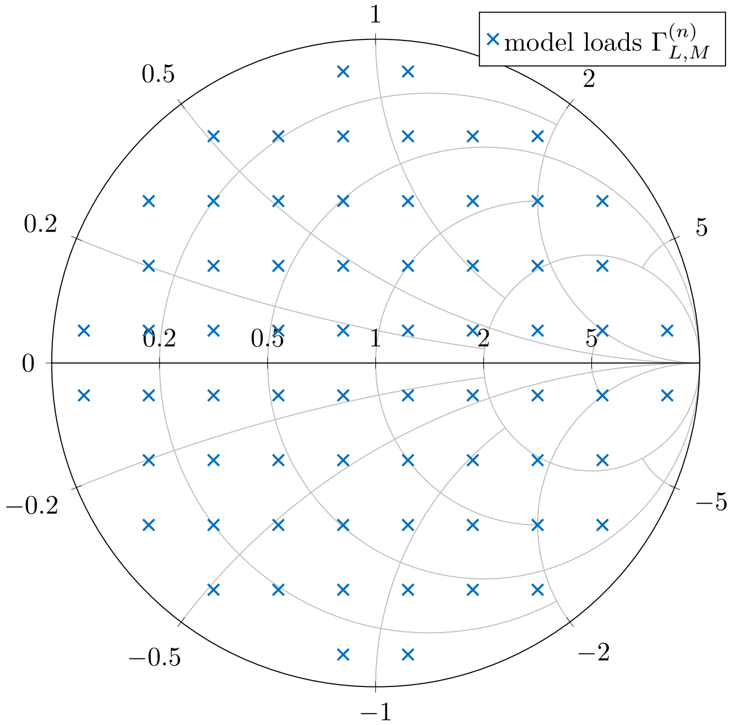

Figure 3.4: Densely spaced load-pull grid for utilizing a wide tuning range.

To get the interpolated response of a set of load-dependent X-parameters, there are several techniques possible. One is to use a commercially available simulation software such as *Keysight Advanced Design System (ADS)* or *NI AWR Microwave Office*. However, it is also possible to utilize the spectral mapping terms of the X-parameter model itself [72]. When predicting the response of X-parameters for a certain load condition $\Gamma_L \notin \{\Gamma_{L,M}^{(n)}\}$, the multiple X-parameter sets lead to ambiguous results for the response. This is because for each set of parameters, which are defined for a different model definition load $\Gamma_{L,M}^{(n)}$, a reflected wave b_{pk} can be calculated. These multiple results for b_{pk} will produce an ambiguous model prediction. To overcome this issue, one could use the trivial solution, i.e., using the result which originates from the closest model definition load by the euclidean distance, or the nearest neighbor. This causes that all other parameter sets are neglected in this case, hence, only one set is remaining, as depicted in Figure 3.5. This may lead to a sub-optimum model prediction. Therefore, using interpolation techniques offers more accuracy. By carrying out the model prediction of an arbitrary number of neighboring parameter sets with different model definition loads, a compound solution can be calculated. In practice, a summation of the responses, weighted by their normalized euclidean distances,

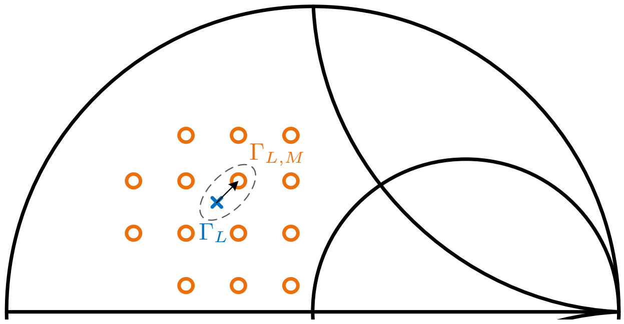

Figure 3.5: Nearest neighbor model prediction.

is determined. This is called the weighted superposition result. In Figure 3.6, this principle is depicted, using four neighboring load conditions. Depending on how many parameters sets are used for calculating the weighted superposition result, the model prediction leads to a more robust solution, because a higher number of parameters sets are used.

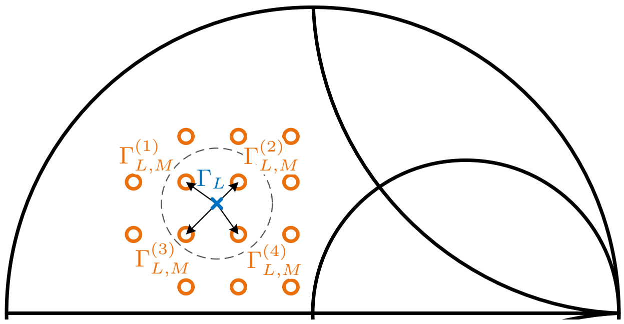

Figure 3.6: Weighted superposition interpolation for four model loads.

Choosing an appropriate strategy for getting an accurate model response strongly depends on the DUT. Figure 3.7 illustrates different evaluations of the model response, demonstrated on load-dependent X-parameters of a commercially available GaN HEMT. The model load conditions $\Gamma^{(n)}_{L,M}$ were chosen to be on a circle with a constant voltage standing wave ratio (VSWR) of VSWR = 8, with a sparse load spacing of 20 °. This is because the difference between the model implementations can be spotted best for these load conditions for this particular DUT. For comparison, verification measurements were performed utilizing loads with the same VSWR, but a much denser spacing of 2 °, see Figure 3.7a. The other graphs in Figure 3.7 show the waves b_{21}, comparing the model prediction results of different model implementations to the verification measurement. It can be seen that for this specific DUT the response strongly depends on the load, as the trajectory of b_{21} changes rapidly for varying loads between $\Gamma_{L,M}^{(1)}$ and $\Gamma_{L,M}^{(4)}$. Therefore, in this region the DUT is very load-sensitive. For all other load conditions considered, the change is small, comparatively.

In Figure 3.7b, the nearest neighbor approach is shown, clearly indicating the accuracy limits of the method. When looking at $\Gamma_{L,M}^{(3)}$, the model prediction looks like a tangent to the trajectory of the verification measurement. It is not exactly linear because of the conjugate terms X^T. Furthermore, strong discontinuities are present, due to different nearest-neighbor X-parameter sets. The response of the weighted superposition for the two nearest neighbors is depicted in Figure 3.7c. It can be seen that especially in the load-sensitive regions, the prediction accuracy is slightly better compared to the nearest neighbor, due to interpolation.

Figure 3.7d shows the prediction response of the implementation in a commercially available simulation environment, in this case *NI AWR Microwave Office 14*. It shows the most accurate implementation, unfortunately the utilized interpolation technique is not known to the author. Due to the observed results, most likely a spline based interpolation is implemented.

It can be seen in this example, that the accuracy of LUT based load-dependent X-parameters are strongly dependent on their implementation in the simulator. Hence, achieving comparable results is hard, especially for a highly load-sensitive DUT. When using a significantly more dense load spacing, all implementations lead to good results, even the trivial nearest neighbor approach. This is especially true for load conditions for which the DUT is insensitive to a load variation. However, a dense load spacing may results in a very large model size and a large measurement time. Furthermore, it can be observed that the spacing of the model load conditions makes a big difference. Therefore, prior knowledge of the behavior of the DUT is indispensable for limiting the model size. Consequently, an optimum load spacing can only be identified by trial and error.

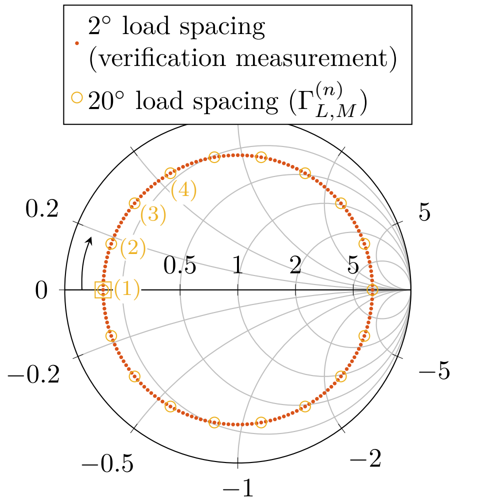

(a) Model extraction loads ($\Gamma_{L,M}^{(n)}$) and verification measurement loads.

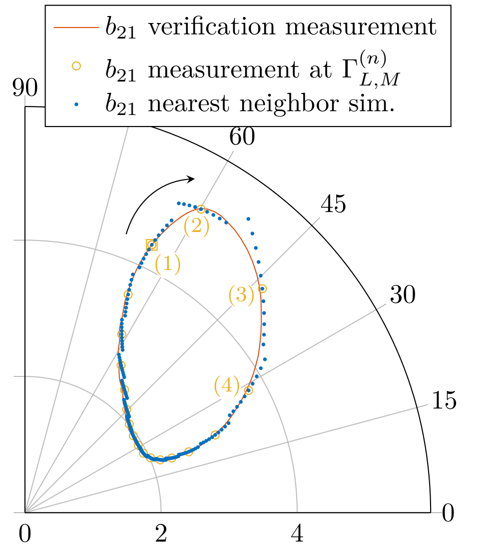

(b) Nearest neighbor interpolation

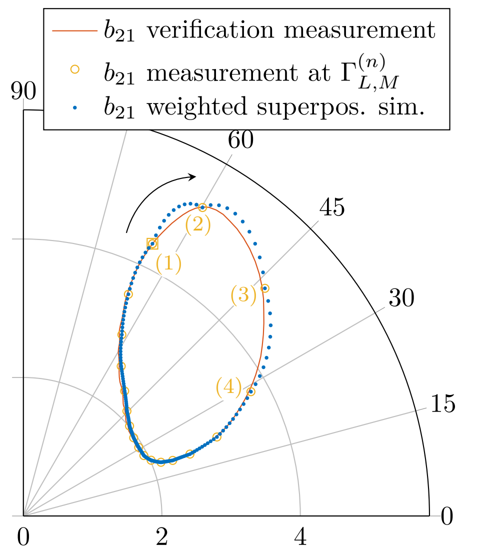

(c) Weighted superposition interpolation with two nearest neighbors

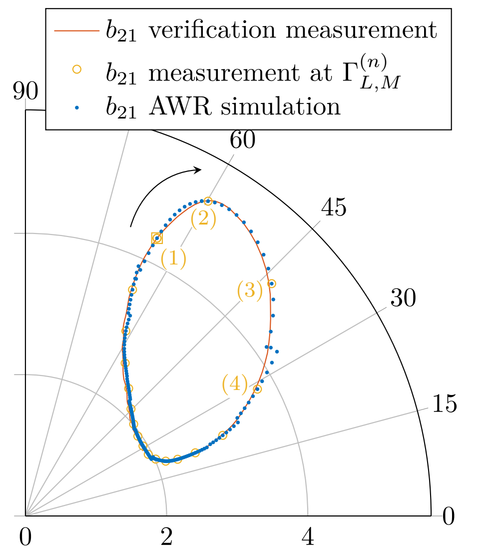

(d) Simulation in *NI AWR Microwave Office 14*

Figure 3.7: Response of load-dependent X-parameters using model loads $\Gamma_{L,M}^{(n)}$ on a circle with VSWR $= 8$ and $20\,^\circ$ load spacing. Different interpolation techniques are compared to a verification measurement.

3.4 Model Extraction

Extracting X-parameters requires certain stimuli conditions. Identifying the nonlinear mapping, or X^F terms, is conceptually the easiest. As already discussed, these parameters are identical to the describing functions with the required stimulus, i.e., a_{11} for X-parameters and a_{11} and a_{21} for the load-dependent case. Therefore, the X^F terms are identical to the large-signal response. Note that a matched source and load is required for the full frequency range including harmonics, except for the fundamental frequency load in load-dependent case. Otherwise additional persistent input signals are present due to reflections, which will cause a systematic error in the X^F parameter.

For identifying the spectral mapping terms, or X^S and X^T parameters, additional small-signal stimulus is necessary. The idea is, that while operating the DUT at the LSOP, i.e., a persistent large-signal stimulus $|a_{11}|$ is applied, a second source is utilized to apply this additional small-signal tone. These are often called extraction tones (ETs) or tickle tones in literature. In order to be able to extract the full set of parameters, this has to be done separately at each involved frequency component, i.e., the fundamental frequency and all considered harmonics, and all ports. Consequently, multiple measurements are necessary in the extraction procedure. To the author's knowledge, two different techniques exist in practice to do so, which are explained in more detail as follows.

3.4.1 Offset Frequency Technique

As the name suggests, for the offset frequency technique this additional small-signal perturbations have a slight frequency offset Δf to the harmonic grid [73]. A plot which shows the principle of the offset frequency technique is depicted in Figure 3.8.

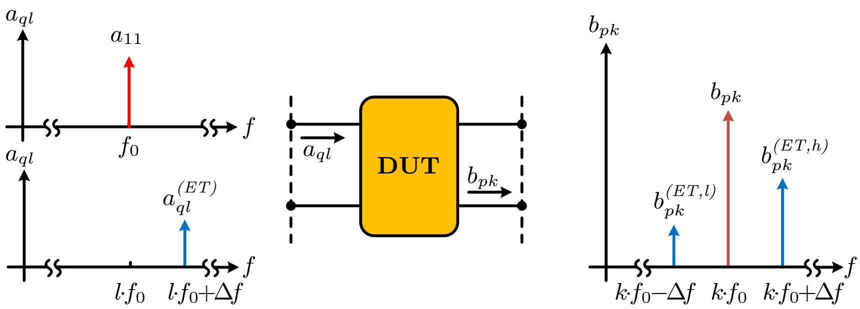

Figure 3.8: Offset frequency technique.

Due to the excitation with the slightly frequency offset ET mixing occurs. Consequently, upper and lower sidebands can be observed at the response. Due to the frequency offset, these can be filtered separately. At all frequencies other than DC, the upper sideband corresponds to the X^S terms and the lower sideband to the X^T terms. They can be calculated as

$$X^S_{pk,ql} = \frac{b^{(ET,h)}_{pk}}{a^{(ET)}_{ql}} \tag{3.17a}$$

$$X^T_{pk,ql} = \frac{b^{(ET,l)}_{pk}}{\left(a^{(ET)}_{ql}\right)^*} \tag{3.17b}$$

The accuracy of the offset phase technique relies on the frequency offset Δf. The highest accuracy is given for $\Delta f \rightarrow 0$. A frequency offset of $\Delta f = 0$ is not feasible, hence, from a measurement point-of-view it should be as small as possible. This strongly depends on the DUT and the measurement equipment. The determination of the optimal frequency offset is always a trade-off, because a very small frequency offset leads to a long measurement time because a low filter bandwidth is necessary and a large frequency offset may cause an error in the model.

3.4.2 Offset Phase Technique

The offset phase technique relies on the phase state of the ET. The ET is always applied at the exact same frequency as the frequencies of the harmonic grid. Consequently, the response of the ET can not be filtered, a separation has to be done in the extraction. The ET also has an influence on both the X^S and X^T terms. Therefore, the response can be seen as a superposition of large-signal and ET, i.e.

$$b^{(ET)}_{pk} = X^F_{pk} + X^S_{pk,ql} \cdot a^{(ET)}_{ql} + X^T_{pk,ql} \cdot \left(a^{(ET)}_{ql}\right)^*. \tag{3.18}$$

As a consequence, multiple measurements are required during the extraction [74]. The principle of the offset phase technique is depicted in Figure 3.9.

Due to the use of multiple measurements, the parameters can be extracted by solving a set of linear equations. This is possible due to the harmonic superposition principle. Since there are three parameters to be estimated, at least three different phase conditions are necessary [75]. By using a larger number N of phase states, an overdetermined set of equations can be formed. This set of linear equations can be formulated as

$$\begin{pmatrix} b^{(ET,1)}_{pk} \\ \vdots \\ b^{(ET,N)}_{pk} \end{pmatrix} = \begin{pmatrix} 1 & a^{(ET,1)}_{ql} & a^{*(ET,1)}_{ql} \\ \vdots & \vdots & \vdots \\ 1 & a^{(ET,N)}_{ql} & a^{*(ET,N)}_{ql} \end{pmatrix} \cdot \begin{pmatrix} X^F_{pk} \\ X^S_{pk,ql} \\ X^T_{pk,ql} \end{pmatrix} \tag{3.19}$$

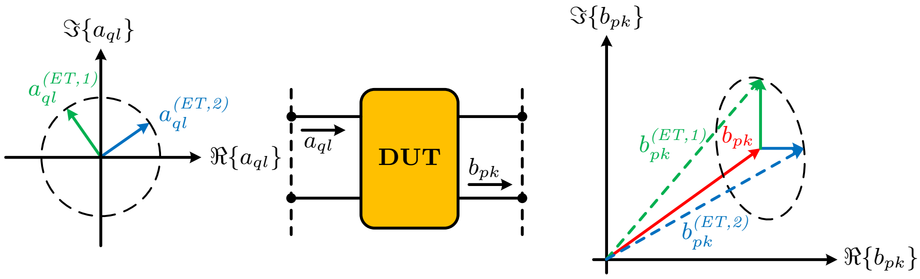

Figure 3.9: Offset frequency technique.

This allows to use least-squares estimation for the parameter extraction, hence, a more robust extraction can be achieved.

Although more ETs are needed compared to the offset frequency technique, this extraction method is easier to implement in a measurement setup, because the ET is on exactly the same frequency than the large-signal stimulus an its harmonics. Furthermore, the possibility of utilizing least-squares estimation makes it the more widely used extraction technique for X-parameter measurements.

An example of an X-parameter measurement using the offset phase technique is shown in Figure 3.10. In this measurement, eight realizations of the extraction tone are utilized in order to be able to form an overdetermined set of equations (Figure 3.10a). In the response of the DUT (see Figure 3.10b), it can be seen that the large-signal response can easily be distinguished from the responses of the ETs. Consequently, it is evident that the harmonic superposition principle is valid. Using this measurement, the corresponding X-parameters can be extracted using Equation (3.19). In many cases least-squares estimation is used, however, any technique which is able to solve an overdetermined set of equation can be used.

3.5 Summary

X-parameters have emerged as a measurement-based black-box behavioral model for non-linear DUTs. They are a superset of S-parameters to handle non-linearities, based on the PHD modeling approach.

Compared to similar models, like the PHD model described in Section 2.4.4 or S-functions, X-parameters come in conjunction with a commercially available off-the-shelf measurement hardware, the *Keysight PNA-X*. Consequently, X-parameters can be generated by the measurement equipment, like it is usual for S-parameters. Therefore, the offset phase technique is utilized. Another benefit is, that they are supported by popular simulation tools like *Keysight ADS* or

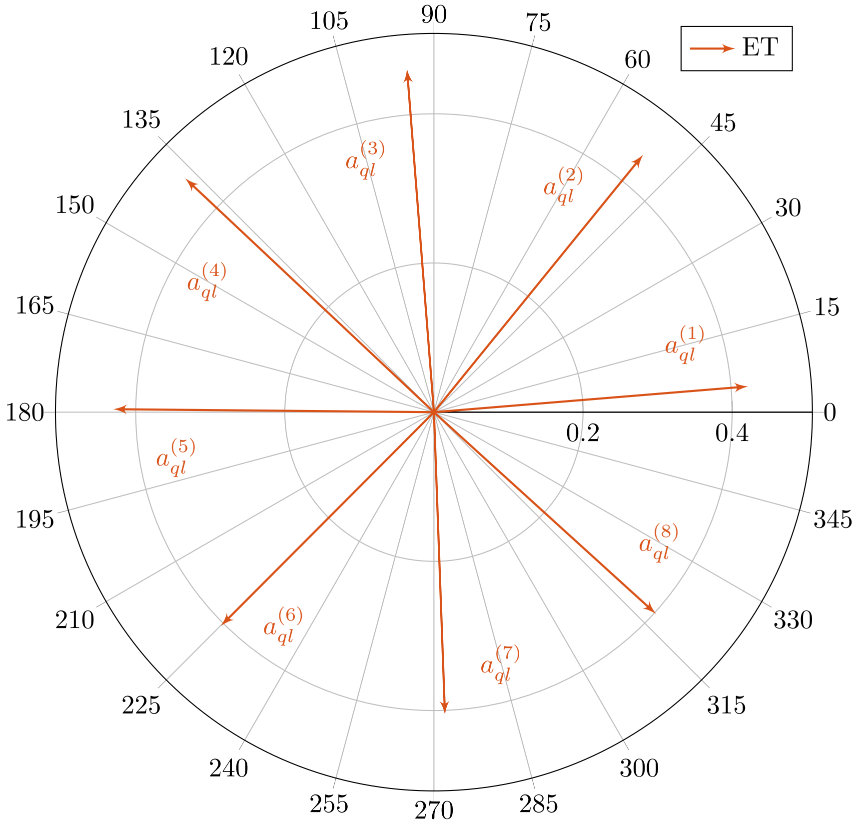

(a) Measured ET

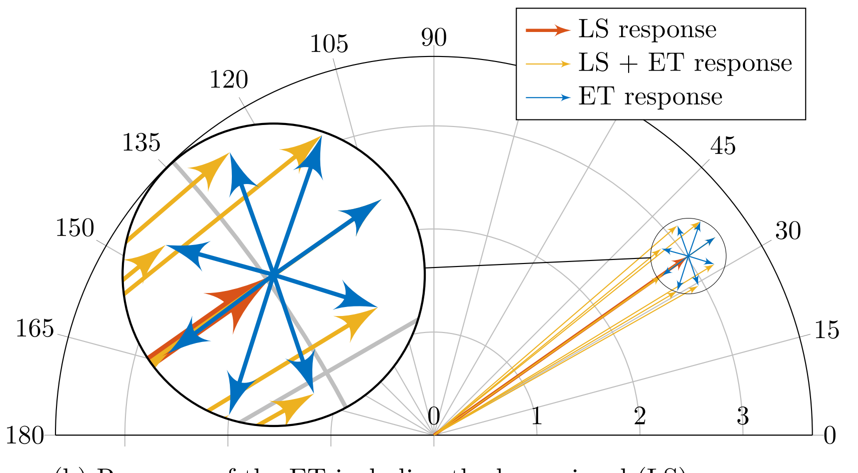

(b) Response of the ET including the large-signal (LS) response.

Figure 3.10: Example of an overdetermined X-parameter measurement using the offset phase technique.

NI AWR Microwave Office.

An extension to the model, the load-dependent X-parameters, allow to define X-parameters for an arbitrary load condition, the model definition load $\Gamma_{L,M}$. This enables a more general use in device modeling, because devices which operate on, e.g., very low impedances, can be modeled easily. However, the model accuracy is limited by the PHD modeling approach, i.e., the linearization of the utilized describing functions. Consequently, for load-sensitive DUTs in strongly non-linear operation, a high model accuracy is typically only given in the proximity of the model definition load. For such devices, multiple model definition loads on a load-pull grid can be utilized to achieve higher accuracy. This means, that the model is implemented as a LUT, hence, interpolation techniques are necessary in the simulator. This may lead to differing results, depending on the implementation in the simulator. Another drawback is that the model size tends to get large, leading to a long measurement duration.

Load-dependent X-parameters can be used as an accurate model for a strongly non-linear DUT, however, there are some difficulties: For finding an appropriate model load condition, either prior knowledge of the DUT is necessary or it has to be determined using trial and error. When utilizing a load-pull grid similar problems arise for defining an appropriate grid spacing. Consequently, it is desired to expand the X-parameter framework in order to be able to get a more general model for handling strongly non-linear and load-sensitive DUTs, which is discussed in the following chapters.

Chapter 4

Measurement Setup

As introduced in Chapter 3, X-parameters rely on a commercially available measurement framework, similar to S-parameters and the VNA. Unfortunately, a VNA is not able to serve as a measurement setup for non-linear DUTs, because it is not able to handle harmonics. However, the concept of the VNA was expanded to fit the requirements of a large-signal excitation. As already mentioned in Chapter 2, the first concepts to do so were called VNNA. These concepts have been developed further, which lead to two different instruments capable of measuring non-linear DUTs, the LSNA and the NVNA [76]. These instruments, their advantages and disadvantages, as well as their applicability for X-parameter measurements are discussed in the following sections.

4.1 Large-signal Network Analyzer

Historically, the first commercially available instrument which was capable of measuring the non-linear response of a DUT, is the LSNA. Over the time a variety of names were used for this instrument, but for simplicity only LSNA will be used in this work.

In principle, the LSNA is a sampler-based instrument. To the author's knowledge, the first approach of this kind was published in 1989 [77]. In this work, the authors used a high speed sampling oscilloscope to record voltage and current waveforms of a non-linear DUT. However, using an oscilloscope is tricky, mainly due to difficulties in the alignment of the channels. The breakthrough came with the introduction of the microwave transition analyzer (MTA) in 1992 by *Hewlett-Packard* [78]. This instrument allows to directly measure amplitude and phase of the travelling waves up to a frequency of 40 GHz. This is done by using harmonic sampling, which is discussed in more detail later on. The first large-signal measurement system utilizing the MTA as a basis was proposed in the same year [79]. The MTA, however, is a 2-channel instrument, which limits its applicability. To fully characterize a 2-port device, two synchronized MTAs can be utilized [80]. This concept was proposed in 1995 and was later called an LSNA. The block diagram of an LSNA is depicted in Figure 4.1.

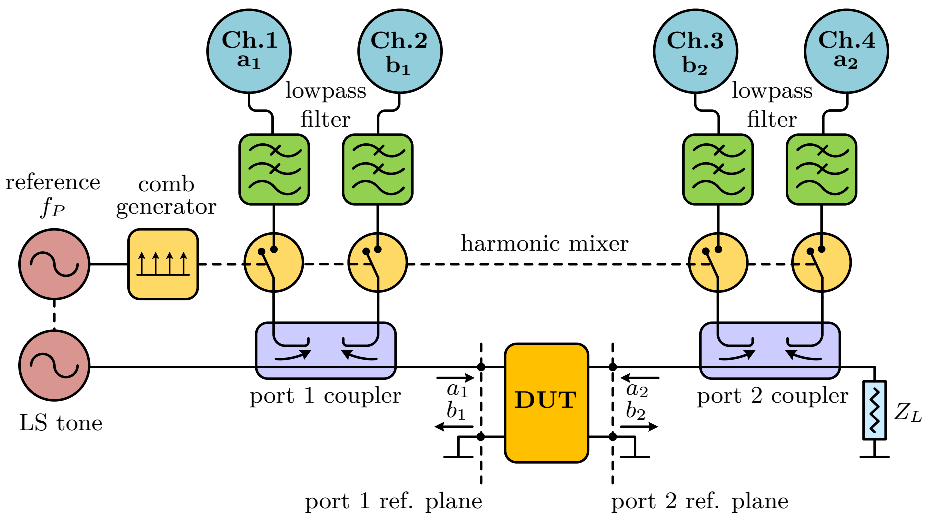

Figure 4.1: Block diagram of an LSNA.

The LSNA is intended to measure the waves a and b for a non-linear 2-port device. Therefore, similar to a VNA, couplers are used. Furthermore, a large-signal source is used for exciting the DUT. The distinct feature of the LSNA is that it uses harmonic sampling or sub-sampling in the utilized MTAs. This allows to record the fundamental frequency and the harmonics of the involved traveling waves [81]. The basic idea of this concept is depicted in Figure 4.2. The block

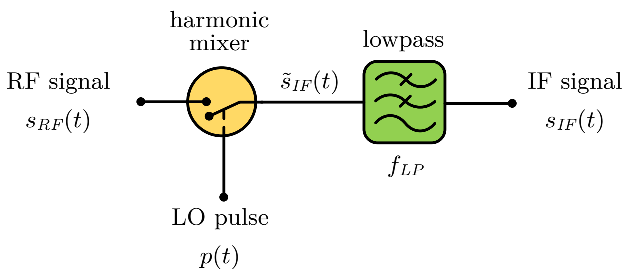

Figure 4.2: Harmonic sampling block diagram.

diagram looks rather simple, it consists of only two elements: A harmonic mixer and a lowpass filter. While the lowpass filter is only required to avoid aliasing, the essential part of this concept it the harmonic mixer.

Harmonic sampling allows to record a signal $s_{RF}(t)$, which consists of a fundamental frequency component as well as harmonics, within a single acquisition and at a relatively low sample rate. Due the presence of harmonics, the bandwidth of the input signal is very high. According to the Nyquist criterion, the sampling rate must be at least twice the frequency of the highest considered harmonic, which is in many RF applications not feasible. However, since the signal $s_{RF}(t)$ is periodic, its spectrum is discrete, allowing to transform its full spectrum into the intermediate frequency (IF) by using a pulse as a local oscillator (LO) source. The IF is in this case an "IF-zone", whose frequency range is restricted by the lowpass filter, which removes all higher order mixing products. Consequently, in harmonic mixing the input signal $s_{RF}(t)$ is multiplied with an LO signal pulse $p(t)$, generated by a comb generator, i.e.,

$$\tilde{s}_{IF}(t) = s_{RF}(t) \cdot p(t). \tag{4.1}$$

After filtering, this results in an IF output signal $s_{IF}(t)$. Ideally, the output of the comb generator is described by a series of Dirac delta functions

$$p(t) = \sum_{n=-\infty}^{\infty} \delta\left(t - \frac{n}{f_P}\right), \tag{4.2}$$

with a pulse repetition frequency of f_P. In frequency domain this translates to a convolution of the input signal with the comb generator output as

$$\tilde{S}_{IF} = S_{RF}(f) * \sum_{n=-\infty}^{\infty} \delta(f - nf_P). \tag{4.3}$$

This is illustrated in Figure 4.3. By a clever choice of the comb generator's pulse repetition frequency f_P, this technique allows to transform an RF input signal and its harmonics to the IF. Therefore, the highest considered harmonic of the input signal has to be within the filter bandwidth f_{LP}. This can be ensured by establishing a comb generator signal component very close but not equal to the fundamental frequency f_0 of the input signal. A different interpretation of this concept is that due to this harmonic sampling, the RF input signal is compressed in the frequency domain. The compression factor is defined as

$$C = \frac{f_0}{\Delta f}, \tag{4.4}$$

with f_0 if the fundamental of the RF input and Δf the distance to the comb generator frequency component $N \cdot f_P$. Hence, at the IF a low frequency replica

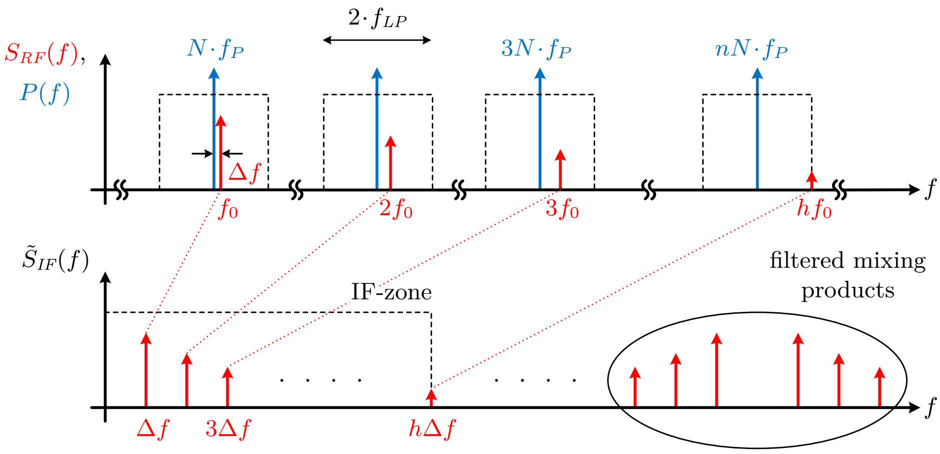

Figure 4.3: Harmonic sampling principle.

of the RF input is observed. Its waveform has an identical shape but at a lower frequency, i.e., a "time-stretched" copy.

Finally, the filtered IF output $s_{IF}(t)$ is digitized with a suitable analog to digital converter (ADC). Is is also possible to use this principle for measuring modulated signals. However, a discrete spectrum of the input signal has to be satisfied, i.e. a periodic input.

The first commercially available LSNA was introduced in 2004 by *NMDG*, the MT4463. It is based on the MTA and is able to characterize a 2-port non-linear DUT up to 50 GHz. Although capable of measuring the full non-linear response, this instrument was discontinued. To the author's knowledge, only one additional LSNA was commercially available, the SWAP X-402 by *VTD* in 2009. This instrument was developed from scratch and is capable to perform a full 2-port characterization up to 30 GHz.

The main benefit of the LSNA is that it is capable of measuring the full non-linear response with a single acquisition, due to the utilization of the harmonic sampling principle. Furthermore, this can be achieved with comparably low sampling rates. The MT4463, for example, has a maximum sampling rate of only 25 MHz. However, compared to a VNA, the achievable signal-to-noise ratio (SNR) is smaller. This is because of convolution of the noise due to the harmonic sampling principle, which reduces the dynamic range of the instrument. Furthermore, it is especially tailored for the measurement of non-linear signals and therefore, further applications for the LSNA are hard to find. To the author's knowledge, this is the main reason why the LSNA has mostly disappeared.

4.2 Non-linear Vector Network Analyzer

Although perfectly suited to measure the non-linear response of a DUT, the LSNA has limitations. Particularly, the dynamic range is the limiting factor. This limitation can be tackled by using mixer based instruments like the VNA. There, the downconversion is based on the heterodyne principle, which allows to achieve high SNR levels and consequently, higher dynamic range. Mixer based VNNAs have been usually called NVNA in literature, hence, it will be used in this work as well.

A VNA is optimized for measuring linear S-parameters, hence, non-liner measurements are not feasible in an out-of-the-box configuration. However, it is possible to measure the harmonics consecutively, by tuning the LO according to the fundamental frequency and the harmonics, respectively. But this is only possible, if the LO and RF sources of the VNA can be tuned independently. This allows to achieve a high dynamic range in the measurement, but a problem arises in the phase relations between the harmonics. This is because of the consecutive measurement of the fundamental frequency and the harmonics, the cross-frequency phase is unknown, consequently, the signal cannot be reconstructed. Hence, a so-called harmonic phase reference (HPR) is needed.

A first measurement solution of this kind was proposed in 1989 [82]. In this work, the harmonics are measured by tuning the receivers sequentially to each of the harmonics at the output. As a large-signal source, a signal generator is used, which is able to provide the required driving power. In order to align the harmonic phases, an additional measurement with a ”golden diode” is performed, which serves as a phase calibration. This golden diode, in this case a Schottky diode, operates as a limiter to provide a well defined spectrum of harmonics, serving as a HPR. This setup allows for an accurate measurement, but only for the output of a DUT. Furthermore, the applicability of the proposed golden diode approach is limited, because the harmonic power content is limited in the proposed limiter configuration. Also long-term stability issues arise in the calibrated phase relations, hence, re-calibration of the phase may be necessary.

Similar to the LSNA, newer concepts of the NVNA utilize comb generators for phase calibration. These are typically based on step-recovery diodes (SRDs), as discussed in more detail in Section 4.3. Additionally, a second comb generator is permanently measured as an HPR signal, to obtain reliable and stable cross-frequency phase relations to reconstruct the measured signal [83]. It is important, that they contain frequency components at least at all considered harmonics, consequently, the comb generator reference frequency is set to $f_P = f_0/n$, with n is an integer number. This ensures, as long as the measurement HPR signal is constant during calibration and measurement, that the phase relations between all harmonics can be determined accurately. To do so, the comb generator used

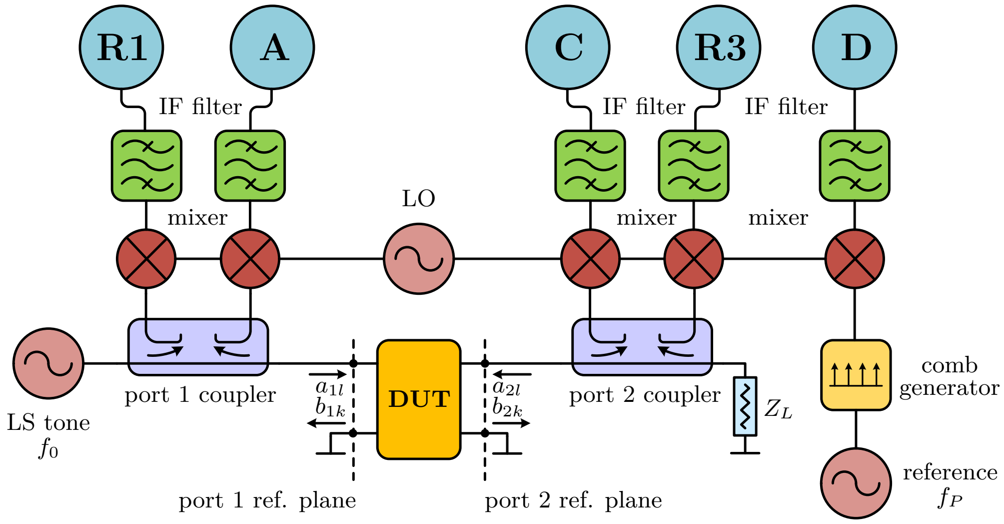

Figure 4.4: Block diagram of an NVNA.

for calibration must be perfectly known, similar to the golden diode. Due to the phase reference signal however, an extra receiver becomes necessary, i.e., for a non-linear 2-port measurement, five receivers are needed [84], see the block diagram in Figure 4.4. Note that the receiver notation introduced in Section 2.4.2 was utilized, i.e., A, C, D, R1, and R3, which is according to *Keysight's* NVNA solution.

With such a setup, a high dynamic range can be achieved in the measurements. However, the drawback is that the harmonic response cannot be measured with a single acquisition, but only consecutively. This leads to a longer measurement time compared to an LSNA.

Currently, the NVNA has established itself as the main instrument for non-linear measurements and several different instruments are available. The most prominent candidate is the *PNA-X* by *Keysight*, which was released in 2008. In the same year, *NMDG* released an NVNA based on the *Rohde & Schwarz ZVxPlus*, the *NM300*. Both instruments are fully capable of measuring the non-linear response of a certain DUT. However, the PNA-X has the benefit of offering the capabilities to generate X-parameters as well, see Figure 4.5. As can be seen in the block diagram, a second coherent signal source is implemented. Consequently, one source, the large-signal source, provides a persistent large-signal stimulus, while the second, the ET source, can be switched to both RF ports. With this configuration, the offset phase technique can be used to extract X-parameters, as introduced in Section 3.4.2. Furthermore, the NVNA is also able to perform S-parameter measurements, by just using the ET source. Hence, in contrast to

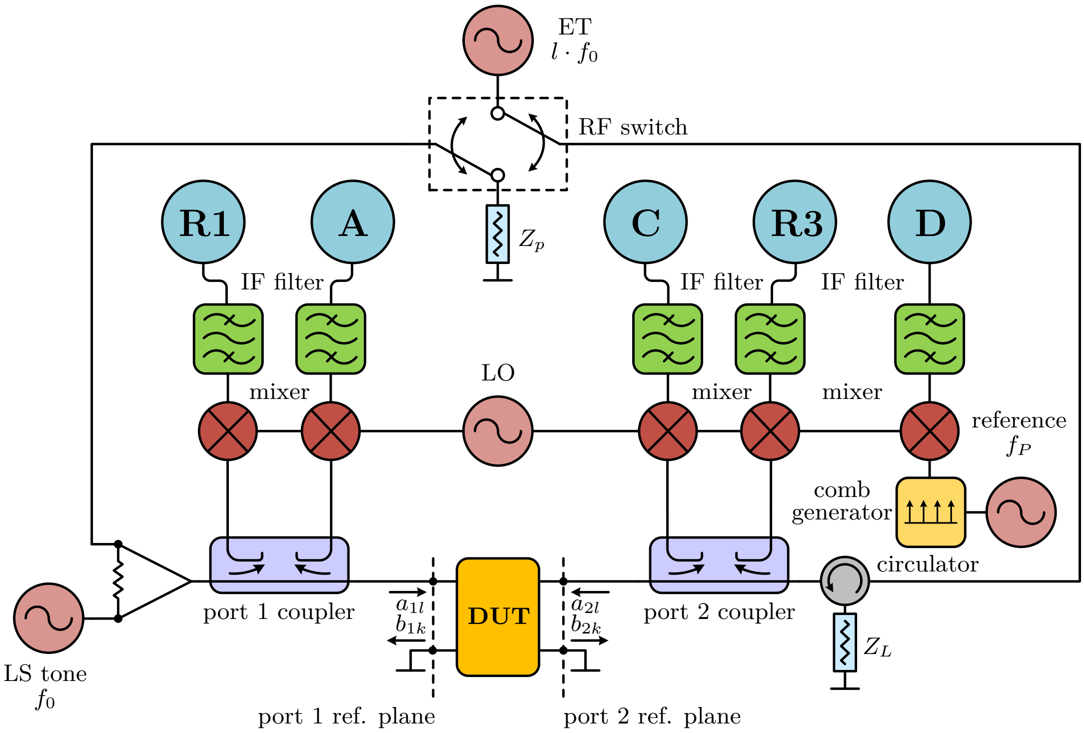

Figure 4.5: Block diagram of an NVNA, capable of extracting X-parameters.

the LSNA, the NVNA is also able to serve as a VNA. To the author's knowledge this is why the NVNA has replaced the LSNA in many RF laboratories.

4.3 Phase Reference

As discussed in the previous sections, a phase reference is indispensable for non-linear measurements. It is utilized for the harmonic mixer in the LSNA, as well as a HPR for the NVNA, necessary to correctly align the harmonics in the measurement. The requirements on the phase reference are sufficient power at the harmonics and a stable phase response. Also, a low pulse repetition frequency (PRF) is often desired, in order to be able to measure at different fundamental frequencies. If this is the case, the PRF is given by the distance of the chosen fundamental frequencies or a fraction of it, to ensure an HPR signal component at each considered frequency point. Ideally, a comb generator, whose output consists of a series of Dirac delta functions, as in Equation (4.2), is used. Comb generators fit these requirements perfectly, but an ideal realization, which shows a series of Dirac delta functions at the output, cannot be realized in practice. However, there are several ways to realize comb generators, capable of serving as a HPR in a non-linear measurement.

For RF frequencies, most common designs for comb generators are based on SRDs [85]. A schematic of the principle is depicted in Figure 4.6. In this circuit,

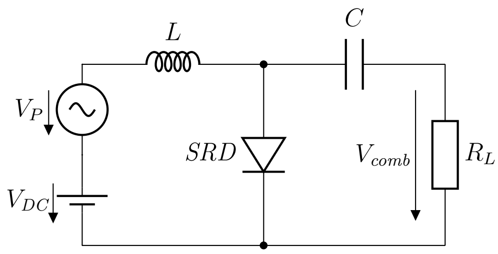

Figure 4.6: Principle of a SRD based comb generator.

the diode operates in two different states because of the alternating current (AC) driving signal, namely in forward and in backward direction. During switching from forward to backward direction, a high amplitude, narrow, and negative pulse is formed, by the energy stored in the driving inductance L. The energy appears across the diode, now in off-state. The diode can now be seen as a capacitance C_R, which determines the width of the pulse as

$$t_P = \frac{\pi\sqrt{LC_R}}{\sqrt{1-\xi^2}}, \tag{4.5}$$

where ξ is the damping factor, which strongly depends on the load. The height of the pulses is proportional to the energy stored in the inductance. By applying a driving signal V_P, a frequency comb is realized. This is a simple method in realizing a comb generator, which is capable to serve as a phase reference in non-linear measurement setups. State-of-the-art phase references however, are utilizing high speed heterojunction bipolar transistors (HBTs) instead of SRDs. These allow to achieve smaller pulse widths t_P, which are independent on the PRF, i.e. the frequency of V_P [86]. One candidate of such a comb generator is the *Keysight U9391F*, which was used for all measurements presented in this work, see Figure 4.7 [87].

To see the performance of the used comb generator, its output was measured using a *LeCroy WaveExpert SDA-100G* sampling oscilloscope. Therefore, is was directly connected to the oscilloscope channel. For the measurement the PRF was set to 500 MHz. The time signal V_{comb} of the measured comb generator, see Figure 4.8, shows, that the pulse width t_P is very small, hence, very close to an ideal series of Dirac delta functions. In Figure 4.9 the frequency domain representation, i.e., the Fourier transform of the measurement in Figure 4.8, is depicted. As expected, due to the small pulse width, a flat magnitude response, as

Figure 4.7: Keysight U9391F comb generator [87].

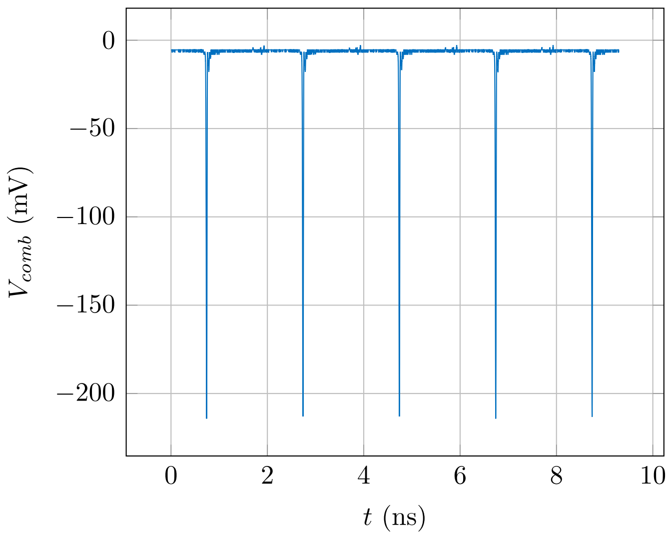

Figure 4.8: Measured time voltage of a Keysight U9391F comb generator with $f_P = 500\,\mathrm{MHz}$.

depicted in Figure 4.9a, and a very flat phase response, depicted in Figure 4.9b, is ensured. This makes it the perfect candidate for a phase reference for non-linear measurements. Note that the phase of the pulse in Figure 4.9b is expected to be exactly at $-180\,°$, which is not the case in the measurement. However, the datasheet of the given comb generator shows a phase tolerance of $\pm 10\,°$, hence, the measurement is well within the tolerance.

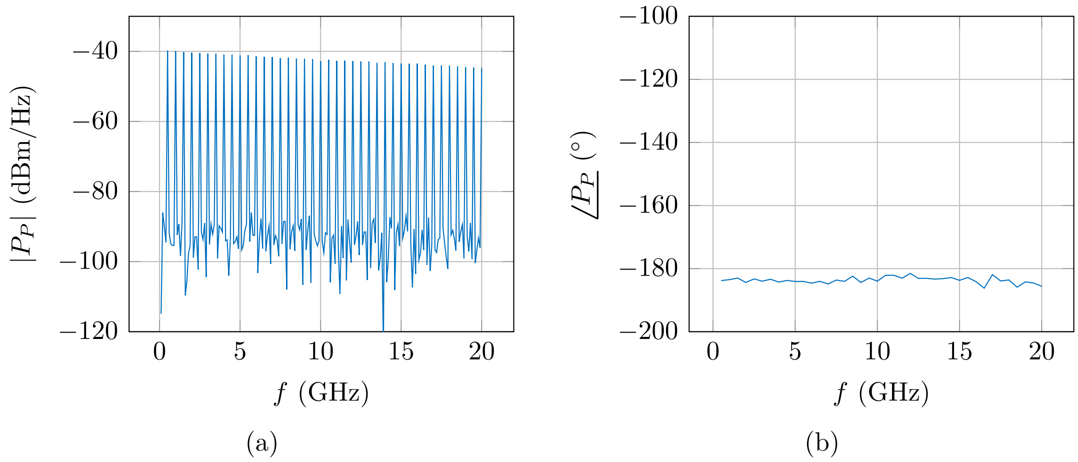

Figure 4.9: Frequency domain representation of the measured Keysight U9391F comb generator with $f_P = 500\,\mathrm{MHz}$.

4.4 Calibration

To perform accurate measurements, calibration is a must. Unlike S-parameter measurements, a vector calibration alone is insufficient for a non-linear measurement setup. To be able to accurately reconstruct the non-linear voltage and current waveforms, additional calibration steps are necessary. Consequently, the calibration has to be split in four different steps:

- 2-port vector calibration
- Receiver power calibration
- Source power calibration
- Phase calibration

For performing a vector calibration, as for S-parameters measurements, different approaches are possible. For example, for coaxial DUT connectors, short, open, load, through (SOLT) or unknown-through calibrations are mostly used in practice [88, 89]. To perform an accurate calibration, an error model is necessary. For the NVNA an 8-term error model is used [84]. The signal flow graph of the 8-term error model is depicted in Figure 4.10. According to this error model, two error-boxes, E1 for port 1 and E2 for port 2, are determined during the calibration procedure. The actual calibration procedure is well known and will not be discussed here in detail. These error-boxes are used to calculate the incident

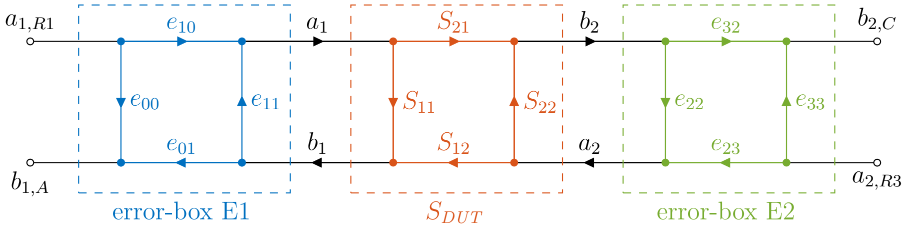

Figure 4.10: 8 term error model used for NVNA calibration.

waves a_1 and a_2, as well as the reflected waves b_1 and b_2, out of the measured quantities at the corresponding receivers $a_{1,R1}$, $a_{2,R3}$, $b_{1,A}$, and $b_{2,C}$, respectively.

The vector calibration is especially tailored for the needs in S-parameter measurements, i.e. rationed measurements. Consequently, absolute quantities for the involved traveling waves a and b are not known, because the receivers are uncalibrated and the power of the signal source is not exactly known. For a non-linear measurement this is not sufficient, it is required to know the absolute quantities for the involved traveling waves. Consequently, a second calibration step is performed, i.e. the receiver power calibration. Therefore, the RF source is turned on and the port power is measured with a power meter and the receivers at all considered frequency points. Consequently, calibration coefficients can be determined in order to get a calibrated power reading at the receivers.

As discussed in Section 4.2, the phase relations between the harmonics are crucial in a non-linear measurement, otherwise restoring a time-domain waveform of the measured signal would be impossible. Consequently, a phase calibration step is indispensable.

The phase calibration is performed similar to the golden diode approach in [82]. However, instead of using a Schottky diode in a limiter configuration, a comb generator is used as a HPR. Its output can be written as

$$b_n^{HPR} = \left| b_n^{HPR} \right| \cdot e^{j(n\omega_0 t + \phi_n)}. \tag{4.6}$$

It is necessary that the coefficients $|b_n|$ and ϕ_n are perfectly known, hence, prior characterization of the HPR is performed [90].

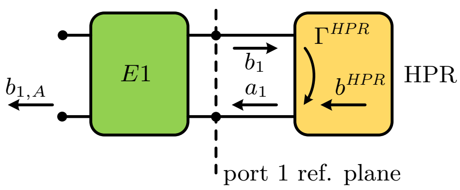

Figure 4.11: Phase calibration.

During calibration, the HPR is connected to the measurement port, hence, port 1 in most cases. A block diagram is depicted in Figure 4.11. Note, that vector calibration is necessary to preform this step, otherwise the coefficients of the phase calibration cannot be determined. Using this configuration, the output of the HPR can be measured using port 1 of the NVNA, which can be written as

$$a_1(n\omega_0) = b_1(n\omega_0) \cdot \Gamma^{HPR}(n\omega_0) + b^{HPR}(n\omega_0). \tag{4.7}$$

By using this procedure, $N + 1$ unknowns are observed, i.e., the N phase terms of the measured signal and the starting time $t + \tau$ of the measurement. However, the phase shift from the measurement ports to the receivers is not time varying. Consequently, the phase of the fundamental frequency must be constant from measurement to measurement. Hence, it is possible to define a calibration reference time in the calibration, allowing to set the phase of the harmonics correctly relative to the fundamental frequency [91].

At last, a source power calibration is performed in order to satisfy a defined port power. Again this is a well-known procedure and therefore, it will not be discussed here in detail.

4.5 Device Under Test

For this work, a commercially available GaN HEMT was chosen as the DUT, because different modes of operation can easily be achieved by varying the bias voltages [5]. For the measurements, the *CHG40010F* by *CREE* was chosen. This transistor has a typical output power of 10 W over a wide frequency range, while maintaining high a gain [92]. Furthermore, an accurate equivalent circuit model is available, which allows to generate models also from simulated data [25].

This transistor is available in packaged configuration only. To make it accessible to a coaxial measurement setup, a test fixture was designed. Therefore, two 50 Ω microstrip transmission lines, with a length of 10 mm each, were designed on a *Rogers RO4003C* substrate. With a thickness of 0.508 mm, a copper cladding of 17 μm, and a dielectric constant of $\epsilon_r = 3.38$, 50 Ω transmission lines with nearly the same width as the leads of the transistor can be achieved [93]. These were used to connect the DUT's package leads with coaxial connectors. Due to their rugged design, low losses, and good reproducibility *Rosenberger 32K243-40ML5* connectors were used. In Figure 4.12 the DUT, the designed printed circuit board (PCB), and the connectors, mounted on a heat sink because of the high power dissipation, are shown.

To remove the influence of the test fixture from the measurements, a through, reflect, line (TRL) calibration was performed [94]. This allows to describe the transition from the coaxial connector, i.e, the coaxial reference plane defined

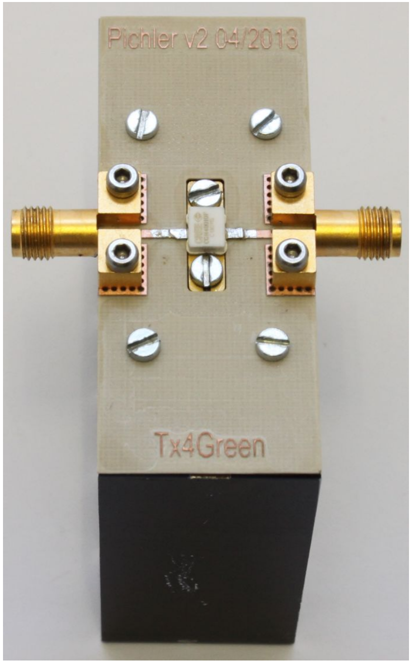

Figure 4.12: *CREE CGH40010F* mounted on a test fixture.

using a SOLT calibration, to the DUT's package leads. This leads to error-boxes describing this transition perfectly. Consequently, all presented measurements are de-embedded using this error-boxes, hence, the measurement reference plane is at the leads of the DUT package, i.e., at the DUT reference plane, as shown in Figure 4.13.

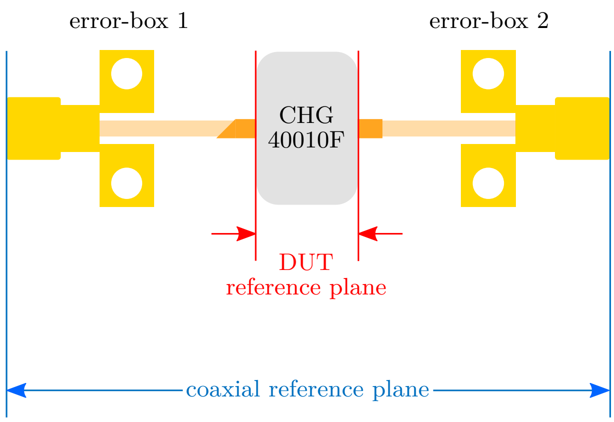

Figure 4.13: Reference planes.

For the measurements in this work, the drain bias voltage is remained constant at 28 V and the drain quiescent current $I_{D,q}$ is varied in order to obtain different modes of operation, which is stated in the presented measurements. The measurements are performed at different fundamental frequencies, all in the range 2 . . . 2.65 GHz, while considering harmonics up to the third order.

4.6 Measurement Setup

For the measurements in this work, an NVNA is used, in particular, the *Keysight N5247A PNA-X*. As discussed in the previous section, the used DUT typically has an output power of 10 W. Consequently, a direct measurement with the given instrument is not possible because the port input power is limited to 27 dBm. However, it is possible to use the NVNA in high power configuration [95]. Therefore, the test-set is expanded with external directional couplers and attenuators. Apart from power handling issues, the attenuators have to be chosen to ensure linear operation of the receivers for all possible input power levels. All external components in the setup are discussed as follows, a block diagram including maximum observed power levels is depicted in Figure 4.14.

For the expanded test-set the most significant limit is the receiver input power, which has a damage level of 15 dBm for all receivers. Furthermore, an operation in the linear region has to be satisfied, which is specified in the range of $-60\ldots-5$ dBm [96]. For higher input power levels the receivers are in compression and for lower levels crosstalk and noise may have significant contributions. This, however, strongly depends on the chosen IF bandwidth and averaging. For an IF bandwidth of 10 Hz, the receiver noise floor is specified at −127 dBm/10 Hz in a frequency range of 1 . . . 10 GHz [97]. Consequently, very low input power levels are possible, however, one should bear in mind that low SNR levels will limit the measurement accuracy.

As a maximum saturated output power of the DUT, 42 dBm is considered for dimensioning the external components. To achieve such high output power levels, sufficient driving power is required. The source power of the NVNA is limited to about 5 . . . 6 dBm, which is far to little considering a small-signal gain of about 16 dB maximum. Consequently, a driving power amplifier is needed. Therefore, a *Mini Circuits ZVE-3W-83+* was chosen, with a maximum output power of 35 dBm and a gain $G = 35$ dB. This allows to provide a sufficiently high driving power for the chosen DUT. This amplifier has a frequency range of 2 . . . 8 GHz, which perfectly fits the desired frequency range.

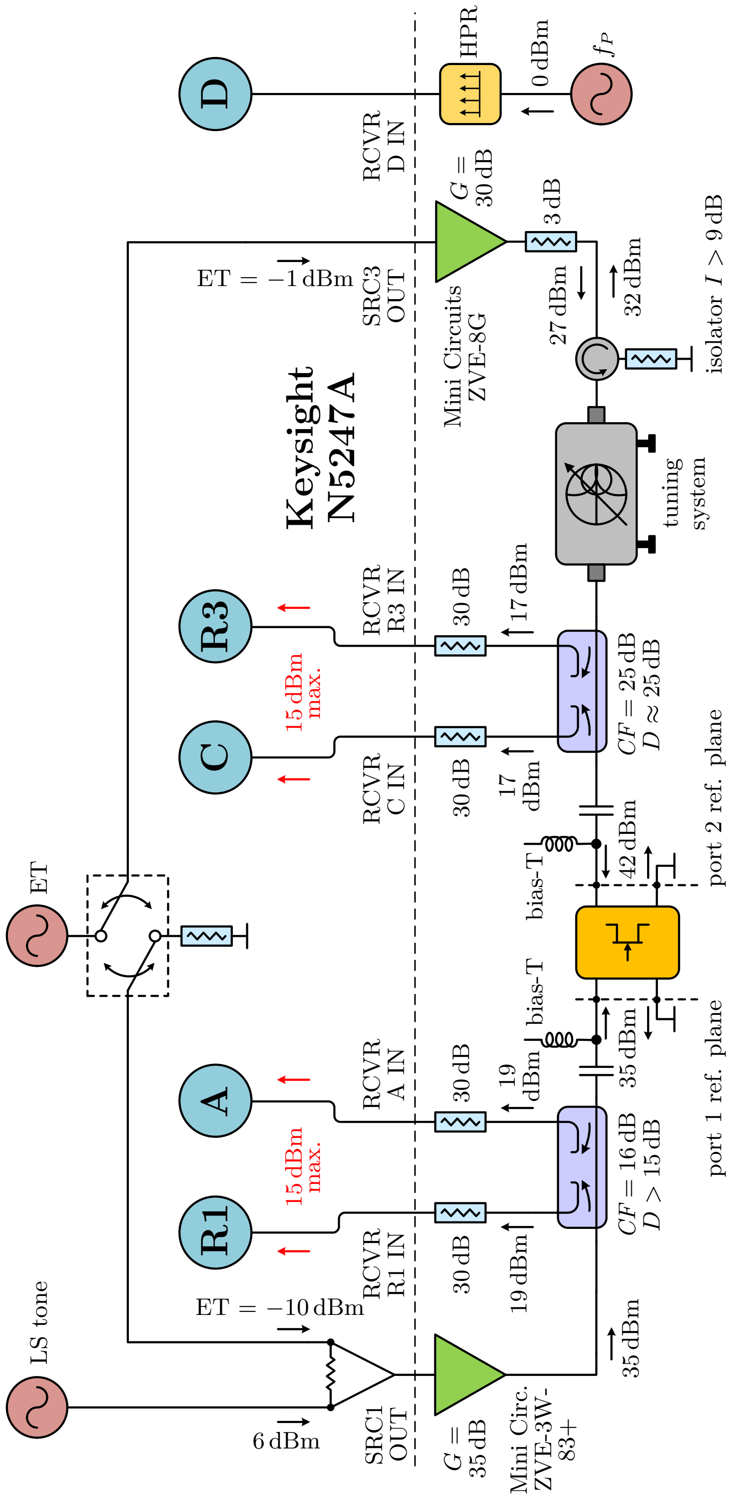

Figure 4.14: Block diagram of the high power measurement setup, including maximum power levels.

For the actual measurement, directional couplers are necessary. For port 1, a *Krytar 1850* is used. This coupler shows a coupling factor $CF = 16\,\mathrm{dB}$ and high directivity $D > 15\,\mathrm{dB}$ over a wide frequency range. For port 2, a *MITEQ CD2-102-802-300N* is used. It has a coupling factor $CF = 25\,\mathrm{dB}$ and a directivity $D \approx 25\,\mathrm{dB}$ in the desired frequency range and is suited for very high input power levels ($P_{MAX} = 500\,\mathrm{W}$). To ensure linear operation, 30 dB attenuators are used at each coupled port. Due to the high dynamic range, phase calibration is still possible at port 1, however a low IF bandwidth and averaging has to be used in order to ensure sufficient SNR.

To be able to measure load-dependent X-parameters, a passive load tuner is placed at the output of the DUT. Depending on the specific measurement task, this tuner is implemented either as a single passive automated slide-screw tuner *Maury MT982A* or multiples of these to form a cascaded or triplexer based harmonic tuning setup, as discussed in Section 2.4.1. For the measurements, the tuners are controlled using the *Maury ATS 5.33* software.

The directional couplers are placed right next to the DUT, to limit the measurement uncertainties. Albeit very small, the insertion loss of the couplers limits the tuning range of the setup: At 2 GHz the maximally achievable VSWR drops from about 12.3 to 9.3 for a single tuner when adding the directional coupler next to the DUT. A placement of the couplers behind the tuners is possible by applying tuner de-embedding, but it was preferred to measure the waves directly without de-embedding the tuners [91]. This reduces measurement uncertainties caused by tuner repeatability and tuning sensitivity errors during tuner de-embedding. This is especially an issue for cascaded tuning setups. Furthermore, very high reflection coefficients are not required for the utilized DUT, hence, the provided tuning range was considered as sufficient.

Providing an ET at both ports is a necessity for extracting X-parameters. Although small-signal, the level of the ET is determined by the DUT. As a rule of thumb, the ET should be at least 16 dB smaller than the large-signal tone [98]. Due to the high output power of the DUT, the ET source cannot be directly connected, otherwise the instrument would be damaged. Consequently, a circulator (*DiTom D3C2080*) was added as an isolator. However, due to the high bandwidth of the isolator, only a minimum of 9 dB of isolation can be guaranteed. To protect the instrument from damage, an additional attenuator could be used, but this would limit the ET power severely. Consequently, an amplifier, a *Mini Circuits ZVE-8G*, in combination with a 3 dB attenuator was used. The attenuator is to protect the output of the amplifier, while the amplifier ensures high isolation to protect the NVNA and allows to provide a sufficiently large ET.

The last remaining elements in the setup are the bias-tees, to apply the DC bias voltages for gate and drain. The measurement phase reference is connected to the NVNA to ensure constant phase relations in the measurements and is driven by an external source, which is synchronized with the NVNA.

The full setup, i.e., the NVNA including all external components, is depicted in Figure 4.15. With this setup, all measurements were gained for this work. Note that in this picture the triplexer based harmonic load-pull setup is shown as tuning system. Alternatively, as discussed previously, a cascaded harmonic tuning setup was used in certain measurements, where only the tuning system is changed while all other components remain equal to the shown picture. The used setup is stated when presenting the respective measurement results.

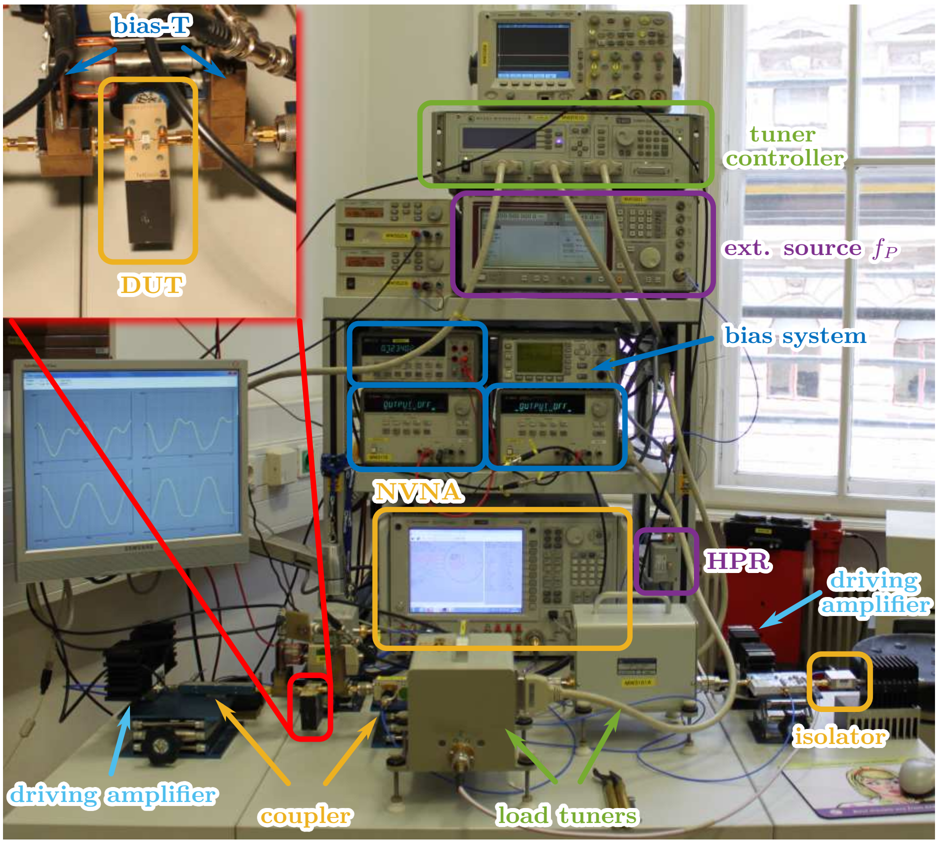

Figure 4.15: Picture of the setup including the NVNA in high power configuration.

4.7 Setup Imperfections

Because of the usage of external components in the test-set, which are required for high power measurements, inherent imperfections are added to the measurement setup. These imperfections are mainly caused by sub-optimum characteristics of the used components. Particularly, a limited return loss of, for example, PAs, directional couplers, or circulators, leads to a poorer RF performance of the NVNA compared to its off-the-shelf configuration. Consequently, the return loss of the measurement ports degrades and causes reflections of the DUT's output signal. This may violate the stringent requirements on the stimulus for X-parameter extraction, because any mismatch at harmonic frequencies will inherently cause an additional persistent large-signal stimulus. This will lead to a systematic error in the extracted parameters.

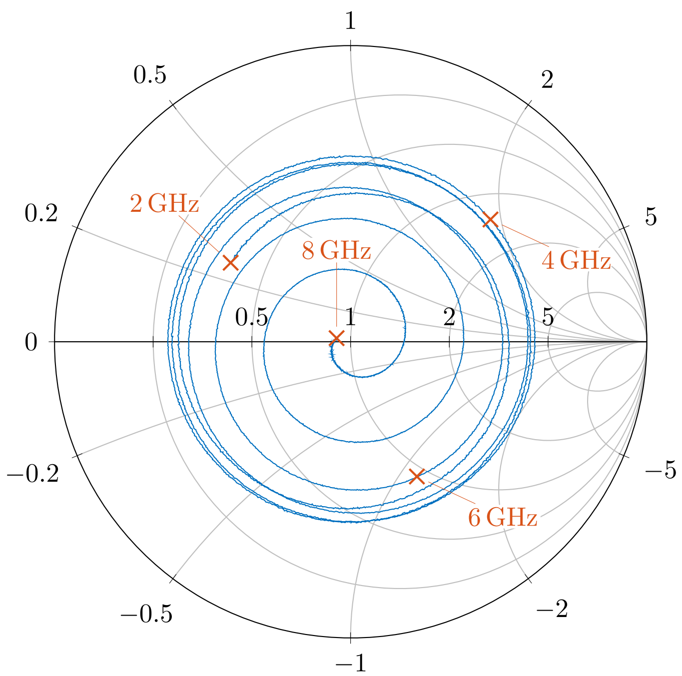

Figure 4.16: Measurement of a typical tuner trajectory of an electro-mechanical slide-screw tuner, the *Maury MT982A*.

Imperfections are especially critical for load-dependent X-parameters. In many cases, like in the setup presented in Section 4.6, passive automated slide-screw tuners are utilized for providing the desired model loads $\Gamma_{L,M}^{(n)}$. Compared to an active load-pull setup, these tuners are cheaper and easier to control. However, they offer a controlled reflection coefficient only for a single frequency, while at all other considered frequency points the input reflection coefficient is determined by the frequency response of the tuner, which is often highly reflective. In Figure 4.16 the tuner trajectory of one of the utilized *Maury MT982A* tuners is shown. For an arbitrarily chosen fundamental load condition, generally a non-zero load reflection coefficient will be observed at the harmonics. This will inherently cause additional large-signal stimuli by reflection of the non-linear response of the DUT. As discussed in Section 3.3, load-dependent X-parameters require, per definition, matched harmonic load conditions. Consequently, a systematic error occurs in the non-linear mapping, i.e. the X^F parameters.

Due to the applied vector calibration, all involved travelling waves are known in magnitude and phase, hence, it is possible to determine the mismatch accurately. Consequently, a correction of this systematic error is possible, as shown in Figure 4.17 [6, 99]. As can be seen in this graph, the desired or ideal stimulus

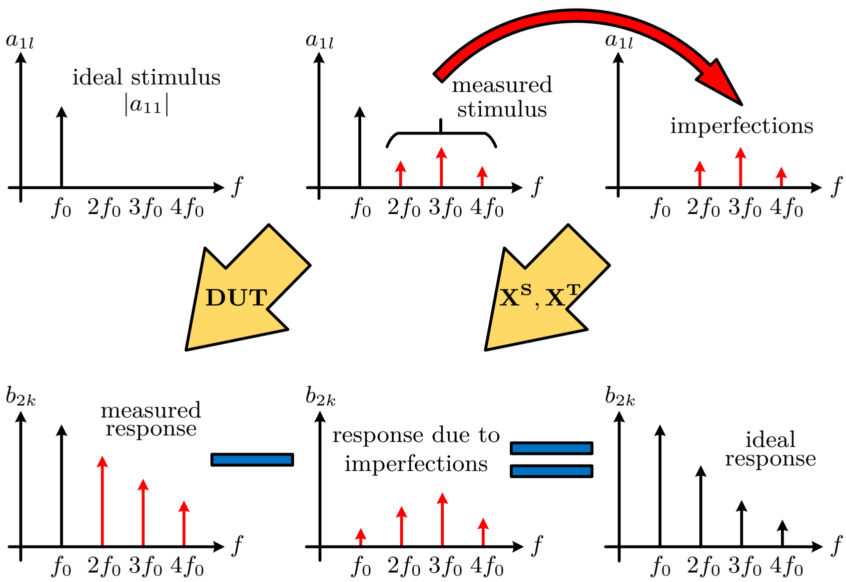

Figure 4.17: Correction procedure of setup imperfections.

for the extraction of X-parameters is a single large-signal input. However, due to imperfections in the setup, the measured large-signal stimulus shows harmonic content. Fortunately, these imperfections can be separated easily. By considering that the LSOP is only negligibly affected, the spectral mapping terms can be determined according to the offset phase technique, as presented in Section 3.4.2. Since the imperfections are known, an isolated ”response due to imperfections” can be calculated by using the spectral mapping terms, i.e., the corresponding X^S and X^T parameters. This can be subtracted from the measured response to get a compensated response, which is the best estimate for the response under ideal conditions.

This procedure can easily be applied since all valid quantities are known. However, one has to bear in mind that this is only possible if the deviation from the LSOP is negligible. Otherwise, the spectral mapping terms cannot be determined accurately, which would lead to an additional error. Furthermore, this correction is only accurate if the harmonic content of the real stimulus is sufficiently small, otherwise the harmonic superposition principle is violated, hence, the systematic error cannot be corrected.

To determine the accuracy of the correction for the used setup and DUT, test measurements were performed. A load-dependent X-parameter model was generated under ideal load conditions. These "ideal load conditions" were realized by using a cascaded harmonic tuning load-pull setup, which allows to ensure matched harmonic loads, while providing an arbitrary model load condition at the fundamental frequency. Since only two tuners were available, the measurement frequency was chosen in order to achieve a maximum return loss at the third order harmonic. Additionally, similar measurements were performed, while varying the second harmonic load impedance over the tuning range. These measurements were performed at 2.6 GHz, a drain quiescent current of $I_{D,q} = 10\,\text{mA}$, an input power of 32 dBm, and a source impedance of $50\,\Omega$. Consequently, highly nonlinear operation is satisfied.

Using these measurements, load-dependent X-parameters were generated. In a first step, the offset phase technique was utilized without correction. Secondly, the same procedure was used, however, also the harmonic mismatch correction, shown in Figure 4.17, was applied. Both procedures were implemented in *MATLAB*.

To determine the accuracy of the gained models, the responses were compared to the load-dependent X-parameter model, gained for ideal load conditions. As an error metric, the mean squared error (MSE) for the drain voltage waveform was used. It is defined as

$$\text{MSE} = 10 \cdot \log_{10}\left[\frac{1}{T}\int_{t=0}^{T}\left(V_D(t) - \hat{V_D(t)}\right)^2 dt\right], \tag{4.8}$$

with $V_D(t)$ is the voltage waveform for ideal conditions and $\hat{V_D(t)}$ the prediction for different mismatches in the model extraction. Note that the DC component is removed from the drain voltage, because it cannot directly be measured with the NVNA.

The results are depicted in Figure 4.18, showing MSE contours depending on the second harmonic load mismatch during extraction and the corresponding drain voltage waveforms.

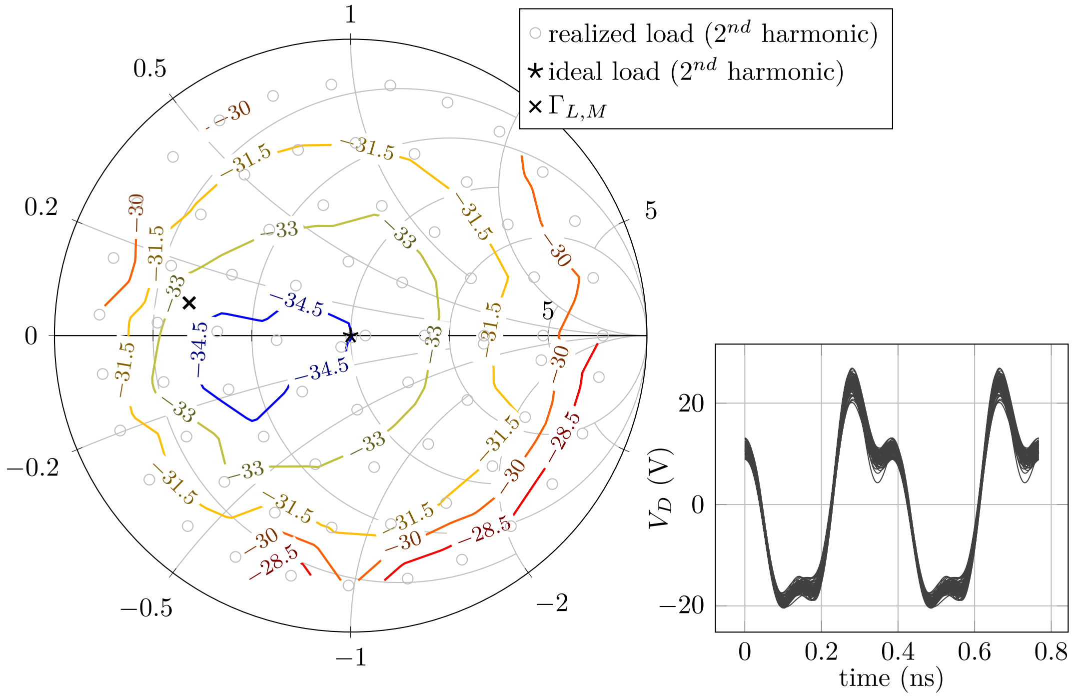

(a) Uncorrected model

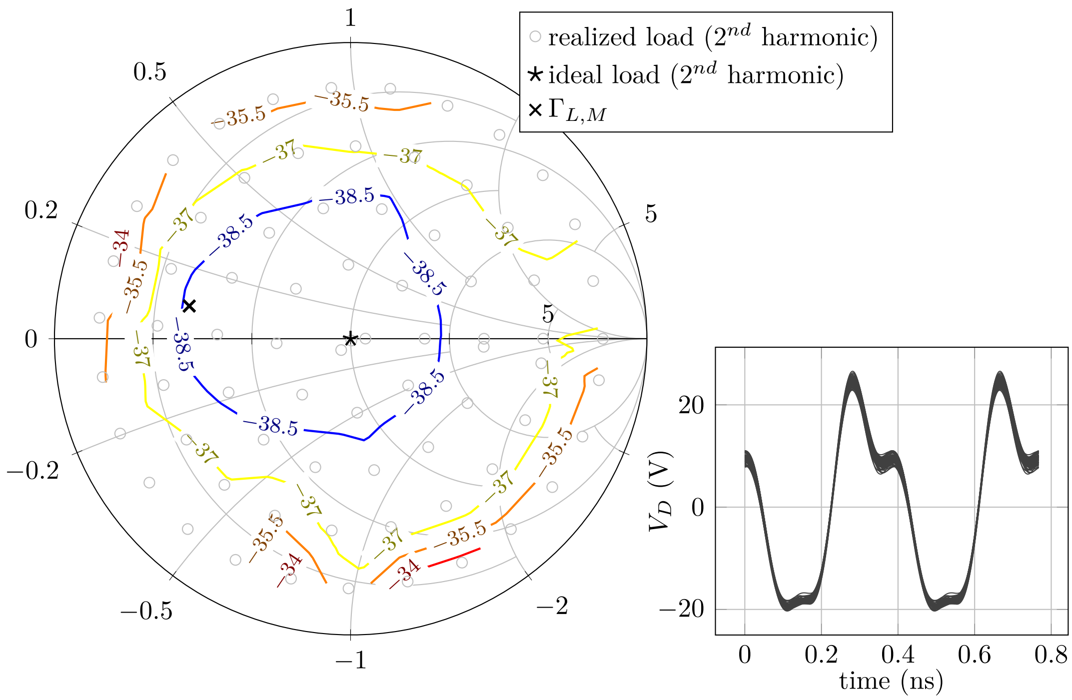

(b) Corrected model

Figure 4.18: Measured model MSE (dB) contour for generated load-dependent X-parameters, for different second harmonic load mismatches, with corresponding drain voltage waveforms.

It can be seen that the observed error is significantly reduced if the correction is applied. The maximum observed MSE can be reduced by more than 6 dB for the used load conditions. The effect of the correction can also be seen in the reduced spread in the voltage waveforms. This shows that even for a highly non-linear DUT this correction shows good results, hence the use of electro-mechanical tuners still allows to generate accurate load-dependent X-parameter models.

4.8 Load-dependent X-parameters for Device Modeling

As stated in Chapter 3, load-dependent X-parameters offer the possibility to be used for device modeling. When used in PA design, high prediction accuracy has to be satisfied for highly mismatched environments. Since X-parameters are based on linearization techniques, their accuracy is limited for highly non-linear DUTs. However, load-dependent X-parameters can by utilized in combination with LUT techniques, as discussed in Section 3.3. For highly efficient PA topologies, defined harmonic terminations are necessary [5]. Consequently, predicting the response for harmonic mismatch accurately is crucial.

To analyze the accuracy of load-dependent X-parameters for harmonic mismatch, load-dependent X-parameters were generated using the given DUT. The model prediction was compared with verification measurements gained from the same device [100]. During the verification measurements, the second harmonic load was changed by using a cascaded harmonic tuning load-pull setup. Since only two tuners were available, a controlled adjustment was only possible for the fundamental and second order harmonic load, the third order harmonic load is given according to the combined tuner trajectory of the two used load tuners. For achieving a maximum VSWR at the third order harmonic load for the combined tuner trajectory, a fundamental frequency of 2.4 GHz was chosen. There, a large third order harmonic load variation was observed, at higher frequencies the tuners show greater return loss, see Figure 4.16. The chosen load conditions are depicted in Figure 4.19a.

For the measurements, the transistor was biased with a drain quiescent current of $I_{D,q} = 10\,\mathrm{mA}$. To operate the DUT in deep compression, an input power of 32 dBm was chosen with a 50 Ω source impedance.

As an error metric, again the MSE on the drain voltage waveform was used, see Equation (4.8). The resulting error contours are depicted in Figure 4.19b. It leads to irregular contours, which is mainly caused by the uncontrolled third order harmonic load. However, for all load conditions the MSE is very small and, most importantly, the spread of the observed MSE values is also small.

As a consequence of this irregular contour, power sweep measurements were

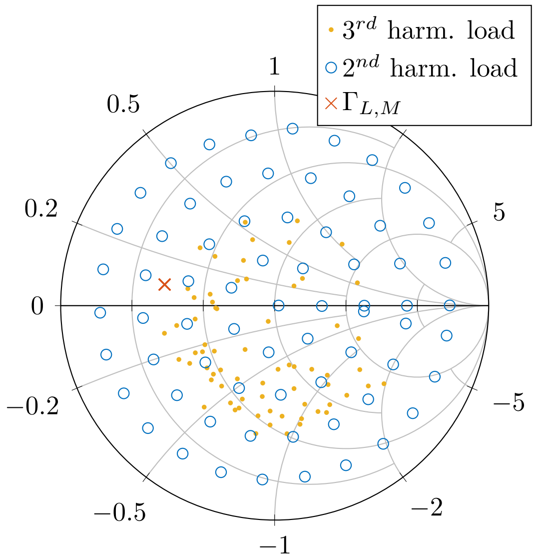

(a) Load conditions

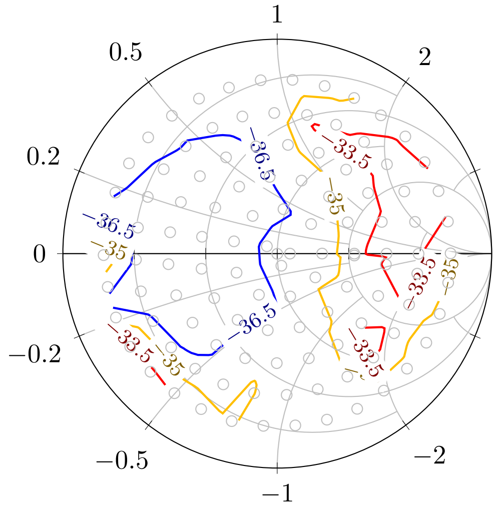

(b) MSE (dB)

Figure 4.19: MSE (dB) of the drain voltage waveform for combined second and third order harmonic load mismatch.

performed for load conditions, where the highest and lowest MSE were observed. The used load conditions are depicted in Figure 4.20a and Figure 4.20b, respectively.

Figure 4.20c shows results for measured gain and MSE depending on the input power, for the largest observed error. It can be seen that the MSE increases for rising input power levels. Consequently, as expected, the error gets larger for strong non-linearity. However, even in deep compression, the MSE stays way blow −30 dB. A comparison for measured and simulated drain voltage waveform for the largest MSE is depicted in Figure 4.20e.

Similar results were gained for load conditions showing the smallest MSE. These are depicted in Figure 4.20b and the power sweep results are shown in Figure 4.20d. In Figure 4.20f the measured and simulated drain voltage waveform is compared for the highest input power level. It can be seen, that very good agreement can be achieved.

Note that for both power sweeps, performed for highest and lowest observed MSE in the contour plot, respectively, slightly different MSE values are observed. This is a consequence of the limited tuning sensitivity of the cascaded harmonic tuning load-pull setup, see Section 2.4.1. Especially for large reflection coefficients, the fundamental frequency load condition changes slightly when adjusting the second order harmonic load.

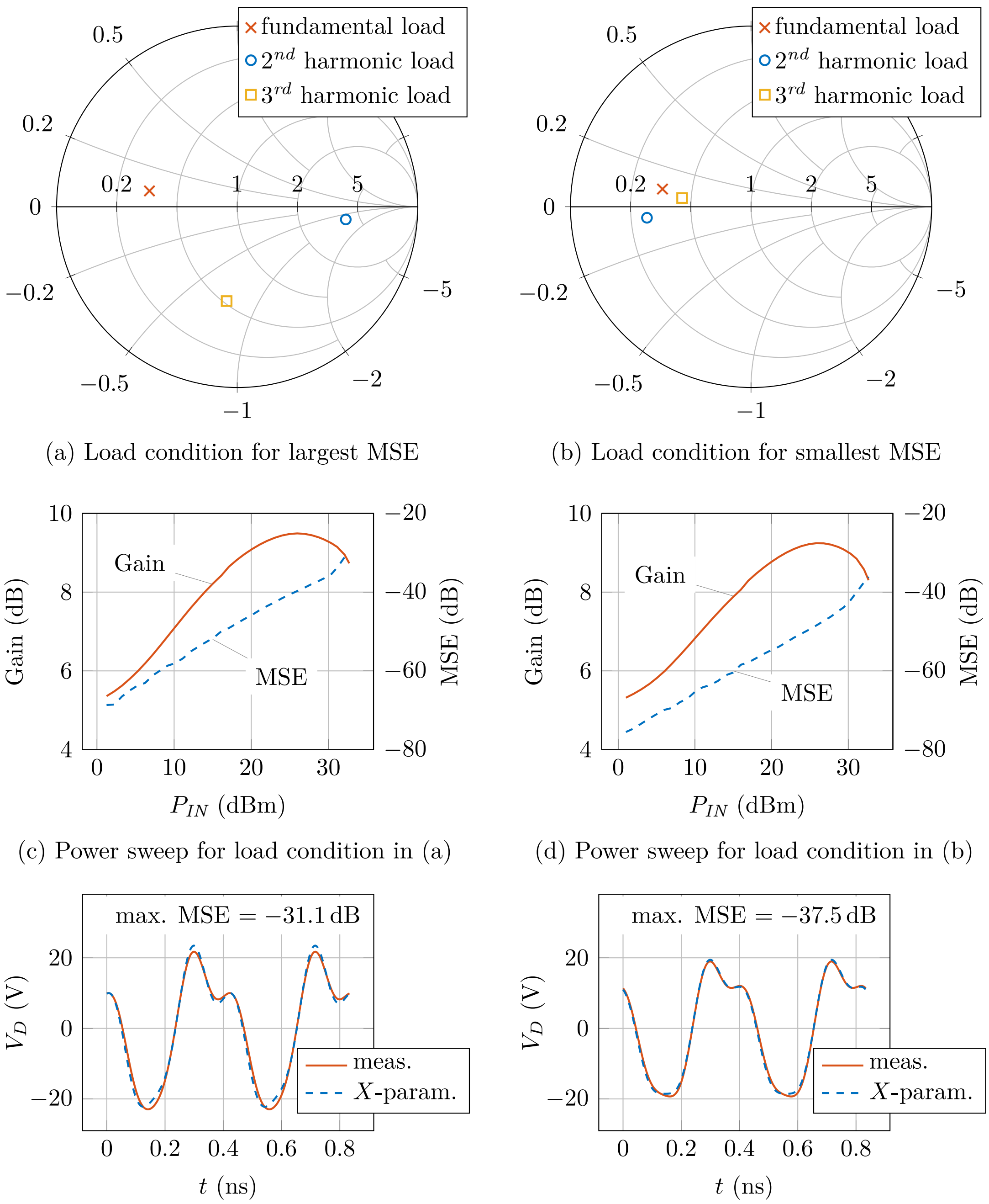

(a) Load condition for largest MSE

(b) Load condition for smallest MSE

(c) Power sweep for load condition in (a)

(d) Power sweep for load condition in (b)

(e) Drain voltage waveform, for load condition in (a), $P_{IN} = 32\,\text{dBm}$

(f) Drain voltage waveform, for load condition in (b), $P_{IN} = 32\,\text{dBm}$

Figure 4.20: Analysis of the X-parameter prediction for largest and smallest MSE observed in Figure 4.19b.

Consequently, this additional deviation of the fundamental frequency load condition will cause a lowered model prediction accuracy. However, due to the very small observed errors, load-dependent X-parameters can be seen as a perfect model to predict the response of a strongly non-linear DUT with high accuracy.

4.9 Summary

For generating measurement-based black-box behavioral models like, e.g., X-parameters, special measurement hardware is necessary to be able to measure the response of a non-linear DUT. Over the years, two different approaches emerged as most practical and became commercially available, the LSNA and the NVNA, i.e., a sampler based and a mixer based instrument, respectively. Although both are perfectly capable of performing non-linear model extraction measurements, the NVNA has replaced the LSNA due to its better dynamic range and its generality, i.e., it can as well be used as a "normal" VNA, without any modifications in the setup.

When measuring a non-linear DUT, the NVNA measures the signal components at the fundamental frequency and at the harmonics consecutively. To be able to reconstruct the signal, the cross-frequency phase is needed. Therefore, two HPRs are used to determine the cross-frequency phase: One, which is always measured using an additional receiver and a second one, which is perfectly known, during calibration. These HPRs are typically comb generators. To be able to perform accurate measurements, on top of the already mentioned phase calibration, a full 2-port vector calibration as well as power calibration is necessary.

With a fully calibrated NVNA, X-parameters can be extracted of a certain DUT. For this work, a GaN HEMT by *CREE*, the *CGH40010F* is used. To be able to measure X-parameters of this DUT, the high power measurement configuration is necessary, in order not to damage the measurement instrument and operate it in the linear range. Therefore, external couplers, attenuators, and driving amplifiers are used. Furthermore, a passive load-pull setup was introduced to be able to measure load-dependent X-parameters.

Adding external components and passive slide-screw tuners may add imperfections to the setup, causing a systematic error in the X-parameter extraction. Especially, tuners often violate the required harmonic matching condition. However, it is possible to correct this error in the model extraction procedure by using the generated spectral mapping terms of the X-parameters. This allows to generate load-dependent X-parameters using passive tuners, which are able to accurately predict the behavior of the given GaN HEMT, even for a large harmonic mismatch.

Chapter 5

Higher Order Approximation

As discussed in Chapters 3 and 4, X-parameters can be used for device modeling. Therefore, load-dependent X-parameters are utilized to handle DUTs in highly mismatched environments. However, this requires prior knowledge of the behavior of the DUT, in order to use a meaningful model definition load $\Gamma_{L,M}$. For an unknown DUT finding an appropriate model definition load would lead to either an LUT using multiple load conditions $\Gamma_{L,M}^{(n)}$ and therefore, large model size, or a trial-and-error approach for determining an optimum model definition load. This is not very useful in practice.

A different approach for achieving an increased model accuracy is to assess the properties of X-parameters. As discussed earlier in this work, X-parameters rely on the concept of describing functions and utilize a Taylor series based linearization to allow for a model which is scalable and easy to be implemented. Based on the describing function approach, several approaches have been proposed to increase the model prediction accuracy. All these approaches rely on approximation techniques, which try to find a reliable and useful description of the DUT. One candidate is the Cardiff model, which is already discussed in Section 2.4.5. Another approach utilizes Padé approximation, allowing to achieve higher accuracy compared to X-parameters [101]. However, to stay in the same modeling and measurement framework, an extension to X-parameters is desired.

It is possible, to extend the Taylor series approximation to higher orders. By including the second order terms, the so-called QPHD or quadratic PHD model can be formed [102, 103]. This has the benefit that it is basically an augmentation of the well-known X-parameters with additional terms. It is formed as

$$
\begin{aligned}
b_{pk} = {} & X^{F}_{pk}(|a_{11}|)P^{k} \\
& + \sum_{(q,l)\neq(1,1)} X^{S}_{pk,ql}(|a_{11}|)P^{k-l} \cdot a_{ql} \\
& + \sum_{(q,l)\neq(1,1)} X^{T}_{pk,ql}(|a_{11}|)P^{k+l} \cdot a^{*}_{ql} \\
& + \sum_{(q,l)\neq(1,1)} X^{U}_{pk,ql}(|a_{11}|)P^{k-2l} \cdot a^{2}_{ql} \\
& + \sum_{(q,l)\neq(1,1)} X^{V}_{pk,ql}(|a_{11}|)P^{k+2l} \cdot a^{*2}_{ql} \\
& + \sum_{(q,l)\neq(1,1)} X^{W}_{pk,ql}(|a_{11}|)P^{k} \cdot a^{*}_{ql} \cdot a_{ql}.
\end{aligned} \tag{5.1}
$$

Consequently, the parameters X^F, X^S, and X^T are defined as in Equations (3.2) and (3.4). The additional second order parameters are derived as

$$X^{U}_{pk,ql} = \left.\frac{\partial^2 F_{pk}}{\partial(a_{ql}P^{-l})^2}\right|_{|a_{11}|} = \left.\frac{\partial^2 F_{pk}}{\partial a^{2}_{ql}}\right|_{|a_{11}|} \cdot P^{2l} \tag{5.2a}$$

$$X^{V}_{pk,ql} = \left.\frac{\partial^2 F_{pk}}{\partial(a_{ql}P^{-l})^{*2}}\right|_{|a_{11}|} = \left.\frac{\partial^2 F_{pk}}{\partial a^{*2}_{ql}}\right|_{|a_{11}|} \cdot P^{-2l} \tag{5.2b}$$

$$X^{W}_{pk,ql} = \left.\frac{\partial^2 F_{pk}}{\partial(a_{ql}P^{-l})\partial(a_{ql}P^{-l})^{*}}\right|_{|a_{11}|} = \left.\frac{\partial^2 F_{pk}}{\partial a_{ql}\partial a^{*}_{ql}}\right|_{|a_{11}|}. \tag{5.2c}$$

Due to the introduction of this higher order terms, an increased model prediction accuracy can be achieved in highly mismatched environments. A similar approach can be found in the enhanced polyharmonic distortion (EPHD) model [104].

5.1 Model Extraction

For the formulation of the QPHD model, the main intention is to rely on the same model extraction framework as for X-parameters. Consequently, the offset phase technique, as discussed in Section 3.4.2, is desired to be utilized. However, it turns out that using a small-signal ET often leads to an ill-conditioned set of equations during extraction. Consequently, a robust parameter extraction is not possible.

Providing a larger ET would allow for a better condition number, but, especially at the output port, this would require an ET driver amplifier with very high output power, which is often not available. To overcome this issue, load-pull

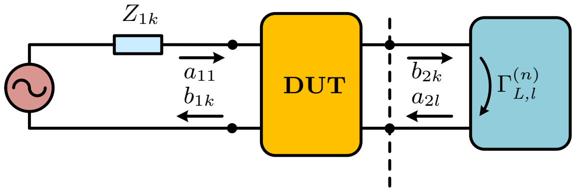

Figure 5.1: Block diagram for extracting higher order PHD modeling parameters.

techniques are utilized to emulate the offset phase technique, as shown in the block diagram in Figure 5.1 [105]. There, a defined mismatch is applied at the output of the DUT. Due to this mismatch, the non-linear response is reflected and causes an additional input. This can be written as

$$a_{2l}^{(n)} = b_{2k} \cdot \Gamma_{L,l}^{(n)}. \tag{5.3}$$

By varying a certain load condition $\Gamma_{L,l}^{(n)}$, the input wave $a_{2l}^{(n)}$ changes, which can be interpreted as an ET. An example of possible load conditions used for model extraction is depicted in Figure 5.2. To be able to extract the model, at least six

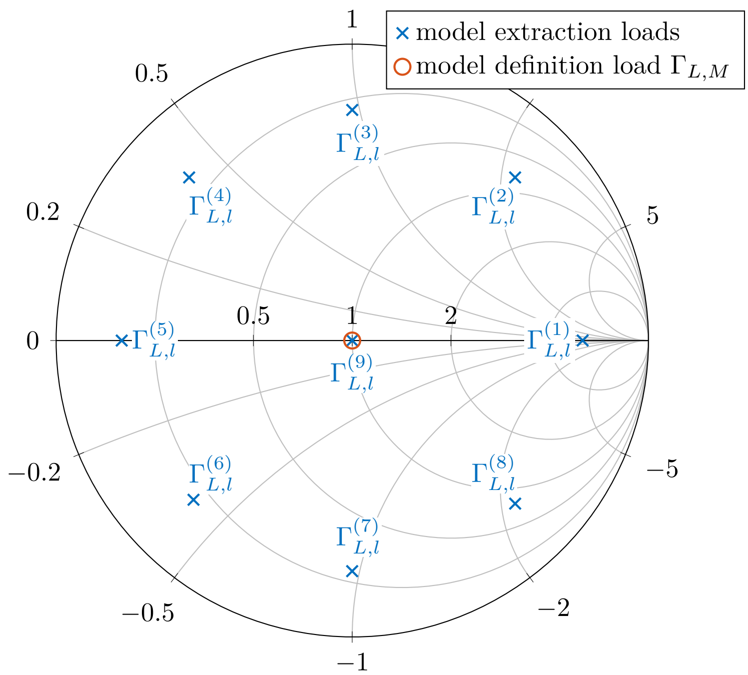

Figure 5.2: Example of utilized loads for QPHD parameter extraction [105].

different load conditions are necessary due to the increased number of parameters.

Unlike load-dependent X-parameters, the used load conditions are not included in the model, hence, the QPHD model is defined at the model definition load $\Gamma_{L,M} = 0$. Similar to the offset phase technique, the parameters are extracted by solving a set of linear equations, which is formed as

$$\begin{pmatrix} b_{ik}^{(1)} \\ \vdots \\ b_{pk}^{(\mathrm{N})} \end{pmatrix} = \begin{pmatrix} 1 & a_{ql}^{(1)} & a_{ql}^{*(1)} & a_{ql}^{2(1)} & a_{ql}^{*^2(1)} & |a_{ql}^{(1)}|^2 \\ \vdots & \vdots & \vdots & \vdots & \vdots & \vdots \\ 1 & a_{ql}^{(N)} & a_{ql}^{*(\mathrm{N})} & a_{ql}^{2(\mathrm{N})} & a_{ql}^{*^2(\mathrm{N})} & |a_{ql}^{(\mathrm{N})}|^2 \end{pmatrix} \cdot \begin{pmatrix} X_{pk}^{F} \\ X_{pk,ql}^{S} \\ X_{pk,ql}^{T} \\ X_{pk,ql}^{U} \\ X_{pk,ql}^{V} \\ X_{pk,ql}^{W} \end{pmatrix} \tag{5.4}$$

Again, least-squares estimation can be utilized by using an overdetermined set of equations.

The drawback of this technique is, that at each port and each considered harmonic, an independent tuner is necessary to provide the desired load conditions. In practice, this requires extensive measurement hardware, because a full 2-port harmonic tuning setup would be necessary.

As discussed in Section 4.8, the linear approximation used in X-parameters is sufficiently accurate in predicting the harmonic response of a DUT in strongly non-linear operation. Consequently, extracting quadratic terms is only necessary at the fundamental frequency for the given DUT, hence, a reduced QPHD model can be formed. This allows to use the same setup, which is used for generating load-dependent X-parameter models. Furthermore, the increase in model size is limited. As an example: A 2-port X-parameter model up to the third order harmonic comprises 79 parameters. Including the second order parameters for a fundamental frequency ET will add only 18 parameters. This reduced QPHD model is given as

$$\begin{aligned} b_{pk} = {} & X_{pk}^{F}(|a_{11}|)P^{k} \\ & + \sum_{(q,l)\neq(1,1)} X_{pk,ql}^{S}(|a_{11}|)P^{k-l} \cdot a_{ql} \\ & + \sum_{(q,l)\neq(1,1)} X_{pk,ql}^{T}(|a_{11}|)P^{k+l} \cdot a_{ql}^{*} \\ & + \sum X_{pk,21}^{U}(|a_{11}|)P^{k-2} \cdot a_{21}^{2} \\ & + \sum X_{pk,21}^{V}(|a_{11}|)P^{k+2} \cdot a_{21}^{*^2} \\ & + \sum X_{pk,21}^{W}(|a_{11}|)P^{k} \cdot a_{21}^{*} \cdot a_{21}. \end{aligned} \tag{5.5}$$

5.2 Accuracy Analysis

The accuracy of this reduced QPHD model was investigated for the given DUT. Therefore, the measurement setup introduced in Section 4.6, was utilized to generate models as well as verification measurements.

To generate the reduced QPHD model, the load conditions in Figure 5.2 were applied at the output. These load conditions were provided only for the fundamental frequency, according to the model formulation in Equation (5.5). To ensure matched harmonic loads, a triplexer based harmonic tuning load-pull setup was used in the measurements. For the generation of the ET at harmonic frequencies, the offset phase technique was utilized in order to get the remaining parameters. The model extraction procedure was implemented in *MATLAB*. Additionally, X-parameters and load-dependent X-parameters were gained from the same device. These were extracted by the used NVNA. The model load condition was set to $\Gamma_{L,M} = 0$ for X-parameters, while for the load-dependent case $\Gamma_{L,M}$ was set to $0.53\underline{/161.7°}$ which is close to the optimum match for maximum output power for the used DUT at the given frequency.

During the measurements, the DUT was biased with a drain quiescent current of $I_{D,q} = 10\,\mathrm{mA}$, while the excitation frequency was set to 2.5 GHz. Due to the requirements onto the X-parameter extraction, the input load condition was set to 50 Ω for the whole frequency range. To determine the model accuracy, verification measurements were performed. The fundamental load condition at the output was varied over the tuning range of the used tuner, again using a triplexer based harmonic tuning load-pull setup. The input power of the CW excitation signal was set to 32 dBm to ensure highly non-linear operation, while all other operational conditions remained equal to the model extraction measurements.

As an error metric, the MSE for the drain voltage waveform, as defined in Equation (4.8), was chosen. It was calculated for the reduced QPHD model, X-parameters, and load-dependent X-parameters, respectively. The calculated error contours are depicted in Figure 5.3.

The observed MSE for X-parameters is shown in Figure 5.3a. It can be seen that for matched and weakly mismatched loads the observed MSE is very low, while for an increasing magnitude of the output reflection coefficient, the MSE increases significantly. For the given tuning range of the setup, the maximum observed MSE was −16.6 dB. For the load-dependent case a similar accuracy is observed, showing the highest model accuracy around the model load condition $\Gamma_{L,M}$, see Figure 5.3b. Again, for an increasing distance to $\Gamma_{L,M}$, the model prediction error decays rapidly, reaching a maximum of −18.7 dB for the given tuning range.

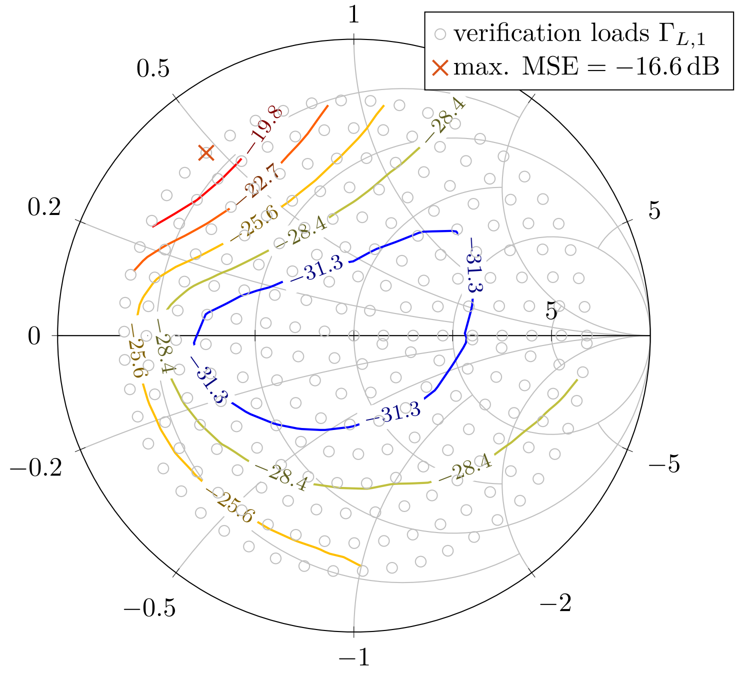

(a) MSE (dB) X-parameters

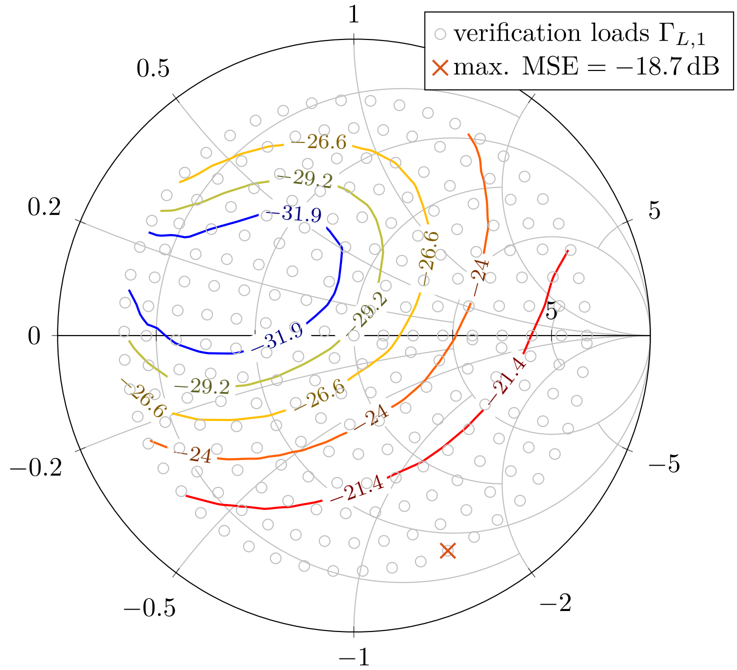

(b) MSE (dB) load-dependent X-parameters $\Gamma_{L,M} = 0.53\angle 161.7°$

Figure 5.3: MSE of the drain voltage waveform for fundamental frequency load mismatch.

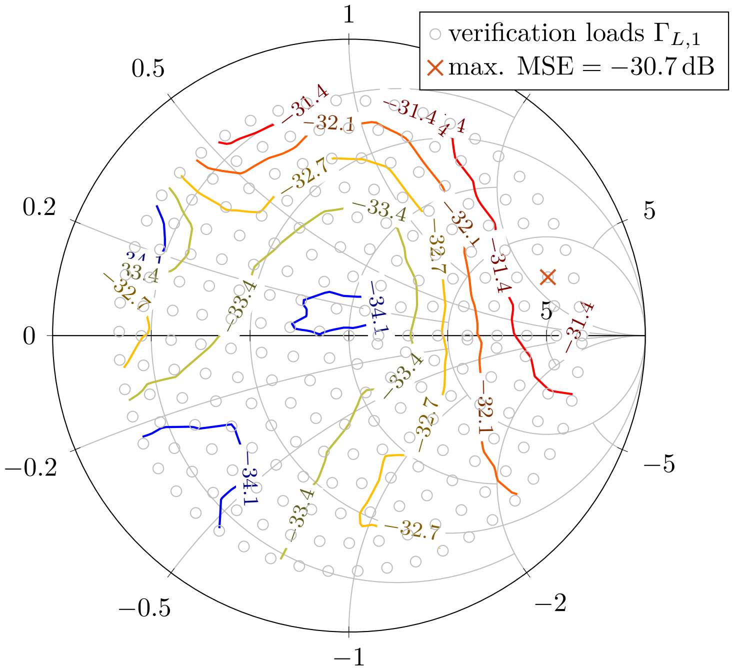

(c) MSE (dB) QPHD

Figure 5.3: MSE of the drain voltage waveform for a fundamental frequency load mismatch.

The MSE error contour for the QPHD model is shown in Figure 5.3c. Similar to X-parameters, the error is very small for matched and weakly mismatched loads. However, even for highly mismatched environments, the observed error remains small, hence, the error spread is also limited. For the given tuning range of the setup, the maximum observed MSE was −30.7 dB. Consequently, a very high model accuracy can be achieved for the given DUT.

In Figure 5.4 the measured and predicted drain voltage waveforms are depicted, at load conditions, for which the maximum MSE for X-parameters (Figure 5.4a), load-dependent X-parameters (Figure 5.4b) and QPHD model (Figure 5.4c) is observed, respectively. The respective load conditions are indicated in Figure 5.3. It can be seen for all presented results that the QPHD model prediction shows very good agreement with the measurements. In contrast, the X-parameter and load-dependent X-parameter model prediction error can clearly be seen in the presented plots, showing worse accuracy than the QPHD model.

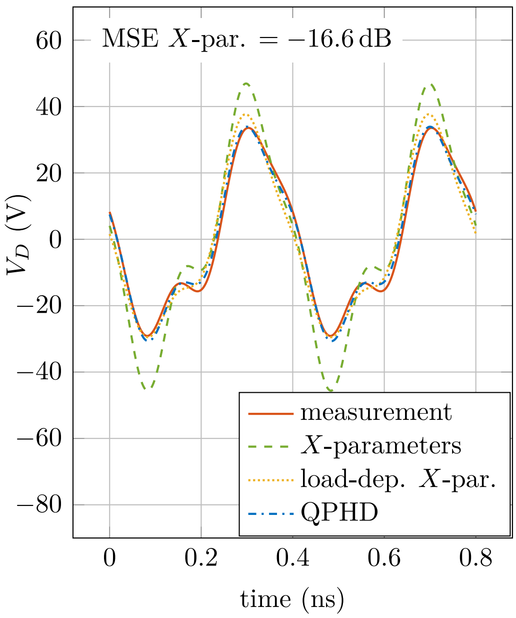

(a) Maximum MSE X-parameters

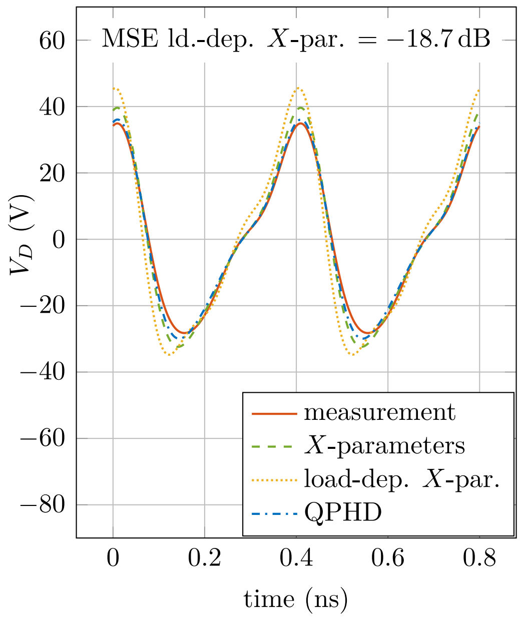

(b) Maximum MSE load-dependent X-parameters ($\Gamma_{L,M} = 0.53\underline{/162°}$)

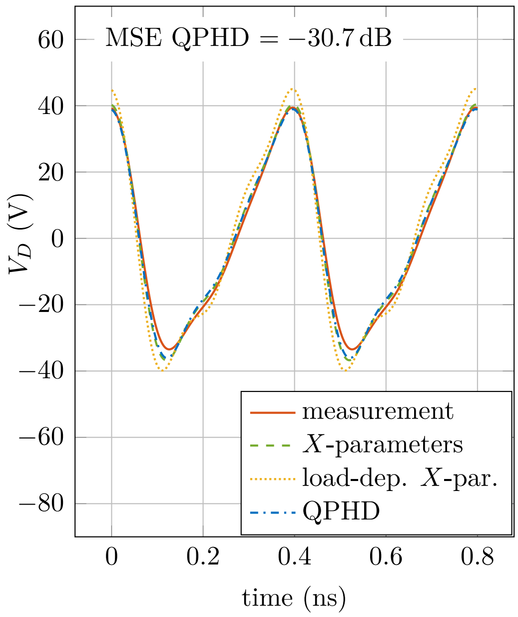

(c) Maximum MSE QPHD model

Figure 5.4: Comparison of the measured and predicted drain voltage waveforms V_D, for load conditions obtaining maximum model error (MSE) for the respective models.

5.3 Dynamic Excitation in Quasi-static Approximation

For many applications it is from interest to be able to predict the response of a DUT under modulated excitation. Especially for state-of-the-art communication systems, this involves complex modulation schemes, designed to achieve high data rates. When assessing such modulation schemes in time domain, typically a time-varying envelope is observed, hence, dynamic effects are present. Additionally, inherent dynamic memory effects occur, which influence the DUT's behavior. This is an issue, because X-parameters and the QPHD model are not able to handle memory effects, they only offer a static model of the DUT. However, it is possible to approximate the dynamic response of a DUT when assuming quasi-static operational conditions, neglecting the influence of the DUT's memory effects [6].

An arbitrary signal $a(t)$, e.g., the signal of a typical state-of-the-art modulation scheme, can be represented by a sum of RF carriers with a time-varying amplitude. Mathematically, this can be written as

$$a(t) = \Re\Big\{ \sum_k a_k(t) e^{j2\pi f_k t} \Big\}, \tag{5.6}$$

with a_k is time-varying envelope of a carrier at the frequency f_k. This envelopes are complex-valued and represented by their amplitude and phase as

$$a_k(t) = |a_k(t)| e^{j\underline{/a_k(t)}} = |a_k(t)| \cdot P_k(t), \tag{5.7}$$

with P as the phasor, which is introduced in Equation (2.19).

When assuming quasi-static conditions, the output of the DUT can be approximated by applying the static X-parameter mapping to the time-varying input signal. Consequently, the quasi-static X-parameter response can be determined by adapting Equation (3.3) to the input in Equation (5.7) as

$$\begin{aligned} b_{pk}(t) = {} & X^F_{pk}(|a_{11}(t)|) P(t)^k \\ & + \sum_{(q,l)\neq(1,1)} X^S_{pk,ql}(|a_{11}(t)|) P(t)^{k-l} \cdot a_{ql}(t) \\ & + \sum_{(q,l)\neq(1,1)} X^T_{pk,ql}(|a_{11}(t)|) P(t)^{k+l} \cdot a^*_{ql}(t). \end{aligned} \tag{5.8}$$

Note that this can easily be adapted in similar fashion for the QPHD model as well.

A typical example for a time-varying envelope signal is a two-tone excitation. Here, the input signal consists of two tones at different frequencies f_1 and f_2, respectively. This signal $s(t)$, using equal signal amplitude for both tones, for simplicity, can be written as

$$\begin{aligned} s(t) = a\cos(2\pi f_1 t) + a\cos(2\pi f_2 t) &= 2a\cos\left(\frac{2\pi\Delta f t}{2}\right)\cos(2\pi f_0 t) \\ &= \Re\left\{2a\cos\left(\frac{2\pi\Delta f}{2}t\right)e^{j2\pi f_0 t}\right\}, \end{aligned} \tag{5.9}$$

with

$$\begin{aligned} f_0 &= \frac{f_1 + f_2}{2}, \\ \Delta f &= f_2 - f_1. \end{aligned} \tag{5.10}$$

Consequently, the time varying envelope is given as

$$a_{11}(t) = 2a\cos\left(\frac{2\pi\Delta f}{2}t\right), \tag{5.11}$$

which can be used for determining the quasi-static response of a two-tone excitation by using X-parameters or the QPHD model.

By using the measurement setup discussed in Section 4.6 and the DUT in Section 4.5, a two-tone measurement was carried out using a tone distance $\Delta f = 20\,\text{kHz}$. Additionally, X-parameters and a QPHD model were generated from the same DUT, to analyze the model accuracy for a two-tone excitation under quasi-static assumption [106]. The measurements were performed at a center frequency of $f_0 = 2.6\,\text{GHz}$ and a drain quiescent current of $I_{D,q} = 10\,\text{mA}$. The time-varying envelope of the two-tone excitation signal can easily be determined using Equation (5.11). This allows to get the magnitude $|a_{11}(t)|$ of the time-varying stimulus, which determines the corresponding X-parameters, see Equation (5.8) and the phasor $P(t)$, defined by the phase of $a_{11}(t)$. These quantities are shown in Figure 5.5, where the magnitude of the input is depicted in Figure 5.5a and the phase in Figure 5.5b. When applied to Equation (5.8), the quasi-static response of the X-parameter model to this two-tone stimulus can be determined. The simulated envelope of $|b_{21}(t)|$ is shown in Figure 5.5c. Apart from the larger amplitude due to the gain of the DUT, it can easily be seen that the shape of the envelope changes. This is caused by non-linear distortion in the DUT.

Transformed to the frequency domain, the signal envelopes become more meaningful. The two-tone excitation signal in baseband is depicted in Figure 5.6a, showing the two input tones symmetrically around the origin. The X-parameter output in baseband, see Figure 5.6b, shows intermodulation products, which originate from the non-linear distortion. Due to the relatively high input power level,

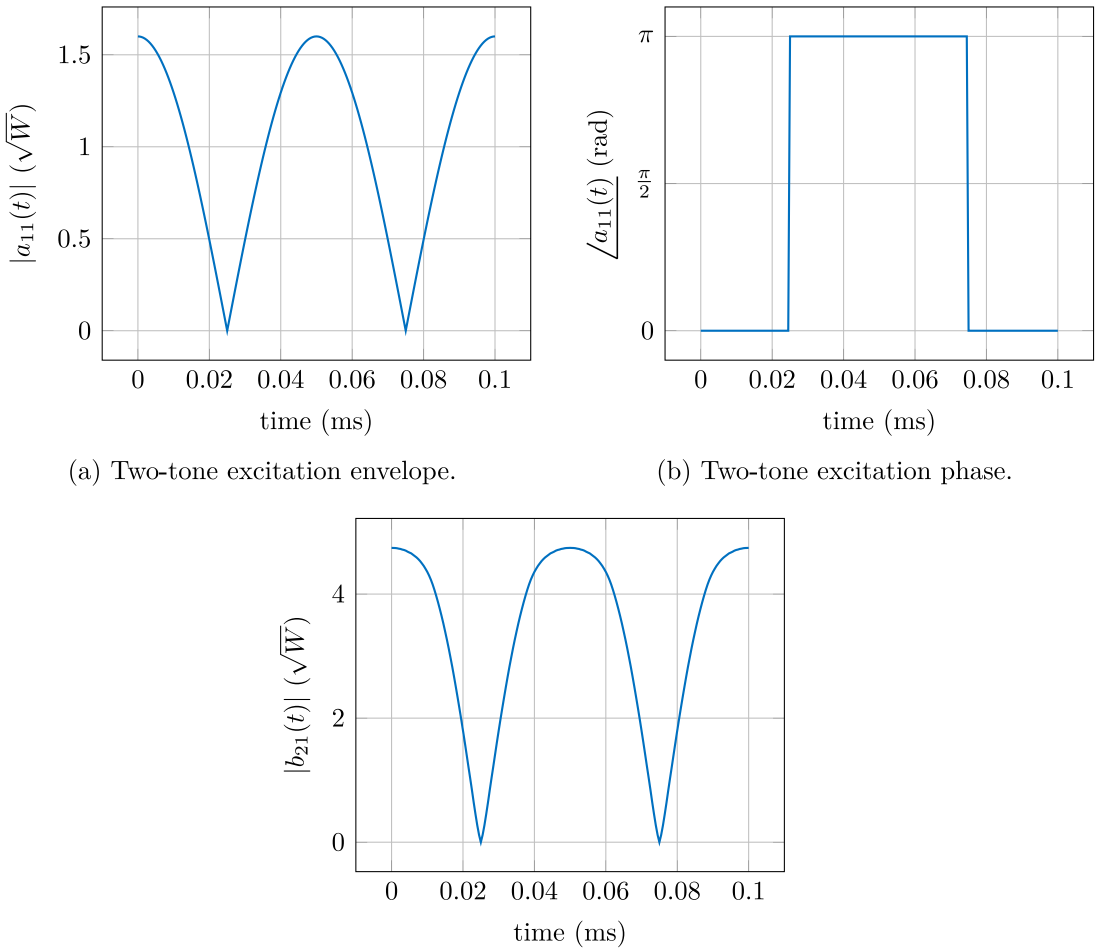

(a) Two-tone excitation envelope.

(b) Two-tone excitation phase.

(c) Two-tone X-parameter response envelope.

Figure 5.5: Time-domain envelope for two-tone excitation and corresponding X-parameter response.

the intermodulation distance is rather small, consequently, strongly non-linear operation is observed. Note that in Figure 5.6b only intermodulation products up to the fifth order are depicted. Higher orders are present, but not depicted, otherwise the plot would get unclear.

To analyze the model accuracy for dynamic excitation analog to the results in Figures 5.5 and 5.6, the quasi-static X-parameter and QPHD model prediction are compared to a two-tone power sweep measurement. Therefore, the measured power level of the two-tone output and the third order intermodulation product (IM3), over input power, are compared to the model prediction. In the

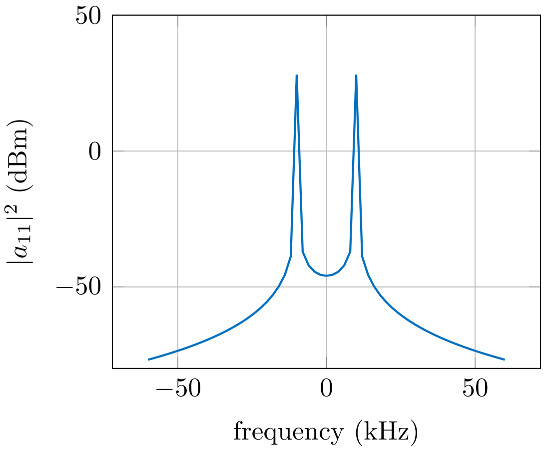

(a) Two-tone excitation.

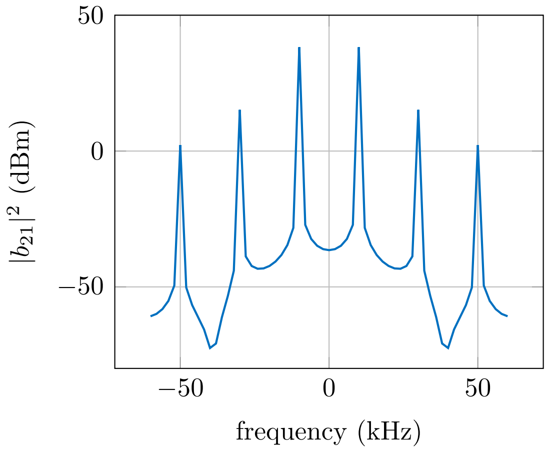

(b) Two-tone X-parameter response.

Figure 5.6: Two-tone spectrum in baseband around a center frequency of $f_0 = 2.6\,\mathrm{GHz}$.

measurements, two different load conditions were used: a $50\,\Omega$ load, i.e., $\Gamma_{L,1} = 0$ and $\Gamma_{L,1} = 0.545\underline{/-179.4^\circ}$.

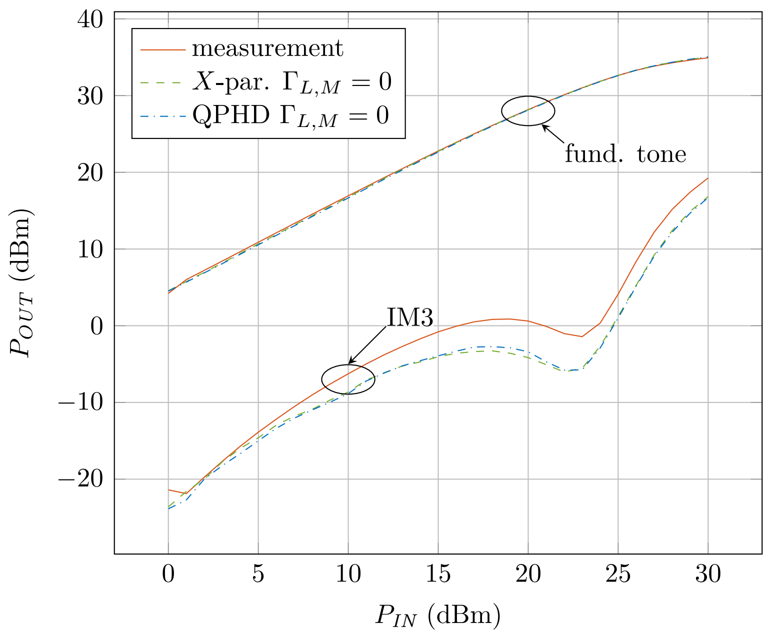

Figure 5.7: Measured and modeled result of a tow-tone experiment for $I_{D,q} = 10\,\mathrm{mA}$, 20 kHz tone spacing, and a load condition of $\Gamma_{L,1} = 0$ [106].

Figure 5.7 shows the result of the first measurement, i.e., $\Gamma_{L,1} = 0$, compared to a quasi-static X-parameter and QPHD model prediction. It can be seen, that the model prediction of both models show equal results, with excellent agreement for the fundamental tone. This is because the load condition for the measurement is equal to the model definition load $\Gamma_{L,M}$ for both models. Consequently, only the non-linear mapping terms are relevant, which are equal for both models. For the predicted IM3 an error is observed, which is due to the limits of the quasi-static approximation.

The result for the second measurement, using $\Gamma_{L,1} = 0.545\underline{/-179.4°}$, is depicted in Figure 5.8. Due to the mismatch to the model load condition, the spectral mapping terms of the models are utilized, consequently, different model prediction results are observed. It can be seen that for the fundamental fre-

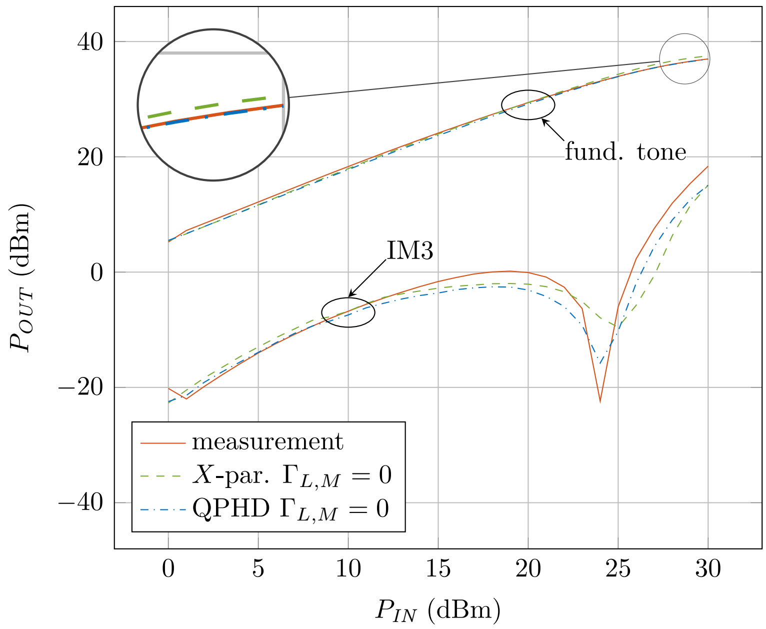

Figure 5.8: Measured and modeled result of a tow-tone experiment for $I_{D,q} =$ 10 mA, 20 kHz tone spacing, and a load condition of $\Gamma_{L,1} = 0.545\underline{/-179.4°}$ [106].

quency component the QPHD model shows excellent agreement with the measurement, while the X-parameter prediction diverges. Especially in compression, i.e., $P_{IN} = 30$ dBm, the X-parameter prediction error reaches 0.54 dB, while for the QPHD model the error reaches only 0.05 dB. The prediction of the IM3 is again limited by the quasi-static approximation, however, for high input power levels the QPHD model shows slightly higher accuracy. Note that for these measurements, a different error metric was used than the MSE. This is because the waveform of the envelope was not accessible from the two-tone measurement.

5.4 Summery

PHD modeling, utilized for X-parameters, is based on a Taylor series based linearization of the describing functions on an LSOP. This offers a practical nonlinear model, however, when used for highly non-linear and load-sensitive devices, their accuracy is limited. To overcome this issue, the Taylor series approximation is expanded to higher orders. Consequently, second order terms are included in the model to form the so-called QPHD model.

It is desired to be able to generate the QPHD model with the same measurement setup as X-parameters, however, when using the offset phase technique similar to an X-parameter measurement, it turns out that the resulting set of linear equations is ill-conditioned in many cases. Consequently, an extraction technique using load-pull measurements is used. This offers a robust extraction technique of the QPHD model. The extraction of the quadratic terms was limited to the fundamental frequency at port 2, firstly, because as already shown in Chapter 4, X-parameters show high accuracy for harmonic load mismatch and secondly, only a fundamental frequency load-pull setup is needed. Consequently, the complexity of the measurement setup remains manageable and the model size is reduced significantly, hence, a reduced QPHD model is formed.

Verification measurements on a GaN HEMT show that the QPHD model allows to generate a model with high accuracy, even for a large mismatch. This tackles the limitations of load-dependent X-parameters, where prior knowledge of the DUT is needed for finding an appropriate model definition load. The measurements show that the model prediction error has a low spread when determined for a wide range of different loads, consequently higher order terms of the Taylor series approximation are not required for the given DUT. Even though, the measurements were performed in deep compression, i.e. strongly non-linear operation.

Additionally, the model's response to a two-tone excitation was analyzed in quasi-static approximation and compared to verification measurements. It can be seen that the QPHD model shows significantly higher accuracy than X-parameters, especially for the predicted response of the fundamental tones. Even the predicted IM3 shows slightly lower error, however, the quasi-static approximation limits the model accuracy for dynamic stimulus.

Chapter 6

Matching Problem

In a design process, models are used to find optimum operational conditions for a DUT, which fit the requirements on the design as good as possible. One of the most common issues in RF circuit design is the matching problem.

For a linear DUT solving the matching problem refers as maximizing the power P_{OUT} at the load impedance Z_L for a given input power P_{IN}. Consequently, the goal for solving the matching problem is to find an appropriate load impedance Z_L for achieving maximum power transfer, or equivalently, an appropriate load reflection coefficient Γ_L. For linear DUTs this is well-known and its solution is the concept of complex conjugate matching. It will be briefly derived in this chapter, for the sake of completeness.

For non-linear DUTs however, the situation is different. For real-world devices, physical limits, like how much voltage they can sustain or how much current it can supply, will influence its behavior [5]. Furthermore, when using active devices such as transistors, the DC power supply has to be considered. This means, that there exist different solutions for the non-linear matching problem, like maximizing the output power or maximizing the efficiency. To solve these problems principally only empirical solutions can be found, as in load-pull measurements. However, it is possible to utilize X-parameters to find equivalent solutions for the non-linear matching problem. Hence, solutions of the matching problem using X-parameters as well as the QPHD model are discussed as follows. Therefore, maximizing the output power as well as the efficiency will be discussed.

6.1 Linear Case

To solve the matching problem for a linear DUT, it reduces to its most general form: A simple linear circuit, consisting of a generator with an output impedance Z_G and a load impedance Z_L, as shown in Figure 6.1.

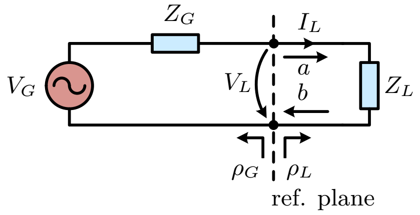

Figure 6.1: Generator matching.

As derived in [107, pp. 77,78], the delivered power into the load Z_L is given as

$$P_{OUT} = \frac{1}{2}\Re\{V_L I_L^*\} = \frac{1}{2}|V_L|^2\Re\left\{\frac{1}{Z_L}\right\}. \tag{6.1}$$

In terms of the generator voltage this can be rewritten as

$$P_{OUT} = \frac{1}{2}|V_G|^2\left|\frac{Z_L}{Z_L + Z_G}\right|^2\Re\left\{\frac{1}{Z_L}\right\}. \tag{6.2}$$

With $Z_L = R_L + jX_L$ and $Z_G = R_G + jX_G$, Equation (6.2) can be reduced to

$$P_{OUT} = \frac{1}{2}|V_G|^2\frac{R_L}{(R_L + R_G)^2 + (X_L + X_G)^2}. \tag{6.3}$$

When assuming a fixed source impedance Z_G, Equation (6.3) has to be stationary for maximizing the delivered power P_{OUT}. As shown in [107, pp. 77,78], to maximize P_{OUT}, Equation (6.3) is differentiated with respect to the real and imaginary part of Z_L, which for the real part leads to

$$\begin{aligned}\frac{\partial P_{OUT}}{\partial R_L} = 0 \rightarrow & \frac{1}{(R_L + R_G)^2 + (X_L + X_G)^2} + \\ & + \frac{-2R_L(R_L + R_G)}{((R_L + R_G)^2 + (X_L + X_G)^2)^2} = 0,\end{aligned} \tag{6.4}$$

or

$$R_G^2 - R_L^2 + (X_L + X_G)^2 = 0. \tag{6.5}$$

For the imaginary part, it results in

$$\frac{\partial P_{OUT}}{\partial X_L} = 0 \rightarrow \frac{-2R_L(X_L + X_G)}{((R_L + R_G)^2 + (X_L + X_G)^2)^2} = 0, \tag{6.6}$$

or

$$R_L(X_L + X_G) = 0. \tag{6.7}$$

Solving Equation (6.5) and Equation (6.7) simultaneously for R_L and X_L results in

$$R_L = R_G \tag{6.8a}$$
$$X_L = -X_G, \tag{6.8b}$$

i.e.,

$$Z_L = Z_G^*, \tag{6.9}$$

or equivalently

$$\rho_L = \rho_G^*, \tag{6.10}$$

This is the well-known conjugate complex matching condition for achieving maximum power transfer.

The concept of conjugate matching is also well-established in practice in finding the optimum load and source impedances in small-signal amplifier design. If the transistor is considered unilateral, i.e., $S_{12} = 0$, maximum power transfer can be achieved by using S_{11}^* and S_{22}^* as source and load reflection coefficients, respectively. This allows to have independent matching networks at the input and output of a 2-port network. In the general, i.e., bilateral case, the input and output matching networks depend on each other, hence, the design of both networks has to be done simultaneously [107, pp. 571,572].

6.2 Non-linear Case

Complex conjugate matching is well established in RF circuit design. However, when it comes to non-linear circuits the situation becomes tricky. Since S-parameters cannot be defined for such circuits and non-linear impedances are hard to determine, a different approach is needed for identifying optimum matching. Furthermore, limits of the generator may influence matching. Traditionally, empirical solutions like load-pull measurements are used to determine the optimum load and source impedances, as discussed in Section 2.4.1. This allows to find the desired mode of operation easily for many applications, but performing load-pull measurements is often time-consuming. Although originally intended to be used as a measurement tool, load-pull measurements can also be utilized in a CAD environment, by using an appropriate device model. However, in many cases a more meaningful solution is desired for the matching problem, similar to the complex conjugate matching in the linear case. Such a solution can be found by using X-parameters as well as the QPHD model, which is discussed as follows, showing results for maximizing the output power as well as the efficiency.

6.2.1 Maximum Output Power

Output power is the most important figure of merit of a PA. Consequently, it is desired to be maximum. In the following, it is discussed how this can be achieved by using PHD modeling based models.

6.2.1.1 X-parameters

It was shown in [108] and [109], that X-parameters can be used to solve the matching problem. Therefore, the traveling wave description is used, differently to the derivation of the complex conjugate matching.

When considering a non-linear 2-port, the fundamental output power into the load at port 2 can be written as

$$P_{OUT} = \frac{|b_{21}|^2 - |a_{21}|^2}{2}. \tag{6.11}$$

Note that again the notation for the traveling waves introduced in Section 3.1 is used here. For maximizing the power at values of a_{21}, the equation has to be stationary. Consequently, Equation (6.12) has to be solved.

$$\frac{\partial P_{OUT}}{\partial a_{21}} = \frac{\partial}{\partial a_{21}} \Big(|b_{21}|^2 - |a_{21}|^2 \Big) = 0 \tag{6.12}$$

This equation is general and always true for maximizing the fundamental output power. To solve the equation with respect to a_{21}, b_{21} has to be substituted. By using the fundamental-only X-parameters, Equation (6.12) can be rewritten as

$$\frac{\partial}{\partial a_{21}} \Big(|X^F_{21} P + X^S_{21,21} a_{21} + X^T_{21,21} P^2 a^*_{21}|^2 - |a_{21}|^2 \Big) = 0. \tag{6.13}$$

For the differentiation of Equation (6.13) the notation is simplified, in order to improve its readability. Therefore, X^F_{21} will be abbreviated as X^F, $X^S_{21,21}$ as X^S, and $X^T_{21,21}$ as X^T. The input wave a_{21} will be abbreviated as just a and b_{21} as b. Consequently, the results of Equation (6.13) lead in simplified notation to

$$\begin{aligned} \frac{\partial P}{\partial a} = \Big(|X^S|^2 + |X^T|^2 - 1 \Big) a^* + X^F X^{T^*} P^{-1} + \\ + X^{F^*} X^S P^{-1} + 2a X^S X^{T^*} P^{-2} = 0. \end{aligned} \tag{6.14}$$

For solving Equation (6.14), Wirtinger calculus is applied [110].Therefore, a and its complex conjugate a^* are treated as independent variables for differentiation.

This allows to form a set of linear equations, which can be written in matrix form as

$$\begin{pmatrix} 2X^S X^{T^*} P^{-2} & |X^S|^2 + |X^T|^2 - 1 \\ |X^S|^2 + |X^T|^2 - 1 & 2X^{S^*} X^T P^2 \end{pmatrix} \cdot \begin{pmatrix} a \\ a^* \end{pmatrix} = \begin{pmatrix} -X^F X^{T^*} P^{-1} - X^{F^*} X^S P^{-1} \\ -X^{F^*} X^T P - X^F X^{S^*} P \end{pmatrix}. \tag{6.15}$$

Equation (6.15) can now be solved with respect to a, leading to an optimum solution for maximum output power P_{OUT} as

$$a_{opt,P} = P \cdot \frac{X^F X^{S^*} \left(|X^T|^2 - |X^S|^2 + 1\right) + X^{F^*} X^T \left(|X^S|^2 - |X^T|^2 + 1\right)}{\left(1 - |X^S|^2 - |X^T|^2\right) - 4|X^S|^2 |X^T|^2} \tag{6.16}$$

The calculation of an optimum for the scattered wave a does not offer a satisfactory solution for the matching problem. To get a more meaningful result the optimum load reflection coefficient is determined, similar to the linear case. It is given as

$$\Gamma_{L,opt,P} = \frac{a_{opt,P}}{b(a_{opt,P})}, \tag{6.17}$$

which can be rewritten by utilizing X-parameters as

$$\Gamma_{L,opt,P} = \frac{a_{opt,P}}{X^F P + X^S a_{opt,P} + X^T P^2 a^*_{opt,P}}. \tag{6.18}$$

When applying Equation (6.16) in Equation (6.18), the optimum load can be expressed as

$$\Gamma_{L,opt,P} = \frac{X^{S^*} \left(1 - |X^S|^2 + |X^T|^2\right) + \left(|X^S|^2 - |X^T|^2 + 1\right) X^T e^{-j2\underline{/X^F}}}{\left(1 - |X^S|^2 - |X^T|^2\right) + 2X^S X^T e^{-j2\underline{/X^F}}}. \tag{6.19}$$

This equation is independent from the incident and reflected waves a and b and only consists of the relevant X-parameters.

As discussed in Section 3.2, the linear S-parameters are a sub-set of X-parameters. For the linear case ($|a_{11}| \simeq 0$), the parameters $X^T \simeq 0$. Consequently, Equation (6.19) collapses to

$$\Gamma_{L,opt,P}(|a_{11}| \simeq 0) = X^{S^*} \cdot \frac{1 - X^{S^2}}{1 - X^{S^2}} = X^{S^*}. \tag{6.20}$$

Again, the optimum match is determined by the complex conjugate of $X^S_{21,21}$, which is equal to S_{22} in the linear case. Consequently, the concept of complex conjugate matching, as discussed in Section 6.1, is again proven.

It is possible to rewrite Equation (6.19) to a more intuitive form [109]. By reformulation, optimum matching can be written as

$$\Gamma_{L,opt,P} = X^{S*}_{21,21} + X^{T}_{21,21} \cdot e^{-j2\phi}, \tag{6.21}$$

with

$$\phi = \angle X^{F}_{21} + \angle\left(\left(1 - |X^{S}_{21,21}|^2 - |X^{T}_{21,21}|^2\right) + 2X^{S}_{21,21}X^{T}_{21,21}e^{-j2\cdot\angle X^{F}_{21}}\right). \tag{6.22}$$

This result can be interpreted geometrically, as the optimum matching is located on a circle around the complex conjugate of $X^{S}_{21,21}$, with a radius of $|X^{T}_{21,21}|$. This is illustrated in Figure 6.2. In this graph, the optimum load was determined by using

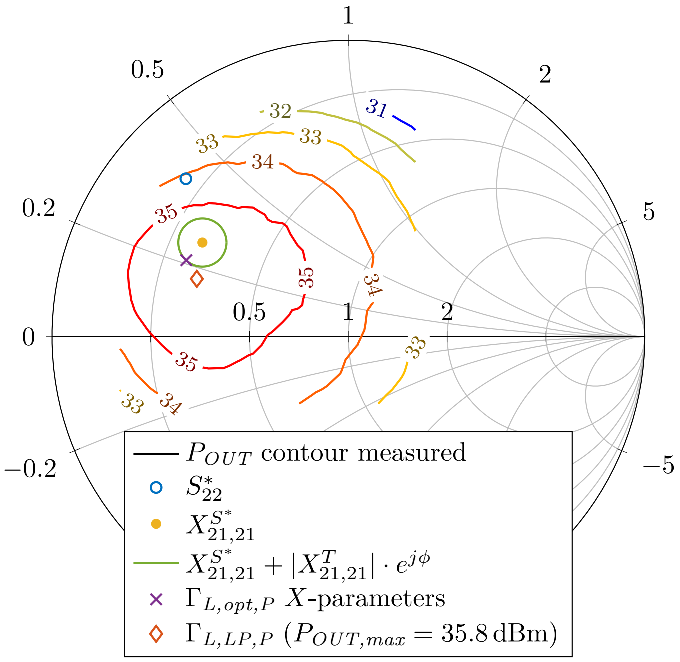

Figure 6.2: Results for the solved non-linear matching problem using X-parameters measured at $P_{IN} = 24.3$ dBm, compared to S^*_{22} and a load-pull contour for equal operational conditions.

Equation (6.21), utilizing measured X-parameters with $\Gamma_{L,M} = 0$. These results were gained using the DUT described in Section 4.5 and the measurement setup in Section 4.6. For the model extraction measurements, the DUT was operated at a drain quiescent current of $I_{D,q} = 10$ mA and an input power of $P_{IN} = 24.3$ dBm. Furthermore, a load-pull measurement was performed to determine the load-pull contour for the output power, as well as, the fundamental load condition for $P_{OUT,max}$, $\Gamma_{L,LP,P}$. Therefore, the triplexer based harmonic tuning load-pull setup was used to ensure unchanged harmonic terminations. For comparison, S-parameters were gained from the same DUT using small-signal excitation.

As can be seen in Figure 6.2, the complex conjugate of S_{22} and $\Gamma_{L,LP,P}$ differ strongly, consequently, non-linear operation is satisfied. Due to the fact that $X^T_{21,21}$ is non-zero, it can be seen that $\Gamma_{L,opt,P}$ is on a circle around $X^{S^*}_{21,21}$, according to Equation (6.21). It can be seen that $\Gamma_{L,LP,P}$ and $\Gamma_{L,opt,P}$ show good agreement, however they are not identical. This small error on the prediction of $\Gamma_{L,opt,P}$ is caused by the limited model accuracy of X-parameters.

6.2.1.2 Quadratic Polyharmonic Distortion Model

As can be seen in Figure 6.2, X-parameters are suited to provide an easy and intuitive solution for the non-linear matching problem of a non-linear DUT. However, as already discussed in Chapter 5, the accuracy of X-parameters is limited for strongly non-linear DUTs.

It is possible however, to use the QPHD model in an equivalent way as in Section 6.2.1.1 [106]. Therefore, Equation (6.13) is rewritten as

$$\begin{aligned} \frac{\partial}{\partial a}\Big(&|X^F P + X^S a + X^T P^2 a^* + X^U P^{-1} a^2 + \\ &+ X^V P^3 a^{*^2} + X^W P^1 a \cdot a^*|^2 - |a|^2 \Big) = 0. \end{aligned} \tag{6.23}$$

Again, the indices in the notation are removed to increase its readability. Due to the applied Wirtinger calculus a and a^* can be treated independently for differentiation, hence, Equation (6.23) results in

$$\begin{aligned} \frac{\partial P}{\partial a} = &\left[X^F X^{T^*} P^{-1} + X^S X^{F^*} P^{-1}\right] + \\ &+ 2a \cdot \left[X^F X^{V^*} P^{-2} + X^S X^{T^*} P^{-2} + X^U X^{F^*} P^{-2}\right] + \\ &+ a^* \cdot \left[X^F X^{W^*} + X^T X^{T^*} + X^S X^{S^*} + X^W X^{F^*} - 1\right] + \\ &+ 2aa^* \cdot \left[X^S X^{W^*} P + X^T X^{V^*} P^{-1} + X^U X^{S^*} P^{-1} + X^W X^{T^*} P^{-1}\right] + \\ &+ 3a^2 \cdot \left[X^S X^{V^*} P^{-3} + X^U X^{T^*} P^{-3}\right] + \\ &+ a^{*^2} \cdot \left[X^S X^{U^*} P + X^T X^{W^*} P^{-2} + X^V X^{T^*} P + X^W X^{S^*} P\right] + \\ &+ 4a^3 \cdot \left[X^U X^{V^*} P^{-4}\right] + \\ &+ a^{*^3} \cdot \left[X^W X^{U^*} + X^V X^{W^*} P^2\right] + \\ &+ 2aa^{*^2} \cdot \left[X^U X^{U^*} + X^V X^{V^*} + X^W X^{W^*}\right] + \\ &+ 2a^2 a^* \cdot \left[X^U X^{W^*} + X^W X^{V^*} P^{-2}\right] = 0. \end{aligned} \tag{6.24}$$

Note, that Equation (6.14) can be derived from Equation (6.24), by setting all quadratic terms to zero, i.e. X^U, X^V, and X^W.

It can be seen, that using the QPHD model leads to a cubic equation after differentiation, which is tricky to solve. However, with its complex conjugate, Equation (6.24) can be rewritten into two equations with two unknown variables a and a^*, which can be solved. A solution of this set of equations can be carried out numerically, using e.g. *MATLAB*. As a consequence of this cubic equation, multiple solutions are obtained when solving Equation (6.24), which may lead to ambiguous results for $\Gamma_{L,opt,P}$.

An example is shown in Figure 6.3, again using the DUT described in Section 4.5 and the measurement setup in Section 4.6. There, $\Gamma_{L,opt,P}$ gained from a

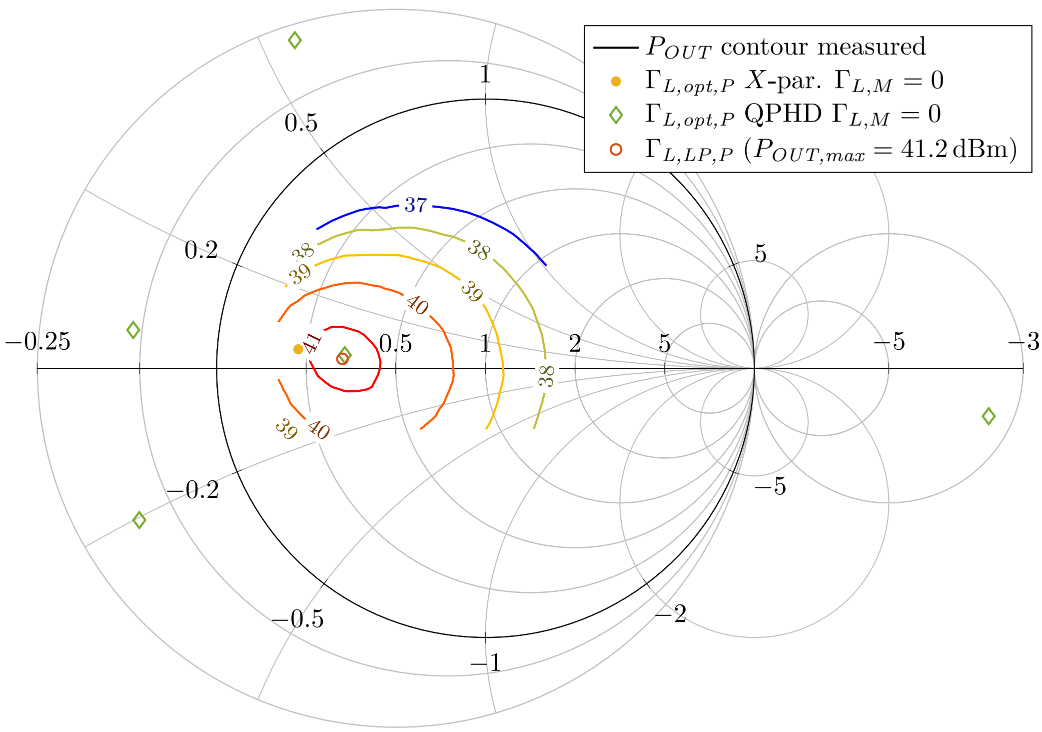

Figure 6.3: Results for determining $\Gamma_{L,opt,P}$ from a QPHD model measured at $P_{IN} = 31\,\mathrm{dBm}$, compared to $\Gamma_{L,LP,P}$ and $\Gamma_{L,opt,P}$ for X-parameters gained for equal operational conditions [106].

QPHD model is compared to $\Gamma_{L,opt,P}$ gained from X-parameters with $\Gamma_{L,M} = 0$ and $\Gamma_{L,LP,P}$. For the load-pull measurement, the triplexer based harmonic tuning load-pull setup was used to ensure unchanged harmonic terminations. All measurements are gained under equal operational conditions, i.e., a drain quiescent current of $I_{D,q} = 10\,\mathrm{mA}$ and an input power of $P_{IN} = 31\,\mathrm{dBm}$, leading to strongly non-linear behavior.

In this graph, all valid solutions for $\Gamma_{L,opt,P}$ are shown. There are five valid solutions in this case, since they have to be complex conjugate. It can be seen that only one obtained value for $\Gamma_{L,opt,P}$ is inside the unit circle. Consequently, only one practically relevant solution is present and all others can be neglected. This residual "valid" solution shows very good agreement with $\Gamma_{L,LP,P}$, the load condition for achieving maximum output power in the load-pull measurement. Comparatively, $\Gamma_{L,opt,P}$ gained from X-parameters do lead to a significant error in predicting the optimum load. These results are equivalent to the results presented in Section 5.2, again showing better accuracy for the QPHD model.

Note that compared to the results in Figure 6.2, the input power level was increased significantly. This was done to illustrate the improved accuracy for adding quadratic terms. Unfortunately, it is not possible to find a simple analytical solution as in Equation (6.21) due to the ambiguous results, however, since only one solution is inside the unit circle for most cases, the QPHD model offers high accuracy for determining the optimum load condition for maximizing the output power.

6.2.2 Maximum Efficiency

When talking about PAs, output power is not the only important figure of merit. Since a PA uses the energy from the DC supply to amplify the RF input signal, efficiency is always important. Similar to Section 6.2.1, it is possible to solve the non-linear matching problem for maximizing the efficiency by using X-parameters as well as the QPHD model, which is discussed as follows.

6.2.2.1 X-parameters

Similar to Equation (6.12), a procedure for maximizing the efficiency has to be found. The efficiency, in this case the drain efficiency, is defined as

$$\eta_D = \frac{P_{RF}}{P_{DC}} = \frac{|b_{21}|^2 - |a_{21}|^2}{2V_D I_D}, \tag{6.25}$$

where V_D is the drain voltage and I_D is the drain current. Again, fundamental-only X-parameters are utilized to be able to solve the matching problem. As discussed in Chapter 3, it is possible to model the DC response by X-parameters. When considering a constant drain voltage V_D the drain current I_D can be substituted using Equation (3.6b), so Equation (6.25) can be rewritten as

$$\eta_D = \frac{|X^F_{21}P + X^S_{21,21}a_{21} + X^T_{21,21}P^2 a^*_{21}|^2 - |a_{21}|^2}{2V_D \cdot \left[X^I_2 + \Re\{X^Y_{2,21}a_{21}\}\right]}. \tag{6.26}$$

Consequently, a formulation in only X-parameters and the incident wave a_{21} is found [111]. To maximize the efficiency, this equation has to be stationary, i.e.

$$\frac{\partial \eta_D}{\partial a_{21}} = 0. \tag{6.27}$$

By applying Wirtinger calculus [110], a quadratic equation in two variables is found after differentiation as

$$\begin{aligned}
-a_{21}^2 \cdot (X^Y_{2,21} X^S_{21,21} X^{T^*}_{21,21})+& \\
a_{21}^{*^2} \cdot (X^Y_{2,21} X^{S^*}_{21,21} X^T_{21,21} - X^{Y^*}_{2,21} D P^2)-& \\
a_{21} a_{21}^* \cdot (2 X^{Y^*}_{2,21} X^S_{21,21} X^{T^*}_{21,21})-& \\
a_{21} \cdot (4 X^I_2 X^S_{21,21} X^{T^*}_{21,21})+& \\
a_{21}^* \cdot (X^Y_{2,21} C P^3 - 2 X^I_2 D^2 - X^{Y^*}_{2,21} B P)+& \\
|X^F_{21}|^2 X^Y_{2,21} P^2 - 2 B X^I_2 P = 0&,
\end{aligned} \tag{6.28}$$

with

$$B = X^F_{21} X^{T^*}_{21,21} + X^S_{21,21} X^{F^*}_{21} \tag{6.29a}$$
$$C = X^F_{21} X^{S^*}_{21,21} + X^T_{21,21} X^{F^*}_{21} \tag{6.29b}$$
$$D = |X^T_{21,21}|^2 + |X^S_{21,21}|^2 - 1. \tag{6.29c}$$

Since a_{21} and a_{21}^* are treated independently, Equation (6.28) can be rewritten into two quadratic equations in two independent variables [111]. This set of quadratic equations can be solved, leading to an optimum incident wave $a_{21,opt,\eta}$ for maximizing the efficiency. The result for $a_{21,opt,\eta}$ will lead to four solutions, however, since they have to be complex conjugate, only two of them are valid.

It is more intuitive to apply $a_{21,opt,\eta}$ to X-parameters, similar to Equation (6.18) and determine an optimum load reflection coefficient as

$$\begin{aligned}
\Gamma_{L,opt,\eta} =& \frac{a_{21,opt,\eta}}{b_{21}(a_{21,opt,\eta})} \\
=& \frac{a_{21,opt,\eta}}{X^F_{21} P + X^S_{21,21}(a_{21,opt,\eta}) + X^T_{21,21} P^2 (a^*_{21,opt,\eta})}.
\end{aligned} \tag{6.30}$$

Again, two solutions for $\Gamma_{L,opt,\eta}$ are observed, resulting in maximum efficiency. However, only one of them is inside the unit circle, hence, only one practically relevant solution exists. This is shown on an example, illustrated in Figure 6.4. Therefore, measured X-parameters are generated by using the measurement setup discussed in Section 4.6 and the DUT described in Section 4.5. For the measurements the DUT was operated at a drain bias current of $I_{D,q} = 10\,\text{mA}$, an excitation frequency of $f_0 = 2.6\,\text{GHz}$, and an input power of $P_{IN} = 24.3\,\text{dBm}$, which

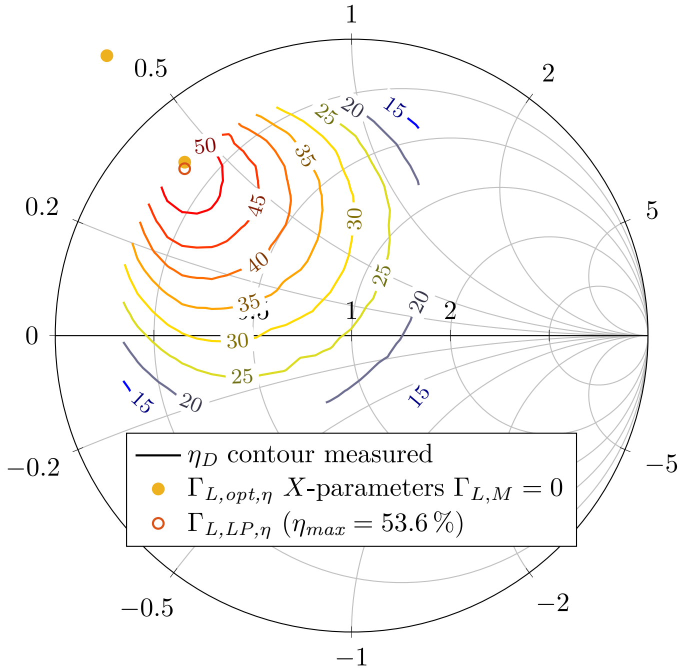

Figure 6.4: Results for the solved non-linear matching problem for drain efficiency using X-parameters measured at $P_{IN} = 24.3\,\text{dBm}$, compared to a load-pull contour for equal operational conditions [111].

leads to weakly non-linear operation. The measured X-parameters were used to gain the optimum load reflection coefficient by using Equation (6.30). Additionally load-pull measurements were carried out using the triplexer based harmonic tuning load-pull setup, to ensure unchanged harmonic terminations. Compared to $\Gamma_{L,LP,\eta}$, the load reflection coefficient for maximum drain efficiency gained from the load-pull measurement, one solution for $\Gamma_{L,opt,\eta}$ shows very good agreement. The second solution does not offer a meaningful result, hence, maximum efficiency can be easily found when using X-parameters.

6.2.2.2 Quadratic Polyharmonic Distortion Model

It has been shown that the QPHD model is suited to predict the optimum load condition for achieving maximum output power accurately. Consequently, its usage for predicting maximum efficiency is also from interest. Using the fundamental-only QPHD model, the outgoing wave b_{21} can be modeled as

$$\begin{aligned} b_{21} = {} & X^F_{21} P + X^S_{21,21} a_{21} + X^T_{21,21} P^2 a^*_{21} + X^U_{21,21} P^{-1} a^2_{21} \\ & + X^V_{21,21} P^3 a^{*2}_{21} + X^W_{21,21} P^1 a_{21} a^*_{21}. \end{aligned} \tag{6.31}$$

Similar to Equation (6.26), this result can be applied to the drain efficiency, which is, for constant drain voltage V_D, derived as

$$\eta_D = \frac{|b_{21}|^2 - |a_{21}|^2}{2V_D \cdot \left[X_2^I + \Re\{X_{2,21}^Y a_{21}\}\right]}. \tag{6.32}$$

Again, a formulation depending only on model parameters and the incident wave a_{21} is found. After differentiation and by applying Wirtinger calculus, two quartic equations in two variables can be identified, which are solvable with respect to a_{21}. Unfortunately, these quartic set of equations is tricky to solve, hence, it was solved numerically using *MATLAB*.

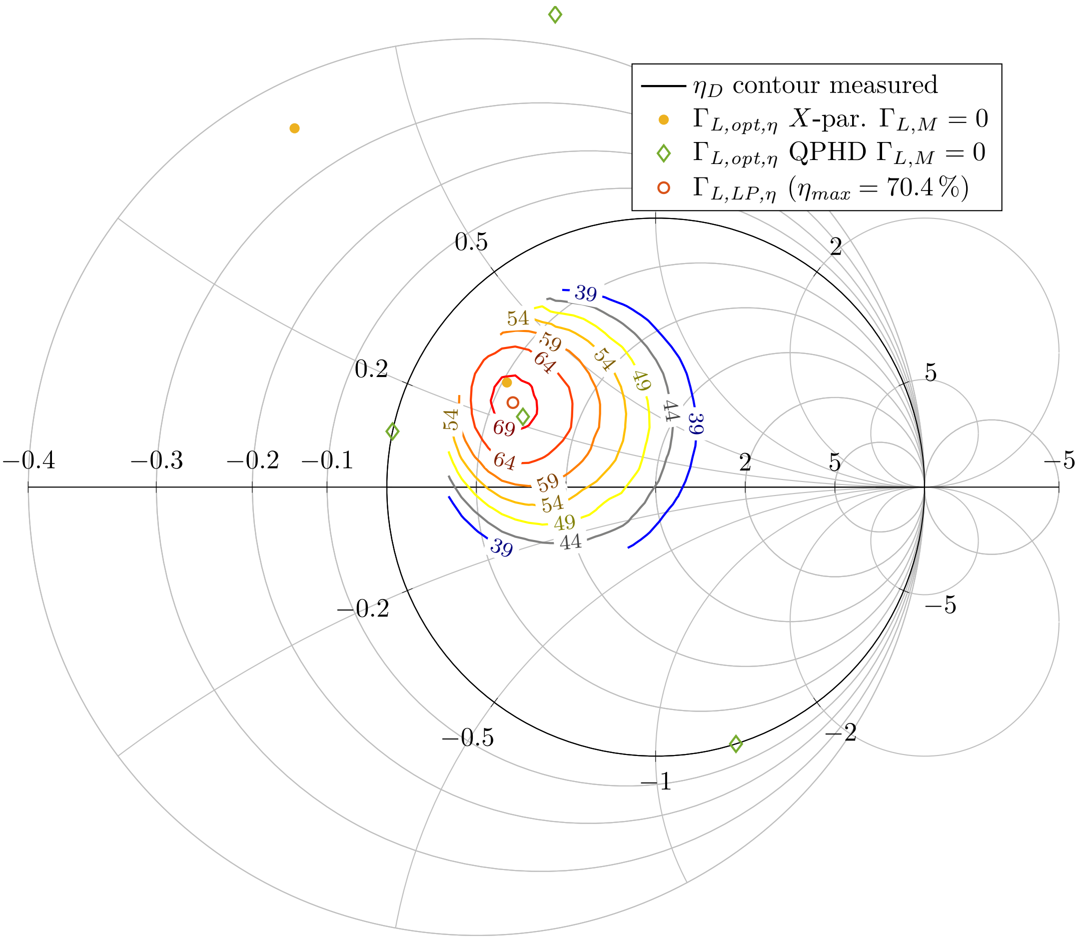

Figure 6.5: Results for determining $\Gamma_{L,opt,\eta}$ from a QPHD model measured at $P_{IN} = 31\,\text{dBm}$, compared to $\Gamma_{L,LP,\eta}$ and $\Gamma_{L,opt,\eta}$ for X-parameters gained for equal operational conditions.

The accuracy of this technique was analyzed on an example. Therefore, X-parameters and a QPHD model were extracted form the DUT described in Section 4.5, while using the measurements setup presented in Section 4.6. In the model extraction measurements, the DUT was operated at a drain quiescent current of $I_{D,q} = 10\,\text{mA}$, an excitation frequency of $f = 2.6\,\text{GHz}$, and an input power of $P_{IN} = 31\,\text{dBm}$, which leads to strongly non-linear operation. Additionally, a load-pull measurement was performed using equal operational conditions, serving as a verification measurement to identify its optimum load condition $\Gamma_{L,LP,\eta}$. Therefore, the triplexer based harmonic tuning load-pull setup was used to ensure unchanged harmonic terminations. In Figure 6.5 the gained results are compared. There, the optimum load reflection coefficient determined from the load-pull measurements $\Gamma_{L,LP,\eta}$, the results for $\Gamma_{L,opt,\eta}$ for X-parameters, and $\Gamma_{L,opt,\eta}$ for the QPHD model are shown. As discussed in the previous section, the X-parameter based result leads to two solutions, with one of them way outside the unit circle. The second solution is close to $\Gamma_{L,LP,\eta}$, leading only to a slight error in predicting the optimum load. The QPHD model based result shows a slightly better agreement with the measurement, however, multiple solutions are obtained due to the quartic equation. Similar to X-parameters, only one of the solutions is inside the unit circle, hence, the single practically relevant solution can easily be identified.

6.3 Power Sweep Measurement Results

To analyze the accuracy of the calculated optimum load conditions, measured X-parameters and QPHD models were used, respectively. These were gained using the measurement setup presented in Section 4.6 and the DUT discussed in Section 4.5 [106]. To get different operational conditions, two different bias conditions were chosen in the measurements. Firstly, a class B operation with a drain quiescent current of $I_{D,q} = 10\,\text{mA}$ and secondly, a class A operation with $I_{D,q} = 500\,\text{mA}$. The input power was varied in a range of $-15 \ldots +32.5\,\text{dBm}$ available input power, in order to obtain different degrees of non-linearity. All measurements were performed at a fundamental frequency of 2.6 GHz and a fixed source impedance of $50\,\Omega$.

Using the stated operational conditions X-parameters, load-dependent X-parameters, and QPHD models were generated. Additionally, small-signal S-parameters were measured of the same DUT. All the presented X-parameters were generated by the NVNA, the QPHD models were extracted as discussed in Section 5.1.

Using the generated models, the optimum load reflection coefficients $\Gamma_{L,opt,P}$ and $\Gamma_{L,opt,\eta}$ were calculated. These were compared to load-pull measurements, specifically the identified optimal load conditions $\Gamma_{L,LP,P}$ and $\Gamma_{L,LP,\eta}$, performed on the same DUT under equal operational conditions as for the model extraction measurements. Therefore, the triplexer based harmonic tuning load-pull setup was used to ensure unchanged harmonic terminations.

6.3.1 Maximum Output Power

By applying the extracted models to the presented techniques in Section 6.2.1, the optimum load conditions for maximizing the output power can be identified. In Figure 6.6 the results for $I_{D,q} = 10\,\mathrm{mA}$ are compared. It can be seen that

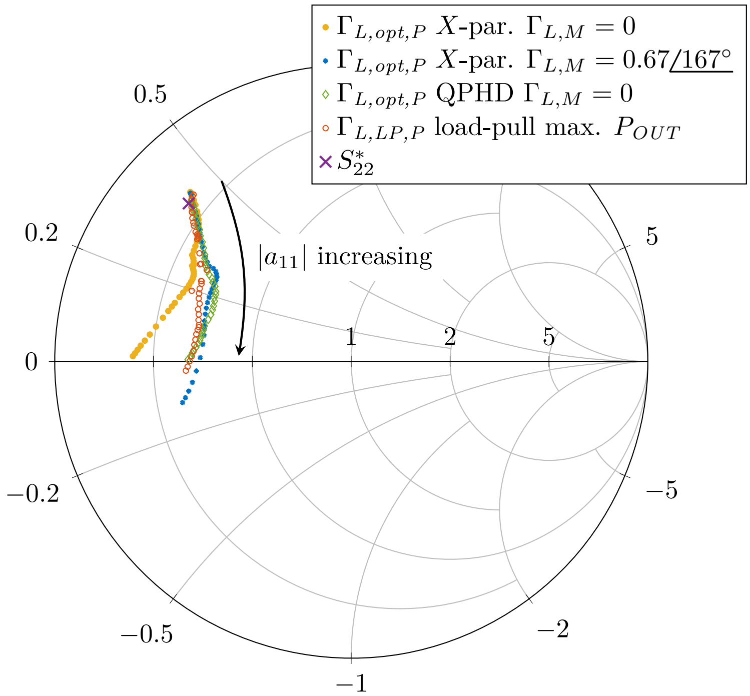

Figure 6.6: Optimum load condition for obtaining maximum output power at $I_{D,q} = 10\,\mathrm{mA}$ and increasing input power, calculated from a $50\,\Omega$ X-parameter, load-dependent X-parameter, and a QPHD model. The results are compared to load-pull measurements and S_{22}^* [106].

for low input power levels, i.e., $P_{IN} = -15\,\mathrm{dBm}$, the optimum load conditions determined by the load-pull measurements $\Gamma_{L,LP,P}$, as well as all calculated values for $\Gamma_{L,opt,P}$, are equal and very close to S_{22}^*. Consequently, linear operation is satisfied. For increasing input power levels (or equivalently increasing $|a_{11}|$), the gained values for $\Gamma_{L,opt,P}$ and $\Gamma_{L,LP,P}$ move counter-clockwise away from S_{22}^*. Hence, the behavior of the DUT becomes increasingly non-linear. It can be seen that especially for $50\,\Omega$ X-parameters ($\Gamma_{L,M} = 0$), the calculated values for $\Gamma_{L,opt,P}$ diverge increasingly from $\Gamma_{L,LP,P}$. For very high input power levels, i.e., strongly non-linear operation, $50\,\Omega$ X-parameters fail to predict optimum matching according to Equation (6.21). Load-dependent X-parameters, with in this case $\Gamma_{L,M} = 0.67\underline{/167^\circ}$, offer higher accuracy, but depend strongly on the model definition load $\Gamma_{L,M}$. Hence, prior knowledge of the behavior of the DUT is required to get an accurate value for $\Gamma_{L,opt,P}$.

For the QPHD model, however, the prediction of $\Gamma_{L,opt,P}$ shows very good agreement with $\Gamma_{L,LP,P}$. This is even true for strongly non-linear operation. Compared to load-dependent X-parameters, optimum matching can be found accurately without any prior knowledge of the behavior of the DUT. Note that only the practically relevant solutions are shown in this graph.

Similar results can be observed for $I_{D,q} = 500\,\text{mA}$, with the difference, that $\Gamma_{L,opt,P}$ doesn't change too much for increasing input power levels. This is shown in Figure 6.7. Note that S_{22}^* seems slightly offset in this graph. However, for very

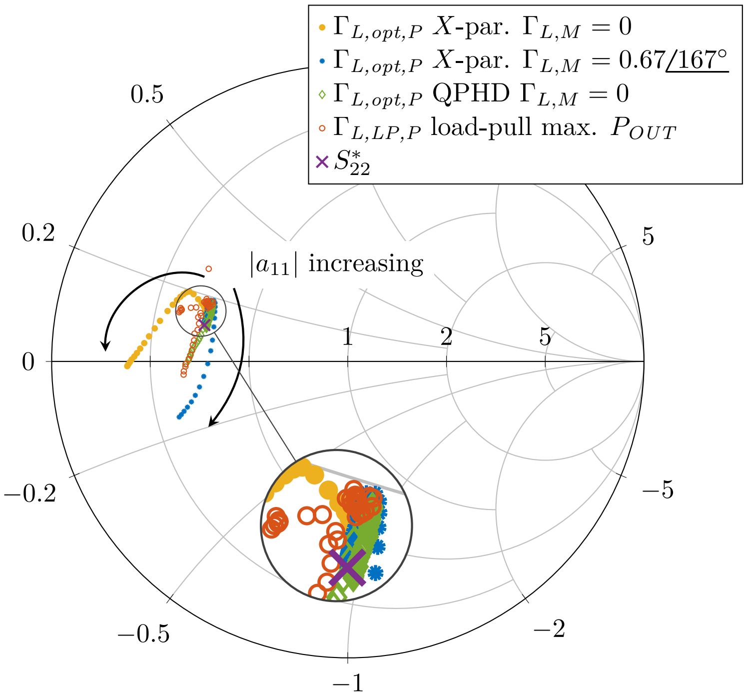

Figure 6.7: Optimum load condition for obtaining maximum output power at $I_{D,q} = 500\,\text{mA}$ and increasing input power, calculated from a $50\,\Omega$ X-parameter, load-dependent X-parameter, and a QPHD model. The results are compared to load-pull measurements and S_{22}^* [106].

low input power levels, i.e., linear operation, the calculated values for $\Gamma_{L,opt,P}$ are equal to S_{22}^*. The offset is in the gained optimum load conditions from the load-pull measurements $\Gamma_{L,LP,P}$, for very low low input power levels. There, the maximum is hard to determine because the load-pull contour is very flat. For increasing input power levels, $\Gamma_{L,LP,P}$ can easier be determined, due to the steeper contour. Similar to Figure 6.6, it can be seen that the QPHD model shows very good agreement with the load-pull measurements, while X-parameters are only accurate for low input power levels.

6.3.2 Maximum Efficiency

Similar as in Section 6.3.1, the optimum load reflection coefficients for efficiency $\Gamma_{L,opt,\eta}$ are compared to load-pull verification measurement results, i.e. $\Gamma_{L,LP,\eta}$. In Figure 6.8, the results for $I_{D,q} = 10\,\text{mA}$ are compared. It can be seen that for very low input power levels (or equivalently low levels for $|a_{11}|$), the measured results for $\Gamma_{L,LP,\eta}$ are accumulated at about the same value. This is because of the

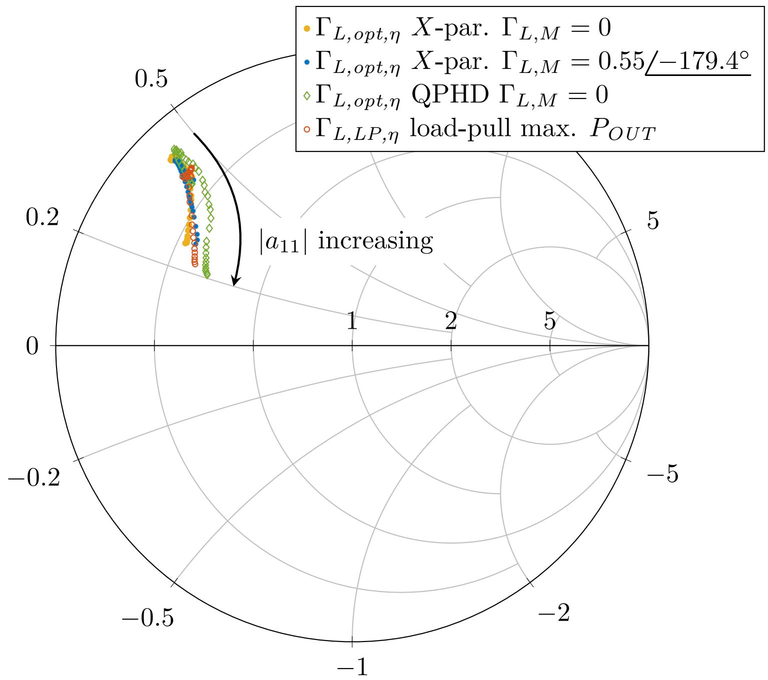

Figure 6.8: Optimum load condition for obtaining maximum efficiency at $I_{D,q} = 10\,\text{mA}$ and increasing input power, calculated from a $50\,\Omega$ X-parameter, load-dependent X-parameter, and a QPHD model. The results are compared to load-pull measurements.

limited tuning range of the measurement setup, limiting the interpolated results for $\Gamma_{L,LP,\eta}$ to the highest achievable reflection coefficient of the setup. Similar to the results for output power, the optimum load condition moves counter-clockwise for increasing input power levels. It can be seen that $\Gamma_{L,opt,\eta}$, calculated for X-parameters and load-dependent X-parameters, shows very good agreement with the measurement, however, for very high input power levels both models lead to a slight error in predicting the optimum load condition for efficiency. Comparatively, the QPHD models leads to a slightly higher accuracy for high input power, but offers lower accuracy for lower input power levels. This is due to numerical issues during the calculation. The quadratic parameters are very small for low input power levels, causing imprecision in the model extraction procedure as well as when solving for $\Gamma_{L,opt,\eta}$. Note that in this graph only the practically relevant solutions are shown.

Similar results can be seen in Figure 6.9, showing the equivalent results for $I_{D,q} = 500\,\text{mA}$. Again, the optimum load conditions for efficiency show less de-

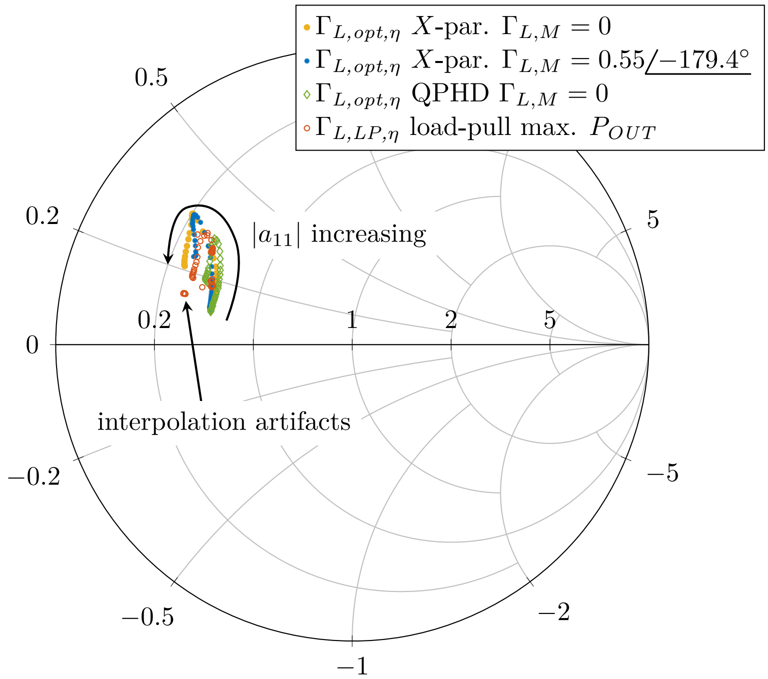

Figure 6.9: Optimum load condition for obtaining maximum efficiency at $I_{D,q} = 500\,\text{mA}$ and increasing input power, calculated from a $50\,\Omega$ X-parameter, load-dependent X-parameter, and a QPHD model. The results are compared to load-pull measurements.

viation. Note, that for very low input power levels an accurate determination of $\Gamma_{L,LP,\eta}$ is tricky, because of the very flat load-pull contour. This causes interpolation artifacts in this graph.

6.4 Prediction of Load-pull Contours

As discussed previously, load-pull contours were traditionally used to determine optimum matching. Although being primarily a measurement technique, it is also possible to determine load-pull contours using models in a CAD environment. Therefore, the load condition is varied empirically, while determining the optimum load by using interpolation techniques.

In Figure 6.10 the modeled load-pull contours are compared to verification measurements. Therefore, the contours for output power P_{OUT} and drain efficiency η_D are determined. A comparison of the contours for output power, gained from the measurement and the X-parameter prediction, is shown in Figure 6.10a. For all the measurements, the DUT and measurement setup discussed in Section 4.5 and Section 4.6 were used, respectively. The drain quiescent current was set to $I_{D,q} = 10\,\mathrm{mA}$ and the available input power to $P_{IN} = 31\,\mathrm{dBm}$ for $50\,\Omega$ source impedance. The frequency of the CW input signal was set to 2.6 GHz and all models and verification measurements were measured under equal operational conditions. For the load-pull measurements, the triplexer based harmonic tuning load-pull setup was used to ensure unchanged harmonic terminations.

It can be seen that the gained contour leads to an error both in the predicted maximum output power and the optimum load reflection coefficient. These results are similar to the observed ones shown in Figure 6.6. Comparatively, the QPHD model based contour is almost identical to the measurement, as shown in Figure 6.10b.

The predicted drain efficiency contour for X-parameters in comparison with the measurement is shown in Figure 6.10c and the corresponding plot for the QPHD model in Figure 6.10d. These results are similar to Figure 6.8. Although both models lead to a slight error in predicting the optimum load condition, it can be seen that the QPHD model shows a significantly higher prediction accuracy for the maximum efficiency value. Equivalent results are observed for $I_{D,q} = 500\,\mathrm{mA}$, as depicted in Figure 6.11.

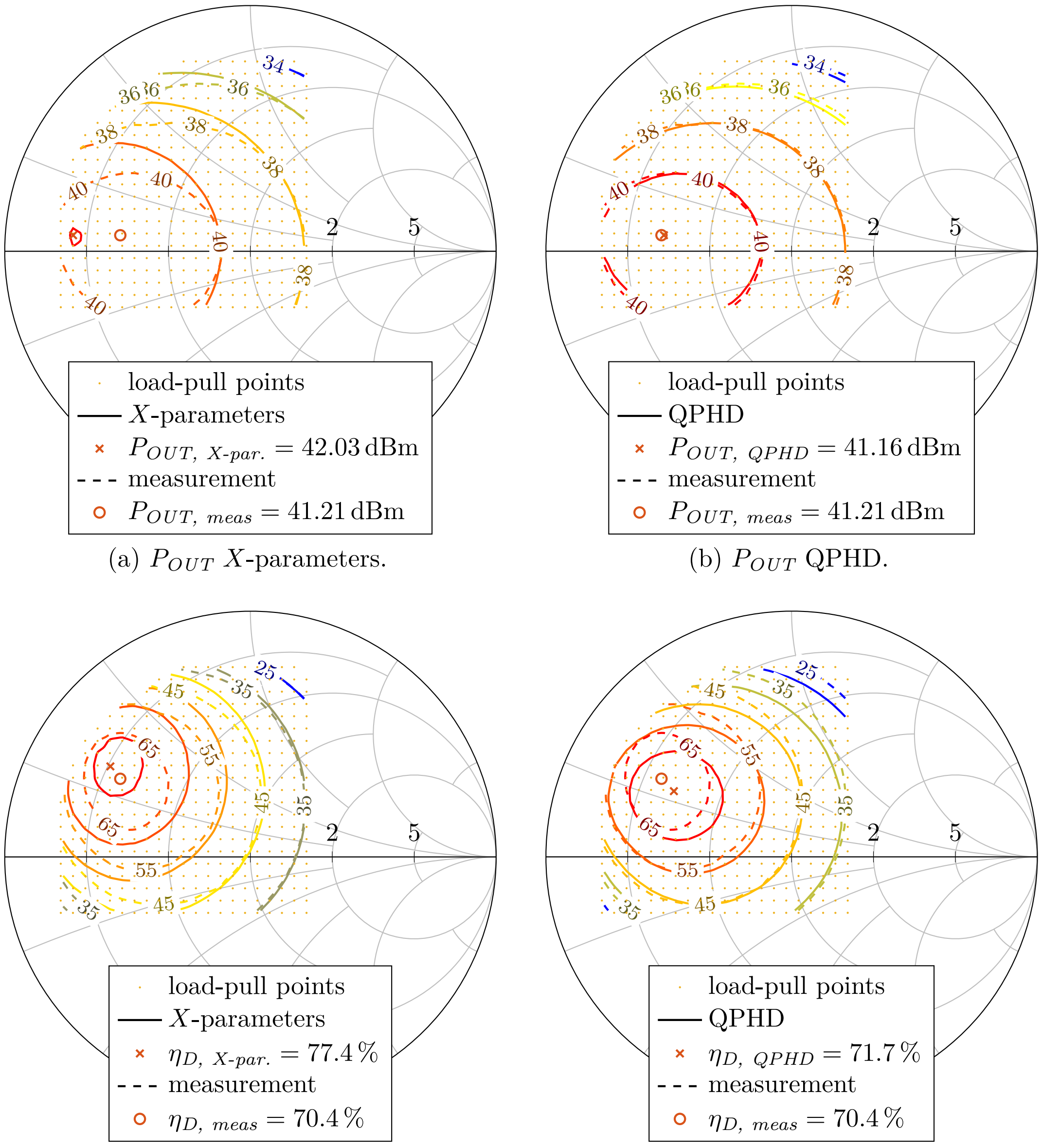

(a) P_{OUT} X-parameters.

(b) P_{OUT} QPHD.

(c) η_D X-parameters.

(d) η_D QPHD.

Figure 6.10: Measured load-pull contours for P_{OUT} and η_D, compared to X-parameters ($\Gamma_{L,M} = 0$) and a QPHD model ($\Gamma_{L,M} = 0$) prediction for $I_{D,q} = 10\,\text{mA}$ and $P_{IN} = 31\,\text{dBm}$ [106].

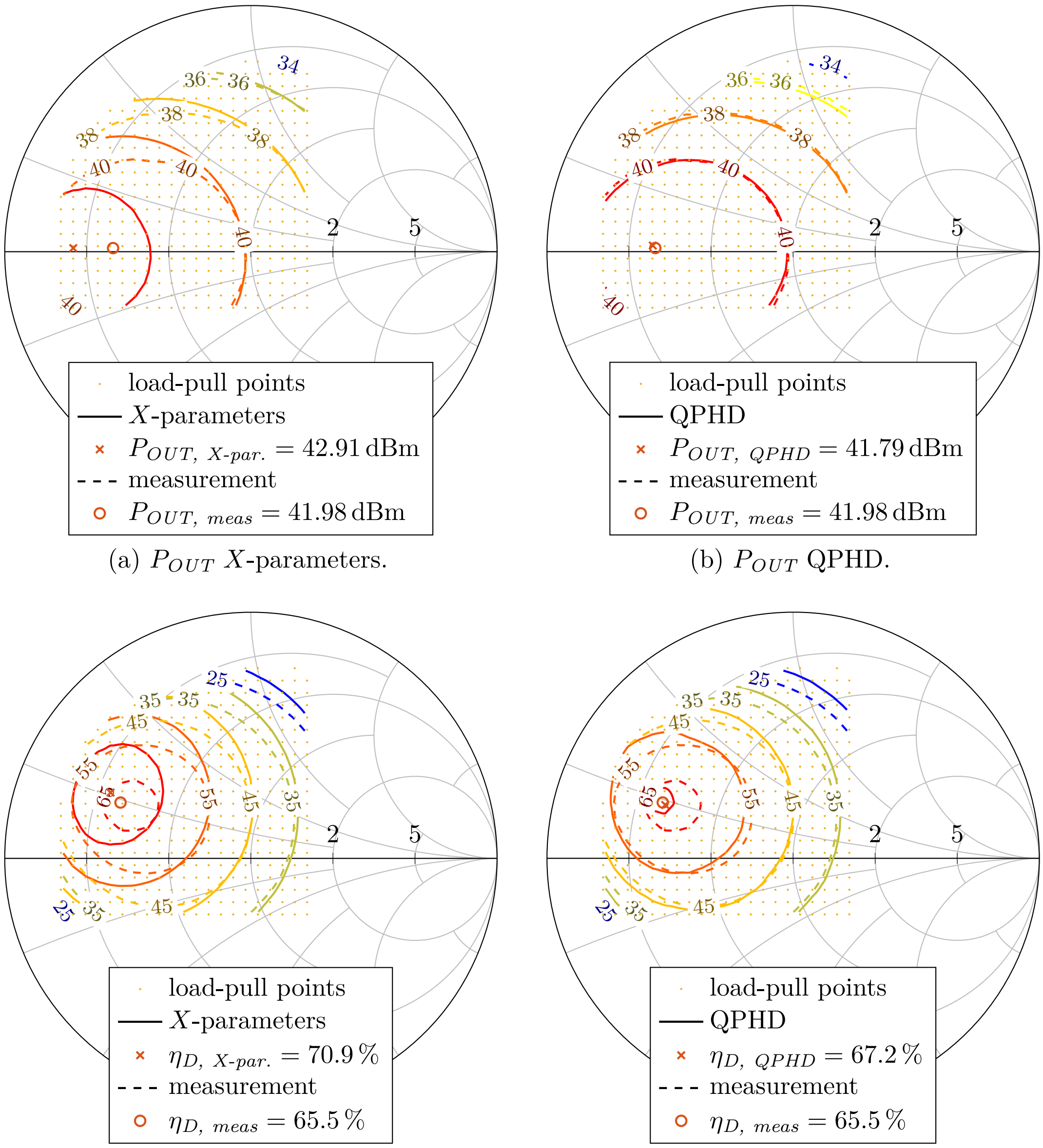

(a) P_{OUT} X-parameters.

(b) P_{OUT} QPHD.

(c) η_D X-parameters.

(d) η_D QPHD.

Figure 6.11: Measured load-pull contours for P_{OUT} and η_D, compared to X-parameters ($\Gamma_{L,M} = 0$) and a QPHD model ($\Gamma_{L,M} = 0$) prediction for $I_{D,q} = 500\,\text{mA}$ and $P_{IN} = 30.9\,\text{dBm}$.

6.5 Summary

Solving the matching problem is crucial in RF circuit design. While there is an analytical solution for linear circuits, i.e., the well-known concept of complex conjugate matching, non-linear DUTs typically rely on empirical solutions like load-pull measurements.

It is possible however, to solve the matching problem analytically using X-parameters. This leads to a closed-form solution for the load condition, necessary for achieving maximum power transfer to the load. Since X-parameters are a superset of S-parameters, this closed-form solution collapses to the complex conjugate matching when applied to a linear DUT. Applied to a non-linear DUT, the accuracy of this solution is limited to the accuracy of X-parameters. Hence, when applied to strongly non-linear DUTs, it fails to predict the correct load condition for maximum output power.

A similar approach can be applied to the QPHD model as well. Since quadratic terms are involved, a simple closed-form solution cannot be found. However, it is possible to find a numerical solution for a given QPHD model. This leads to ambiguous results due to the quadratic terms, but, it can be shown that typically only one solution for the calculated reflection coefficient is inside the unit circle, hence, only one practically relevant solution exist. Similar to the results in Chapter 5, the result shows high accuracy, which was verified using load-pull measurements.

This approach is not limited only for determining the optimum load condition for maximizing the output power, but also for efficiency. Therefore, the DC parameters in the X-parameter model can be utilized. For using X-parameters, this leads to a set of quadratic equations, which can easily be solved numerically. Again, only one solution is inside the unit circle. This allows to predict the load condition for maximizing the efficiency with good accuracy. Furthermore, the QPHD model can be utilized, increasing the accuracy for strongly non-linear DUTs.

To conclude this chapter, simulated load-pull contours using X-parameters and the QPHD model were carried out and compared to verification measurements. It was demonstrated that the QPHD model allows to predict optimum load conditions for efficiency and maximum output power with very good agreement with actual load-pull measurements. This leads to similar results as for calculating $\Gamma_{L,opt,P}$ and $\Gamma_{L,opt,\eta}$. However, it can be seen that the QPHD model offers higher accuracy for predicting the maximum values for output power and efficiency for the used DUT in strongly non-liner operation.

Chapter 7

Conclusion

This thesis discussed the modeling of non-linear RF components by using a black-box behavioral modeling approach based on PHD modeling. In contrast to physics-based or equivalent circuit models, behavioral models enable a comprehensive description of a DUT, without any knowledge of its inner workings. These allow to formulate a model solely on input/output relations on the DUT's ports. Due to their more intuitive interpretation and easier implementation in an RF circuit simulation environment, frequency-domain behavioral models are desired, especially when it comes to RF circuit design. Due to its close relationship to S-parameters, PHD modeling emerged. It offers a superset of S-parameters for describing non-linear DUTs while staying in the traveling waves description framework. The most important and most widely used implementation of PHD modeling are X-parameters. Apart from the model itself, they come with a comprehensive measurement framework, i.e. the *Keysight PNA-X*. This NVNA allows to extract X-parameters, similar to S-parameters and the VNA.

In this thesis the modeling performance of X-parameters and PHD modeling in general were analyzed. Therefore, measured models were compared to verification measurements over a wide range of different modes of operation. The model extraction measurements as well as the verification measurements were performed by a *Keysight N5247A PNA-X*. A load-pull setup was included to enable load-dependent X-parameter measurements. As a DUT, a commercially available GaN HEMT was chosen, the *CREE CGH40010F*. This DUT was operated in various different modes of operation, which were achieved by varying the gate bias voltage and by different types of excitation signals. The chosen DUT is a 10 W device, which exceeds the power handling capabilities of the NVNA. Consequently, the test-set was expanded to a high power configuration. Using this setup and DUT, models and verification measurements were gained, which determined the accuracy of the model prediction.

Due to expansion to the high power setup and the presence of tuners, the strict requirements on the stimulus for an X-parameter measurement were violated. An extraction of the model, while using such a setup, would have caused an inherent systematic error, consequently, a correction was applied by using the model itself. This systematic model error was analyzed by an harmonic load mismatch during the model extraction measurements. It was shown that the MSE on the drain voltage waveform was reduced by more than 6 dB by applied correction, limiting the MSE to MSE < -34 dB.

It has been shown in this thesis, that especially load-dependent X-parameters allowed to accurately predict the behavior of the DUT, even in strongly nonlinear operation. Especially a harmonic load mismatch was modeled accurately, with an MSE < -31 dB. However, for the fundamental frequency, the chosen DUT showed a highly load-sensitive behavior. Consequently, load-dependent X-parameters failed to model the DUT accurately. An increased accuracy was achieved by utilizing load-dependent X-parameters on a grid, but therefore interpolation techniques were required. As shown in this thesis, different interpolation techniques exist, which showed differing results.

By the introduction of quadratic terms to the PHD modeling approach, the QPHD model was formed. This allowed to achieve better accuracy for load sensitive DUTs. It was shown in this thesis, that when the DUT was operated in deep compression, the QPHD model allowed to predict the drain voltage waveform with an MSE < -30.7 dB, while X-parameters and load-dependent X-parameters showed an MSE < -16.6 dB and MSE < -18.7 dB, respectively, for the given tuning range. In addition to the CW excitation, the model accuracy was analyzed by a dynamic excitation, where a two-tone stimulus was utilized. Although a static model, the model prediction was carried out by assuming quasi-static conditions. Consequently, the simulation was performed in the envelope domain. For the results in this thesis, two different load conditions were used, while determining the model prediction response. Compared to verification measurements, it was shown that the QPHD model's prediction showed higher accuracy, for both the fundamental tone and the third order intermodulation products. The improved accuracy was therefore demonstrated well. However, extraction the QPHD model turned out to be challenging, because the offset phase technique lead to an ill-conditioned set of equations in many cases. A more robust approach for the model extraction was found by utilizing load-pull techniques. This mimicked the offset phase technique by applied mismatches at the DUT's ports. Since it was already shown that X-parameters performed well at harmonic mismatches, quadratic terms were only introduced for the fundamental load condition, which lead to a reduced QPHD model. This was able to accurately predict the behavior of the chosen DUT over a wide range of operation.

By using the introduced models, one of the most important problems in RF engineering was analyzed in this thesis, the non-linear matching problem. Therefore, an analytical solution was identified for the load condition for achieving maximum output power by using X-parameters. A similar solution was presented for the QPHD model, but, due to the presence of the quadratic terms only numerical solutions could be calculated, where multiple solutions were obtained. It was shown however, that only one of the solutions was inside the unit circle, hence, only one practically relevant solution existed. The calculated solutions for X-parameters and the QPHD model were compared to verification load-pull measurements, which showed that especially the QPHD was able to predict the optimum load conditions for maximizing the output power accurately. It was demonstrated in this thesis that a solution for the drain efficiency using X-parameters and QPHD model can be derived. This was done by the introduction of the drain current in the model, while constant drain voltage was assumed. For predicting the load condition for maximizing the efficiency, multiple solutions were obtained for both X-parameters and the QPHD model. However, again only one of them was inside the unit circle, i.e. practically relevant. The accuracy of this calculated solution was analyzed by comparing them to load-pull verification measurements, which showed good agreement, especially for the QPHD model.

References

[1] J. C. Pedro, “The wonderful world of nonlinearity: A distinguished microwave lecture on the modeling and characterization of RF and microwave circuits,” *IEEE Microwave Magazine*, vol. 16, pp. 22–35, Oct. 2015. 1

[2] S. A. Maas, *Nonlinear Microwave and RF Circuits*. ARTECH HOUSE INC, 2003. 2

[3] N. B. C. Jose Carlos Pedro, *Intermodulation Distortion in Microwave and Wireless Circuits*. ARTECH HOUSE INC, 2003. 2, 11

[4] C. Desset, B. Debaillie, V. Giannini, A. Fehske, G. Auer, H. Holtkamp, W. Wajda, D. Sabella, F. Richter, M. J. Gonzalez, H. Klessig, I. Gódor, M. Olsson, M. A. Imran, A. Ambrosy, and O. Blume, “Flexible power modeling of LTE base stations,” in *Proc. IEEE Wireless Communications and Networking Conf. (WCNC)*, pp. 2858–2862, Apr. 2012. 2

[5] S. C. Cripps, *RF Power Amplifiers for Wireless Communications*. Artech House Publishers, 2006. 2, 17, 66, 76, 94

[6] J. H. David E. Root, Jan Verspecht and M. Marcu, *X-parameters, Characterization, modeling, and design of nonlinear RF and microwave components*. The Cambridge RF and microwave engineering series, Cambridge: Cambridge University Press, 2013. 2, 40, 41, 73, 88

[7] J. M. Cusack, S. M. Perlow, and B. S. Perlman, “Automatic load contour mapping for microwave power transistors,” *IEEE Transactions on Microwave Theory and Techniques*, vol. 22, pp. 1146–1152, Dec. 1974. 4, 16

[8] K. S. Kundert and A. Sangiovanni-Vincentelli, “Simulation of nonlinear circuits in the frequency domain,” *IEEE Transactions on Computer-Aided Design of Integrated Circuits and Systems*, vol. 5, pp. 521–535, Oct. 1986. 4

[9] L. W. Nagel, "Spice-simulation program with integrated circuit emphasis," *Memo No.. ERL-M382, Electronics Research Laboratory, Univ. of California, Berkeley*, 1973. 5

[10] J. C. Pedro and S. A. Maas, "A comparative overview of microwave and wireless power-amplifier behavioral modeling approaches," *IEEE Transactions on Microwave Theory and Techniques*, vol. 53, pp. 1150–1163, Apr. 2005. 5, 6

[11] M. C. Jeruchim, P. Balaban, and K. S. Shanmugan, *Simulation of communication systems: modeling, methodology and techniques*. Springer Science & Business Media, 2006. 5, 6

[12] W. R. Curtice, "RF and Microwave Semiconductor Device Handbook," ch. Nonlinear Transistor Modeling for Circuit Simulation, pp. 17.1–17.20, Boca Raton, FL, USA: CRC Press, Inc., 2003. 6

[13] C. M. Snowden, *Semiconductor Device Modelling*. Springer Science & Business Media, Dec. 2012. Google-Books-ID: hSHjBwAAQBAJ. 6

[14] J. J. Ebers and J. L. Moll, "Large-signal behavior of junction transistors," *Proceedings of the IRE*, vol. 42, pp. 1761–1772, Dec. 1954. 7

[15] H. K. Gummel and H. C. Poon, "An integral charge control model of bipolar transistors," *The Bell System Technical Journal*, vol. 49, pp. 827–852, May 1970. 7

[16] L. W. Nagel, "Spice2: A computer program to simulate semiconductor circuits," *Ph. D. dissertation, University of California at Berkeley*, 1975. 7

[17] H. Kondoh, "An accurate FET modelling from measured S-parameters," in *Proc. IEEE MTT-S Int. Microwave Symp. Digest*, pp. 377–380, June 1986. 7

[18] W. R. Curtice, "A MESFET model for use in the design of GaAs integrated circuits," *IEEE Transactions on Microwave Theory and Techniques*, vol. 28, pp. 448–456, May 1980. 8

[19] H. Statz, P. Newman, I. W. Smith, R. A. Pucel, and H. A. Haus, "GaAs FET device and circuit simulation in SPICE," *IEEE Transactions on Electron Devices*, vol. 34, pp. 160–169, Feb. 1987. 8

[20] I. Angelov, H. Zirath, and N. Rosman, "A new empirical nonlinear model for HEMT and MESFET devices," *IEEE Transactions on Microwave Theory and Techniques*, vol. 40, pp. 2258–2266, Dec. 1992. 8

[21] T. Mimura, S. Hiyamizu, T. Fujii, and K. Nanbu, “A new field-effect transistor with selectively doped GaAs/n-Al$_x$Ga$_{1-x}$As heterojunctions,” *Japanese journal of applied physics*, vol. 19, no. 5, p. L225, 1980. 8

[22] M. Asif Khan, A. Bhattarai, J. Kuznia, and D. Olson, “High electron mobility transistor based on a GaN-Al$_x$ Ga$_{1-x}$N heterojunction,” *Applied Physics Letters*, vol. 63, no. 9, pp. 1214–1215, 1993. 9

[23] L. Dunleavy, C. Baylis, W. Curtice, and R. Connick, “Modeling GaN: Powerful but challenging,” *IEEE Microwave Magazine*, vol. 11, pp. 82–96, Oct. 2010. 9

[24] I. Angelov, V. Desmaris, K. Dynefors, P. A. Nilsson, N. Rorsman, and H. Zirath, “On the large-signal modelling of AlGaN/GaN hemts and SiC mesfets,” in *Proc. European Gallium Arsenide and Other Semiconductor Application Symp. GAAS 2005*, pp. 309–312, Oct. 2005. 9

[25] R. Pengelly, B. Millon, D. Farrell, B. Pribble, and S. Wood, “Application of non-linear models in a range of challenging gan hemt power amplifier designs,” in *IEEE MTT-S Int. Microw. Symp. Dig*, 2008. 9, 66

[26] R. Pengelly, “6-port GaN HEMT models help designers optimize PA efficiency,” tech. rep., Cree Inc., 2013. 9

[27] D. E. Root, S. Fan, and J. Meyer, “Technology independent large signal non quasi-static FET models by direct construction from automatically characterized device data,” in *Proc. 21st European Microwave Conf*, vol. 2, pp. 927–932, Sept. 1991. 9

[28] D. Schreurs, M. O’Droma, A. A. Goacher, and M. Gadringer, *RF Power Amplifier Behavioral Modeling*. New York, NY, USA: Cambridge University Press, 1st ed., 2008. 10, 11

[29] J. Wood and D. E. Root, *Fundamentals of Nonlinear Behavioral Modeling for RF and Microwave Design*. Artech House, 2005. 10

[30] M. Schetzen, *The Volterra and Wiener theories of nonliner systems*. Malabar, Fla.: Krieger Publ., [2.] reprint ed. with add. materials ed., 2006. Literaturangaben. 10, 11

[31] D. R. Morgan, Z. Ma, J. Kim, M. G. Zierdt, and J. Pastalan, “A generalized memory polynomial model for digital predistortion of RF power amplifiers,” *IEEE Transactions on Signal Processing*, vol. 54, pp. 3852–3860, Oct. 2006. 11

[32] S. Boyd, Y. Tang, and L. Chua, “Measuring Volterra kernels,” *IEEE Transactions on Circuits and Systems*, vol. 30, pp. 571–577, Aug. 1983. 11, 22

[33] Q.-J. Zhang, K. C. Gupta, and V. K. Devabhaktuni, “Artificial neural networks for RF and microwave design - from theory to practice,” *IEEE Transactions on Microwave Theory and Techniques*, vol. 51, pp. 1339–1350, Apr. 2003. 12, 13

[34] J. Wood, *Behavioral Modeling and Linearization of RF Power Amplifiers*. Artech House, June 2014. 12, 14

[35] M. A. Nielsen, *Neural networks and deep learning*, vol. 25. Determination press San Francisco, CA, USA, 2015. 13

[36] J. Xu, D. Gunyan, M. Iwamoto, A. Cognata, and D. E. Root, “Measurement-based non-quasi-static large-signal FET model using artificial neural networks,” in *Proc. IEEE MTT-S Int. Microwave Symp. Digest*, pp. 469–472, June 2006. 14

[37] E. W. Matthews, “The use of scattering matrices in microwave circuits,” *IRE Transactions on Microwave Theory and Techniques*, vol. 3, pp. 21–26, Apr. 1955. 14

[38] K. Kurokawa, “Power waves and the scattering matrix,” *IEEE Transactions on Microwave Theory and Techniques*, vol. 13, pp. 194–202, Mar. 1965. 15

[39] D. C. Youla, “On scattering matrices normalized to complex port numbers,” *Proc. IRE 49,1221*, 1961. 15

[40] B. Pichler, N. Leder, T. Faseth, H. Arthaber, and G. Magerl, “Efficiency enhanced switched mode power amplifier for digital RF transmitters,” in *Proc. IEEE 16th Annual Wireless and Microwave Technology Conf. (WAMICON)*, pp. 1–3, Apr. 2015. 16

[41] B. Pichler, N. Leder, T. Faseth, and H. Arthaber, “Design of a PWM driven continuous mode class F amplifier using harmonic load pull measurements,” in *Proc. Mediterranean Microwave Symp. (MMS2014)*, pp. 1–3, Dec. 2014. 17

[42] M. S. H. Fadhel M. Ghannouchi, *Load-Pull Techniques with Applications to Power Amplifier Design*. Springer-Verlag GmbH, 2012. 17, 18

[43] Y. Takayama, “A new load-pull characterization method for microwave power transistors,” in *Proc. IEEE-MTT-S Int. Microwave Symp*, pp. 218–220, June 1976. 18

[44] P. D. van der Puije and S. R. Mazumder, “Two-signal method of measuring the large-signal S-parameters of transistors,” in *Proc. IEEE-MTT-S Int. Microwave Symp. Digest*, pp. 263–266, June 1978. 20, 22

[45] J. Verspecht, D. Barataud, J.-P. Teyssier, and J.-M. Nébus, “Hot S-parameter techniques: 6= 4+ 2,” in *66th ARFTG Microwave Measurements Conf. Dig*, pp. 7–15, 2005. 20

[46] J. Martens and P. Kapetanic, “Probe-tone S-parameter measurements,” *IEEE Transactions on Microwave Theory and Techniques*, vol. 50, pp. 2076–2082, Sept. 2002. 20

[47] T. Gasseling, D. Barataud, S. Mons, J.-. Nebus, J. P. Villotte, J. J. Obregon, and R. Quere, “Hot small-signal S-parameter measurements of power transistors operating under large-signal conditions in a load-pull environment for the study of nonlinear parametric interactions,” *IEEE Transactions on Microwave Theory and Techniques*, vol. 52, pp. 805–812, Mar. 2004. 20

[48] J. Verspecht, “Everything you’ve always wanted to know about «Hot-S22»(but were afraid to ask),” in *Intoducing New Concepts in Nonlinear Network Design, Workshop at the International Microwave Symposium*, 2002. 22, 26, 29

[49] F. Verbeyst and V. Bossche, “VIOMAP, the S-parameter equivalent for weakly nonlinear RF and microwave devices,” *IEEE Transactions on Microwave Theory and Techniques*, vol. 42, pp. 2531–2535, Dec. 1994. 23, 24

[50] F. Verbeyst and M. V. Bossche, “The Volterra input-output map of a high-frequency amplifier as a practical alternative to load-pull measurements,” *IEEE Transactions on Instrumentation and Measurement*, vol. 44, pp. 662–665, June 1995. 23, 24

[51] F. Verbeyst, “Using orthogonal polynomials as alternative for VIOMAP to model hardly nonlinear devices,” in *Proc. 47th ARFTG Conf. Digest*, vol. 29, pp. 112–120, June 1996. 24

[52] J. Peyton Jones and S. Billings, “Describing functions, Volterra series, and the analysis of non-linear systems in the frequency domain,” *International Journal of Control*, vol. 53, no. 4, pp. 871–887, 1991. 24

[53] J. Verspecht, “Describing functions can better model hard nonlinearities in the frequency domain than the volterra theory.,” -, 1995. 24

[54] J. Verspecht, D. F. Williams, D. Schreurs, K. A. Remley, and M. D. McKinley, “Linearization of large-signal scattering functions,” *IEEE Transactions on Microwave Theory and Techniques*, vol. 53, pp. 1369–1376, Apr. 2005. 25

[55] Verspecht and D. E. Root, “Polyharmonic distortion modeling,” *IEEE Microwave Magazine*, vol. 7, pp. 44–57, June 2006. 26, 27, 28, 29

[56] J. Verspecht, M. vanden Bossche, and F. Verbeyst, “Characterizing components under large signal excitation: Defining sensible "large signal s-parameters"?!,” in *Proc. th ARFTG Conf. Digest-Spring*, vol. 31, pp. 109–117, June 1997. 26

[57] J. Verspecht and P. Van Esch, “Accurately characterizing hard nonlinear behavior of microwave components with the nonlinear network measurement system: Introducing nonlinear scattering functions,” in *Proc. 5th Int. Workshop Integrated Nonlinear Microwave Millimeterwave Circuits*, pp. 17–26, 1998. 27

[58] M. Myslinski, F. Verbeyst, M. V. Bossche, and D. Schreurs, “S-functions extracted from narrow-band modulated large-signal network analyzer measurements,” in *Proc. 74th ARFTG Microwave Measurement Conf*, pp. 1–8, Nov. 2009. 30

[59] Z. Qinglong and L. Shengli, “Comparative study of X-parameters and nonlinear scattering functions,” in *Proc. IEEE 2011 10th Int. Conf. Electronic Measurement Instruments*, vol. 3, pp. 355–358, Aug. 2011. 30

[60] H. Qi, J. Benedikt, and P. Tasker, “A novel approach for effective import of nonlinear device characteristics into CAD for large signal power amplifier design,” in *Proc. IEEE MTT-S Int. Microwave Symp. Digest*, pp. 477–480, June 2006. 30

[61] H. Qi, J. Benedikt, and P. J. Tasker, “Nonlinear data utilization: From direct data lookup to behavioral modeling,” *IEEE Transactions on Microwave Theory and Techniques*, vol. 57, pp. 1425–1432, June 2009. 31, 32, 33

[62] H. Qi, *Nonlinear Data Utilization: Direct Data Look-up to Behavioural Modelling.* PhD thesis, Cardiff University, 2008. 32, 33

[63] S. Woodington, T. Williams, H. Qi, D. Williams, L. Pattison, A. Patterson, J. Lees, J. Benedikt, and P. J. Tasker, “A novel measurement based method enabling rapid extraction of a RF waveform look-up table based behavioral

model," in *Proc. IEEE MTT-S Int. Microwave Symp. Digest*, pp. 1453–1456, June 2008. 33

[64] S. Woodington, R. Saini, D. Williams, J. Lees, J. Benedikt, and P. J. Tasker, "Behavioral model analysis of active harmonic load-pull measurements," in *Proc. IEEE MTT-S Int. Microwave Symp. Digest (MTT)*, pp. 1688–1691, May 2010. 33, 35, 36

[65] P. J. Tasker and J. Benedikt, "Waveform inspired models and the harmonic balance emulator," *IEEE Microwave Magazine*, vol. 12, pp. 38–54, Apr. 2011. 34, 35

[66] P. J. Tasker, "Practical waveform engineering," *IEEE Microwave Magazine*, vol. 10, pp. 65–76, Dec. 2009. 36

[67] J. M. Horn, J. Verspecht, D. Gunyan, L. Betts, D. E. Root, and J. Eriksson, "X-parameter measurement and simulation of a GSM handset amplifier," in *Proc. European Microwave Integrated Circuit Conf*, pp. 135–138, Oct. 2008. 38

[68] J. Verspecht, D. Gunyan, J. Horn, J. Xu, A. Cognata, and D. E. Root, "Multi-tone, multi-port, and dynamic memory enhancements to PHD non-linear behavioral models from large-signal measurements and simulations," in *Proc. IEEE/MTT-S Int. Microwave Symp*, pp. 969–972, June 2007. 44

[69] C. Xie, T. Zhang, and D. Liu, "Using X-parameters to model mixers," in *Proc. Int. Conf. Microwave and Millimeter Wave Technology (ICMMT)*, vol. 3, pp. 1–3, May 2012. 44

[70] G. Simpson, J. Horn, D. Gunyan, and D. E. Root, "Load-pull + NVNA = enhanced X-parameters for PA designs with high mismatch and technology-independent large-signal device models," in *Proc. 72nd ARFTG Microwave Measurement Symp*, pp. 88–91, Dec. 2008. 44

[71] J. Horn, D. E. Root, and G. Simpson, "GaN device modeling with X-parameters," in *Proc. IEEE Compound Semiconductor Integrated Circuit Symp. (CSICS)*, pp. 1–4, Oct. 2010. 44

[72] B. Pichler, N. Leder, G. Magerl, and H. Arthaber, "On the dependability of load dependent X-parameter models for varying loads," in *Integrated Nonlinear Microwave and Millimetre-wave Circuits Workshop (INMMiC), 2017*, pp. 1–3, 2017. 46

[73] D. E. Root, J. Verspecht, D. Sharrit, J. Wood, and A. Cognata, "Broad-band poly-harmonic distortion (PHD) behavioral models from fast automated simulations and large-signal vectorial network measurements," *IEEE Transactions on Microwave Theory and Techniques*, vol. 53, pp. 3656–3664, Nov. 2005. 50

[74] J. Verspecht, D. E. Root, J. Wood, and A. Cognata, "Broad-band, multi-harmonic frequency domain behavioral models from automated large-signal vectorial network measurements," in *Proc. IEEE MTT-S Int. Microwave Symp. Digest*, pp. 4 pp.–, June 2005. 51

[75] D. Gunyan, D. Root, L. Betts, and J. Horn, "Large Signal Scattering Functions From Orthogonal Phase Measurements," July 23 2009. US Patent App. 12/015,932. 51

[76] W. V. Moer and L. Gomme, "NVNA versus LSNA: enemies or friends?," *IEEE Microwave Magazine*, vol. 11, pp. 97–103, Feb. 2010. 55

[77] M. Sipila, K. Lehtinen, and V. Porra, "High-frequency periodic time-domain waveform measurement system," *IEEE Transactions on Microwave Theory and Techniques*, vol. 36, pp. 1397–1405, Oct. 1988. 55

[78] D. J. Ballo, "The microwave transition analyzer: A new instrument architecture for component and signal analysis," *Hewlett Packard Journal*, 1992. 55

[79] F. van Raay and G. Kompa, "A new on-wafer large-signal waveform measurement system with 40 GHz harmonic bandwidth," in *Proc. IEEE MTT-S Microwave Symp. Digest*, pp. 1435–1438 vol.3, June 1992. 56

[80] J. Verspecht, P. Debie, A. Barel, and L. Martens, "Accurate on wafer measurement of phase and amplitude of the spectral components of incident and scattered voltage waves at the signal ports of a nonlinear microwave device," in *Proc. IEEE MTT-S Int. Microwave Symp*, pp. 1029–1032 vol.3, May 1995. 56

[81] J. Verspecht, "Large-signal network analysis," *IEEE Microwave Magazine*, vol. 6, pp. 82–92, Dec. 2005. 56

[82] U. Lott, "Measurement of magnitude and phase of harmonics generated in nonlinear microwave two-ports," *IEEE Transactions on Microwave Theory and Techniques*, vol. 37, pp. 1506–1511, Oct. 1989. 59, 65

[83] D. Barataud, M. Campovecchio, and J.-. Nebus, “Optimum design of very high-efficiency microwave power amplifiers based on time-domain harmonic load-pull measurements,” *IEEE Transactions on Microwave Theory and Techniques*, vol. 49, pp. 1107–1112, June 2001. 59

[84] P. Blockley, D. Gunyan, and J. B. Scott, “Mixer-based, vector-corrected, vector signal/network analyzer offering 300kHz-20GHz bandwidth and traceable phase response,” in *Proc. IEEE MTT-S Int. Microwave Symp. Digest*, pp. 4 pp.–, June 2005. 60, 64

[85] Hewlett Packard, “Harmonic generation using step recovery diodes and SRD modules, Application Note AN920,” tech. rep., Hewlett Packard, 1968. 62

[86] D. Gunyan and Y.-P. Teoh, “Characterization of active harmonic phase standard with improved characteristics for nonlinear vector network analyzer calibration,” in *Proc. 71st ARFTG Microwave Measurement Conf*, pp. 1–7, June 2008. 62

[87] Keysight, “Keysight Technologies U9391C/F/G Comb Generators, 5989-7619EN,” Sept. 2017. 62, 63

[88] W. Kruppa and K. F. Sodomsky, “An explicit solution for the scattering parameters of a linear two-port measured with an imperfect test set (correspondence),” *IEEE Transactions on Microwave Theory and Techniques*, vol. 19, pp. 122–123, Jan. 1971. 64

[89] A. Ferrero and U. Pisani, “Two-port network analyzer calibration using an unknown ’thru’,” *IEEE Microwave and Guided Wave Letters*, vol. 2, pp. 505–507, Dec. 1992. 64

[90] J. Verspecht, “Broadband sampling oscilloscope characterization with the "nose-to-nose" calibration procedure: a theoretical analysis,” in *Proc. 10th Anniversary. IMTC/94. Advanced Technologies in I M. 1994 IEEE Instrumentation and Measurement Technolgy Conf. (Cat. No.94CH3424-9)*, pp. 526–529 vol.2, May 1994. 65

[91] P. Roblin, *Nonlinear RF Circuits and Nonlinear Vector Network Analyzers: Interactive Measurement and Design Techniques*. Cambridge University Press, 2011. 66, 70

[92] Cree Inc., “CHG40010F Datasheet,” 2012. 66

[93] Rogers Corporation, "RO4000® Series High Frequency Circuit Materials Datasheet," 2018. 66

[94] G. F. Engen and C. A. Hoer, "Thru-reflect-line: An improved technique for calibrating the dual six-port automatic network analyzer," *IEEE Transactions on Microwave Theory and Techniques*, vol. 27, pp. 987–993, Dec. 1979. 66

[95] Keysight, "High Power Amplifier Measurements Using Nonlinear Vector Network Analyzer, Application Note 5990-5039EN," tech. rep., Keysight Technologies, 2014. 68

[96] Keysight, "Keysight Technologies Vector Network Analyzer Receiver Dynamic Accuracy, Application Note N5247-90003," tech. rep., Keysight Technologies, 2016. 68

[97] Keysight, "Keysight 2-Port and 4-Port PNA-X Network Analyzer N5247A, Data Sheet and Technical Specifications N5247-90002," tech. rep., Keysight Technologies, 2014. 68

[98] Keysight, "Keysight NVNA Help, NVNA Rev. A.02.10.01." `http://na.support.keysight.com/pna/nvna/NVNAWebHelp/NVNAHelp.htm`, July 2019. 70

[99] B. Pichler, N. Leder, G. Magerl, and H. Arthaber, "Load error correction for high power load dependent X-parameter measurements," in *Proc. 12th European Microwave Integrated Circuits Conf. (EuMIC)*, pp. 216–219, Oct. 2017. 73

[100] B. Pichler, N. Leder, G. Magerl, and H. Arthaber, "Experimental study on load dependent X-parameter models for PA design," in *Proc. IEEE Radio and Antenna Days of the Indian Ocean (RADIO)*, pp. 1–2, Sept. 2017. 76

[101] J. Cai, J. B. King, B. M. Merrick, and T. J. Brazil, "Padé-approximation-based behavioral modeling," *IEEE Transactions on Microwave Theory and Techniques*, vol. 61, pp. 4418–4427, Dec. 2013. 80

[102] G. Z. E. Nashef, F. Torrès, S. Mons, T. Reveyrand, T. Monédière, E. N'Goya, and R. Quéré, "Second order extension of power amplifiers behavioral models for accuracy improvements," in *Proc. 40th European Microwave Conf*, pp. 1030–1033, Sept. 2010. 80

[103] J. Cai, J. B. King, A. Zhu, J. C. Pedro, and T. J. Brazil, "Nonlinear behavioral modeling dependent on load reflection coefficient magnitude,"

IEEE Transactions on Microwave Theory and Techniques, vol. 63, pp. 1518–1529, May 2015. 80

[104] C. Maziere, D. Gapillout, A. Xiong, and T. Gasseling, "High efficiency doherty power amplifier design using enhanced poly-harmonic distortion model," in *Proc. Antennas and Electronic Systems (COMCAS) 2015 IEEE Int. Conf. Microwaves, Communications*, pp. 1–5, Nov. 2015. 81

[105] B. Pichler, G. Magerl, and H. Arthaber, "A robust extraction technique for second order PHD based behavioral models," in *Proc. Int. Workshop Integrated Nonlinear Microwave and Millimetre-wave Circuits (INMMIC)*, pp. 1–3, July 2018. 82

[106] B. Pichler, G. Magerl, and H. Arthaber, "A study on quadratic PHD models for large signal applications," *IEEE Transactions on Microwave Theory and Techniques*, vol. 67, pp. 2514–2520, July 2019. 89, 91, 92, 100, 101, 106, 107, 108, 112

[107] D. M. Pozar, *Microwave Engineering*. JOHN WILEY & SONS INC, 2011. 95, 96

[108] A. M. Pelaez-Perez, S. Woodington, M. Fernandez-Barciela, P. J. Tasker, and J. I. Alonso, "Application of an NVNA-Based System and Load-Independent X-Parameters in Analytical Circuit Design Assisted by an Experimental Search Algorithm," *IEEE Transactions on Microwave Theory and Techniques*, vol. 61, pp. 581–586, Jan. 2013. 97

[109] D. E. Root, J. Verspecht, and J. Xu, "Closed-form solutions to large-signal PA problems: Wirtinger calculus applied to X-parameter," in *Proc. 12th European Microwave Integrated Circuits Conf. (EuMIC)*, pp. 212–215, Oct. 2017. 97, 99

[110] W. Wirtinger, "Zur formalen Theorie der Funktionen von mehr komplexen Veränderlichen [On the formal theory of functions of more complex variables]," *Mathematische Annalen*, vol. 97, p. 357, Dec. 1927. 97, 103

[111] B. Pichler and H. Arthaber, "Solution for the large-signal matching problem: Maximizing the efficiency using X-parameters," in *Submitted for Integrated Nonlinear Microwave and Millimetre-wave Circuits Workshop (INMMiC)*, 2020. 103, 104